TU Clausthal
Clausthal University of Technology

# Material Parameter Identification using Finite Elements and Digital Image Correlation

Doctoral Thesis
(Dissertation)

to be awarded the degree of

Doctor in Engineering (Dr.-Ing.)

submitted by

M. Sc. Rose Rogin Gilbert

from Trivandrum, India
(Origin)

approved by the Faculty of
Mathematics/Computer Science and Mechanical Engineering,
Clausthal University of Technology

Date of oral examination
02.06.2021

Dean
Prof. Dr. rer. nat. Jörg P. Müller

Chairperson of the Board of Examiners
Prof. Dr.-Ing. Gunther Brenner

Supervising Tutor and Reviewer
Prof. Dr.-Ing. Stefan Hartmann

Reviewer
Prof. Dr.-Ing. Andreas Menzel

*For Indootyyy*

# Foreword

> No one who achieves success does so without acknowledging the help of others. The wise and confident acknowledge this help with gratitude. - Alfred North Whitehead

The thesis work presented here is based on my work from December 2013 - December 2019 at the Institute of Applied Mechanics at the Clausthal University Of Technology. First and foremost, I would like to thank Prof. Dr.-Ing. habil Stefan Hartmann for his valuable guidance and mentorship during my time at the institute. Without his advice and recommendations this thesis wouldn't have been fruitful. I would like to acknowledge the financial support by the German-Israeli Foundation for Scientific Research and Development (GIF) and the German Research Foundation (DFG).

I would like to thank my friends and colleagues that I have met in this *my home far away from home* called Clausthal-Zellerfeld. I would like to thank my office mate Dr.-Ing. Maria Angeles Martinez Page for all the valuable discussions (scientific and unscientific), giving me the perfect atmosphere to work and of course, for all the cooking parties. A special thanks to Dr.-Ing. Matthias Grafenhorst for always helping me with the many problems encountered during implementation in Tasafem. I would like to thank Dipl.-Ing. Chris Leistner for all the valuable discussions with regards to material parameter identification and helping me with the experiments, especially setting up the DIC system and for all the fun we had together. A special shout-out to M.Sc. Pranav Kumar Dileep for all the valuable discussions regarding different aspects of modelling. Let me also say thanks to M.Sc. Lutz Müller-Lohse for all help he provided me for the representation of the pictures and for our fun discussions during coffee breaks. I would also like to thank M.Sc. Ali Kheirimarghzar for all the laughs and the discussions regarding transversal isotropy. A special thanks must be mentioned to Ms. Heidi Andresen for all the help, valuable talks and advices throughout my time at the institute. I would also like to thank Mr. Jan Sue, our head of the workshop in preparation of the specimens. A special thanks has to be given to Dr.-Ing. Stephan Krämer for the valuable tips he gave me at the first stage of my work regarding material parameter identification. I would also like to thank M.Sc. Laura Mignanelli for valuable discussions about experiments and statistics. I would also like to thank my other former colleagues Dr.-Ing. Steffen Rothe, Dr.-Ing. Carmen Sguazzo, M.Sc. Susana Rodriguez Porto and Dr.-Ing. Raad Al-Kinani for all the valuable advices and tips they provided me during the start of my research work.

I would like to thank Jithin Mohan and Nimi Jithin for being my closest friends and confidants. They always believed in me and supported me (both personally and professionally) and never said no to me, any time of the day. I would also like to thank my other friends Sibin Saseendran, Praseeth Prabhakar, Hinesh Madhusoodanan and a lot of other friends who made my stay in Clausthal a wonderful adventure.

Let me express my sincere appreciation to my parents and siblings for all the love and prayers

they provided me during this time. My strength is the support and love of my family. Last but not least, my heartfelt gratitude to my lovely wife, Indulekha, without whose love, care and unwavering support this thesis wouldn't have come into being.

Clausthal-Zellerfeld, January 2021 Rose Rogin Gilbert

# Abstract

In nature, there exists many materials exhibiting different behavior. In the field of Solid Mechanics, these material behavior are characterized with the help of constitutive models like elasticity, plasticity etc. Nowadays, computer aided simulations assist in analyzing real processes by solving complicated problems numerically. Within the context of Solid Mechanics, these complicated problems are generally solved using the widely known Finite Element Methods. In order to predict correctly the different processes, it is essential to know the material parameters that are used to characterize the constitutive model used in modeling the physical properties like Young's modulus, Poisson's ratio etc. To this extent, the process of material parameter identification is used. The aim of the thesis is to discuss several aspects of material parameter identification.

In order to predict the behavior of a material under different loading conditions, it is essential to identify material parameters with a certain confidence. This is the foundation of this research work. The basics of Continuum Mechanics and the method of finite elements to solve the partial differential equation are formulated. High-order time integrators are used to discretize the problem in temporal domain. It has the advantage of higher accuracy and greater flexibility so that concept of time adaptivity can be used. The non-linear system of equations obtained by the spatial and temporal discretization is solved using classical Newton-Raphson method or Multilevel-Newton algorithm (MLNA).

The basic problem of identification along with the concept of local identifiability is formulated. The concept of local identifiability is a very important aspect of Solid Mechanics which is mostly ignored by researchers. The reason for this is unknown. The prediction of material behavior might lead to highly erratic results, if the identified material parameters are not accurate. This is one of the primary focus of this thesis work. For inhomogeneous deformations, finite element method has to be used to identify material parameters. In addition to the usage of finite elements, if full-field data by using a Digital Image Correlation (DIC) system can also be measured during experiments, it provides a great deal of information to identify the material parameters accurately. The determination of sensitivities required for the identification can be a tedious process. Typically, finite difference schemes (also known as External Numerical Differentiation (END)) are used, which is a time-consuming process if there are many material parameters to be identified. Alternatively, the sensitivities can be determined using the Internal Numerical Differentiation (IND). This concept is explained in detail with the help of MLNA.

In this thesis, different aspects of parameter identification are discussed with the help of several examples. Several simple examples are analyzed to understand the basic problems in parameter identification. It can be concluded that certain quality measures must be analyzed to ensure that the identified parameters are within a certain confidence. Finally, the identification process is performed to identify parameters of an overstress-type finite strain viscoelastic model, modeled for a rubber specimen. Different rate-dependent biaxial experiments and multistep relaxation biaxial experiment with full field data using a DIC-system were performed on the rubber specimen. The sensitivities for strain measures and reaction forces are explicitly provided to the optimizer. This enabled the comparison of the computational time to identify the parameters using END and IND. From the results, it can be concluded that IND is faster than END. This research work points out the significance of proper material parameter identification.

# Contents

# 1. Introduction

In this day and age, for research and development every industry makes use of computer simulations of different processes on different materials, like, aerospace industry, automotive industry, field of biomechanics, weather etc. First concept of computer simulations dates back to 1947 by Stanisław Marcin Ulam, see (Ulam et al., 1990). While playing solitaire, Ulam developed the idea of playing hundreds of games to analyse the probability of a successful outcome. It was around that time, the electronic general-purpose digital computer known as ENIAC (Electronic Numerical Integrator and Computer) was developed, see (Eckert Jr. and Mauchly, 1964). Ulam along with Nicholas Metropolis proposed the Monte Carlo method, see (Metropolis and Ulam, 1949), while working at the Los Alamos National Laboratory. Realizing the importance of using computers to solve or analyze mathematical problems, John von Neumann programmed the ENIAC to perform Monte Carlo simulations on neutron diffusion in fissionable material. FERMIAC, developed by Enrico Fermi, was a computer developed to perform mechanical simulations of random diffusion of neutrons, see (Metropolis, 1987). From performing analog simulations to performing very complicated simulations, the computers and the methods to solve these complicated problems have advanced exponentially. Computer aided simulation are nowadays used in weather prediction, solid mechanics, fluid mechanics, quantum physics etc. It has become one of the essential tools in the field of research and development.

By the beginning of 1940s, a new method needed to be developed to solve complex structural problems. This lead to the development of the most popular method in Solid Mechanics called finite element method (FEM). The history of FEM can be traced back to (Hrennikoff, 1941) and (Courant, 1943). With the development of FEM along with advancement in Computer Science, analysis of different problems in the field of Solid Mechanics was advanced to a whole new level. This enabled development of complicated material models (models describing the behavior of materials) which couldn't be solved previously due to lack of computational power. These material models are characterized by material parameters. With new and improved material models, the prediction of the behavior of complex materials has immensely advanced. However, without proper material parameter identification, it is not possible to obtain a reasonable prediction of the behavior of materials. This forms the basis of this thesis.

## 1.1. Motivation

The work presented in this thesis was funded partly by the German-Israeli Foundation for Scientific Research and Development (GIF) and the German Research Foundation (DFG). The GIF project (I-89-202.17-2012) titled "Vasoreactive response of the skeletonized distal internal thoracic artery and bifurcation branches: Application for CABG" was to model the mechanical

response of the arteries under the influence of pressure and chemicals. It was a collaborative project between the universities TU Munich, TU Clausthal in Germany and the Ben Gurion University in Beer-Sheva, Israel. The experiments were performed in the Ben Gurion University. Using the experiments, an preexisting model for the passive response and a new concept for active response of the arteries were developed, see (Gilbert et al., 2019), and implemented in the in-house FORTRAN based finite element code TASAFEM. During the material parameters identification, it was found out that depending on the initial guess provided to the solver in Matlab, the solution would converge to different material parameters, see (Gilbert et al., 2016). Naturally, this means that multiple solution exists. Using these material parameters, the behavior of the arteries couldn't be predicted as different material parameters lead to different behavior. This necessitated the studies in identifiability in Solid Mechanics, see (Hartmann and Gilbert, 2018). This formed the motivation of this thesis.

The second part of the work is to determine the sensitivities using different methods. This part of the work was funded by the German Research Foundation (DFG). In order to demonstrate different methods, real experiments were carried out on rubber specimens using biaxial testing machine developed at the institute. The rubber specimens were provided by Dr. Nils Hendrik Kröger from the DIK (Deutsches Institut für Kautschuktechnologie e.V., Hannover, Germany). Using the experiments performed on the specimens, the parameters were identified for an overstress-type viscoelastic model. The advantages and the disadvantages of different methods to determine the sensitivities were also analyzed.

## 1.2. State of the Art

In nature exists, different kinds of materials exhibiting different behaviors. These materials are used in manufacturing different machine components, building structures etc. In order to use computer aided simulations, it is essential that the behavior of these materials are characterized. The characterization of behavior of materials is known as *constitutive modeling*. The laws of continuum mechanics are used to develop these constitutive relations, see (Holzapfel, 2000; Haupt, 2002). In the field of solid mechanics (scope of this thesis), depending on the behavior of the material, the constitutive modeling is classified into elasticity, plasticity, viscoelasticity and viscoplasticity. In this thesis work, the constitutive modeling is limited to elasticity and viscoelasticity.

Rubber materials can be modeled using hyperelasticity or viscoelasticity. One of the first constitutive model for rubber was proposed by (Mooney, 1940) which was in turn expressed using strain energy function in terms of a linear combination of two invariants of the left Cauchy-Green tensor by (Rivlin, 1948). It was a hyperelastic model and is widely known as Mooney-Rivlin model. The Mooney-Rivlin model was further extended to a polynomial-type elasticity by (Rivlin and Saunders, 1951). Ogden (1976) expressed a strain energy function in terms of the three principal stretches. Using the 8-chain molecular structure of a representative volume element, Arruda and Boyce (1993) proposed a hyperelastic constitutive model. This model is widely used nowadays to model rubber and other polymers. Simo (1987) developed a thermodynamically consistent finite strain viscoelastic model based on internal variables, including

damage. Liu et al. (1994) provided the stress tensor and the consistent tangent for some invariant-based viscoelastic models. By adding a volumetric part of the free energy, the incompressible model was extended to a compressible model. Based on the multiplicative decomposition of deformation gradient into volumetric and isochoric parts proposed by Flory (1961), Holzapfel (1996) proposed a finite strain viscoelastic with Ogden-type strain energy function. Based on this model, a thermodynamically consistent model based on internal variables under varying temperature was proposed by (Holzapfel and Simo, 1996). A constitutive model representing the viscoelasticity as a phenomenological theory was proposed by (Lion, 1996). The softening behavior, called Mullins effect, seen in the first few cycles was excluded by applying a few cycles of loading and unloading while performing the experiments. The Mullins effect was incorporated by a continuum damage model. This model was extended to include the thermal effects by (Lion, 1997). Based on the multiplicative viscoelastic decomposition proposed by (Sidoroff, 1974), (Govindjee and Reese, 1997) proposed a new model for finite deformation viscoelasticity under the assumption of a viscoelastic potential to provide a similar modeling concept to elasto-plasticity. Examples for uniaxial plane strain relaxation and creep were analysed. This model was extended by Reese and Govindjee (1998) to be flexible away from the thermodynamic equilibrium. Bergström and Boyce (1998) performed a detailed experimental campaign on carbon black-filled chloroprene rubber subjected to different rate-dependent tests. One of the primary observation was that the rate dependence is higher during the loading than during the unloading based on which a new constitutive model was proposed. For a simple linear viscoelastic model, like three-parameter models, application of the classic rheological spring-dashpot models with regards to a spring in parallel with a Maxwell element as well as a spring in series with a Kelvin element is researched by (Huber and Tsakmakis, 2000). Based on multiplicative decomposition of the deformation gradient tensor, a finite strain viscoelastic model was proposed. For uniaxial tension-compression example, it was shown that a prediction of mechanical response for finite deformations are challenging. A phenomenological material model for a superimposed finite elastic–viscoelastic–plastoelastic stress response with damage for carbon-black filled rubbers was proposed by (Miehe and Keck, 2000). Tension, torsion and combinations of both these tests were performed by (Haupt and Sedlan, 2001) on cylindrical bars made of a carbon-black filled rubber. A thermodynamically consistent model of viscoplasticity is proposed based on the experiments. In this thesis, the rubber is assumed to be modelled using a overstress-type viscoelastic model. A model based on (Lubliner, 1985; Lion, 1997) was proposed by (Hartmann, 2002). For the description of the equilibrium stress state, the elasticity relation based on (Hartmann, 2001b) that fits into polynomial-type elasticity of (Rivlin and Saunders, 1951) was applied. A slight modification of this model is taken in this thesis work to model the response of the rubber specimens.

The balance equations along with the constitutive equations on which the basics of continuum mechanics is developed cannot be solved analytically for real life problems. Simple problems can be solved analytically. However, the complicated problems, called initial boundary value problems (so-called because the solution of such problems should also satisfy both the initial and the boundary conditions), are solved numerically using the finite element method. The development of finite elements was the turning point for computer aided simulation in the field of Solid Mechanics. The basic ideas regarding finite elements (coined by Ray William Clough in (Clough,

1960)) can be found in works by (Hrennikoff, 1941) and (Courant, 1943). The major leaps in the field of finite element method was due to works by (Zienkiewicz, 1984; Zienkiewicz and Taylor, 2000a; Bathe, 1986; Hughes, 1987; Simo and Hughes, 1998). Using finite elements saves a lot of time and cost as real experiments are expensive and time consuming to develop. Finite element simulation are nowadays used in almost every industry like aerospace, weather forecast, transportation, biomechcanics to name a few typical utilization of the FE concepts to solve real world problems. Here, Fig. 1.1 shows a typical example of a 3D model of a complicated geometry like a pig artery in the field of biomechanics, Fig. 1.1(a), and the finite element simulation result are shown in Fig. 1.1(b). Finite element simulation provide an alternative to conducting expen-

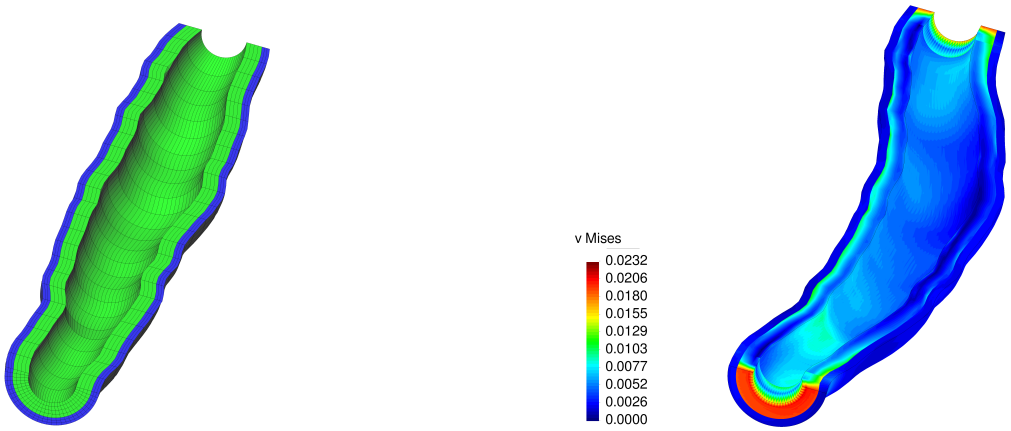


(a) Mesh of an artery

(b) Stress distribution in an artery

Figure 1.1.: Undeformed configuration and von Mises stress distribution inside the artery (units in $\mathrm{N\,mm^{-2}}$), see (Gilbert et al., 2019)

sive experiments for designing parts and components, analyzing real processes etc. FEM uses the underlying partial differential equation by applying the method of vertical lines, see (Wittekindt, 1991; Fritzen, 1997; Schiesser, 1991; Ellsiepen and Hartmann, 2001). First, a spatial discretization is applied leading to a system of differential-algebraic equations (DAEs) followed by a temporal discretization resulting in a system of non-linear equations which are subsequently solved using different methods. The domain is divided into different elements with nodes connecting each elements. An ansatz function for the displacement field is formulated. Depending on the accuracy required for the computation, the number of degrees of freedom of the elements can be increased. The easiest way is to increase the number of elements keeping the ansatz of the displacement field constant is known as h-FEM, see (Zienkiewicz, 1984; Zienkiewicz and Taylor, 2000a; Bathe, 1986; Hughes, 1987; Simo and Hughes, 1998). Yet another method is to increase the order of the ansatz function keeping the number of elements constant. This method is popularly known as p-FEM, see (Peano, 1976; Szabo and Mehta, 1978; Szabó, 1979; Babuska et al., 1981; Szabo and Babuska, 1991). Another method is to increase both the number of elements as well as the order of the polynomial of the ansatz function. This method is known as hp-FEM, see (Guo and Babuška, 1986; Schwab et al., 1998; Demkowicz et al., 1989). The spatial discretiza-

tion leads to a system of DAEs (depending on the partial differential equation). These DAEs are then temporally discretized. Normally, one-step methods like Backward-Euler type methods are applied to discretize in time. Most commercial software use this method. According to Hartmann (1998), after the discretization of the DAEs, the resulting non-linear system of equations can be solved using Multilevel-Newton algorithm (MLNA), see (Rabbat et al., 1979). This differentiates the whole process into global and local level with the local level being the Gauss-point level. This enables successful application of high-order time integration schemes like Runge-Kutta methods, see (Hairer et al., 1993; Hairer and Wanner, 1996; Alexander, 1977). The use of Runge-Kutta procedures is very well demonstrated in (Ellsiepen and Hartmann, 2001) within the context of a von Mises-type plasticity model. These methods with respect to viscoelasticity model was discussed in (Hartmann, 2002). These schemes provides with a great amount of flexibility. The concept of time-adaptivity (step-size control) can be applied without any essential additional numerical costs, see (Hartmann, 2003). A history-based time adaptive scheme was proposed by (Gilbert et al., 2019) on the basis of mechanical response of arteries. The time-discretization leads to a system of non-linear equations which can be solved using classical Newton-Raphson scheme or Multilevel Newton algorithm, see (Rabbat et al., 1979). For discussion with regards to finite elements, see for more details (Ellsiepen and Hartmann, 2001; Hartmann, 2005).

Once the IBVP is setup, the next step would be to perform simulations. However, before the simulation can be performed, it is essential to know the material parameters that characterize the constitutive relations. The process of determining these parameters with the help of experimental data is known as *material parameter identification*. A residual vector between experimental data and simulated data is build up, the $L_2$ norm of which has to be minimized in a least-square sense and as such is a nonlinear problem which might lead to multiple solutions. Different types of experiments are performed in order to identify the material parameters, like, uniaxial tensile-compression tests, biaxial tests, indentation tests, tube under internal pressure etc. In this thesis, some examples are investigated to better understand the different concepts and challenges of identification. The study aims to form a bridge between mathematics and engineering from the context of material parameter identification. To obtain a specific homogeneously distributed stress and homogeneously distributed strain state within a small region of the specimen, uniaxial tensile tests are carried out. This is a go-to test for most material models. Integral quantity (a quantity resulting from integration over a domain) like force can be measured directly using a force gauge. For isotropic materials in small strain range, different strain measuring devices like strain gauge or video extensometer are used to obtain the strain (local) at region of interest. Using the forces and the strain data, the parameters can be identified. However, in the case of complicated models (like transversal isotropy, orthotropy etc.), the problem is not so direct. In inhomogeneous deformation state, it is essential to know the local strain distribution especially in the small region under consideration. For this purpose, the so-called Digital Image Correlation (DIC) systems are used. Developed by Sutton et al. (1983), the theory behind DIC is the comparison of digital images of a local region of interest at different stages of deformation, see (McCormick and Lord, 2010). The comparison is done by tracking blocks of pixels to measure the displacement and strain on the surface. The pixel blocks needs to be random and unique. In order to ensure this, the rubber specimens are painted at first using a white paint and then black dots are sprayed on the surface. Using a DIC-system, discrete points on the surface of

the specimen can be tracked in real-time and the spatial coordinates or strain measures of those points at each time step can be obtained. This provides the user with more data to identify the material parameters. In such cases, it is essential to use FEM to identify the material parameters. Another experiment that can be performed are compression tests. These are a bit more challenging as it may lead to buckling of the specimen which adversely affects the identification, see (Amin et al., 2002; Hartmann et al., 2003). Another important experiment is the application of torsion on thin-walled tubes, see (Haupt and Lion, 1995) and the references cited therein. It is done under the assumption that the shear stress is constant across the wall leading to a homogeneous shear stress and strain state for a small-strain region. Kadlowec et al. (2003); Haupt and Sedlan (2001) perform torsion tests for large-strain deformations under the assumption of isotropy and incompressibility. This, however, is an inhomogeneous deformation state. Shear tests are also used to determine certain parameter, like shear modulus, see (Sutton et al., 2009). Three-rail small strain shear tests according to (Sguazzo and Hartmann, 2018) was performed on glass-fiber epoxy resin composites with the help of DIC-system by (Hartmann et al., 2021, 2020). Another typical experiment to identify material parameters are indentation tests, see (Lee et al., 2005; Hartmann et al., 2006; Rauchs et al., 2010; Chen and Diebels, 2014). Biaxial tests are also known to be used in the determination of material parameters, see (Ognedal et al., 2012; Lamkanfi et al., 2015; Hartmann et al., 2018a). In this thesis, biaxial tests are performed on rubber specimens to identify the material parameters for an overstress-type viscoelastic model.

Another important aspect of material parameter identification is the local identifiability of material parameters. *Local Identifiability* is the determination of uniqueness of the material parameters. The identification problem is a nonlinear problem leading to multiple solutions. Therefore, it is essential to know whether the identified parameters are locally unique. The concept of identifiability was first mentioned in (Beveridge and Schechter, 1970; Beck and Arnold, 1977) for the general case in parameter identification. The application of these concepts in the realm of solid mechanics can be found in (Hartmann and Gilbert, 2018; Hartmann et al., 2018a, 2021; Sewerin, 2020) and literature cited therein. Identifiability problem can be defined as the necessary conditions under which material parameters are uniquely identified. Hartmann and Gilbert (2018); Hartmann et al. (2021) also discuss quality measures describing the quality of the identified material parameters, such as the confidence interval, the correlation between the parameters and coefficient of determination. Using these concepts, material parameter was identified for a glass-fiber epoxy composites, see (Hartmann et al., 2020), and the model was validated using a plate with a hole. The prediction was accurate to within 30% for force as well as strain distribution. This accurate prediction shows the importance of the concepts of identifiability.

In order to uniquely identify material parameters, in addition to force data obtained from force gauges, it is essential to have full-field data. DIC-system are a recently (since 1980s) popular approach which provides full-field information in terms of displacements or strains on a sub-region of the surface of a specimen. This full-field data can then be compared to finite element simulation data, (Andresen et al., 1996; Mahnken and Stein, 1996, 1997; Sutton et al., 2009; Grédiac and Hild, 2013; Hartmann et al., 2020, 2021). The works of Mahnken have mainly combined the use of finite element simulations with material parameter identification in the context of solid mechanics problems. There are many other researches based on this concept, see (Scheday, 2003; Kreißig, 1998; Benedix et al., 1998; Kreissig et al., 2001; Cooreman et al., 2007; Krämer, 2016)

where a gradient-based optimization method is used. For a more comprehensive view, please see (Mahnken, 2018) and the references cited therein. An optimization-based identification scheme was outlined for self-diagnostic poly(dimethylsiloxane)(PDMS) elastomer by Schulte et al. (2020). Rose and Menzel (2019, 2020) identified thermal material parameters based on full field temperature measurement. Several identifications were performed to analyse the impact of the convection and conduction coefficient. A finite strain nonlinear magneto-viscoelasticity was introduced by (Kiefer et al., 2015) and the parameters were identified for a magnetoactive polymer (MAP). Hartmann et al. (2003) approached the problem on a gradient-free scheme based on numerical algorithm proposed by Powell (1994, 1998). Neural network can also be applied for identification of material parameters, see (Huber and Tsakmakis, 1999a,b). Kleuter et al. (2007) and Heimes (2005) discusses the parameter identification for the case of finite strain viscoelasticity using the classical FEM/DIC approach. For the completion of the identification process, objective function has to be at the local minimum. Sensitivity is the derivative of the residuum with respect to material parameters. The determination of sensitivities is a very rarely researched upon topic. Hartmann (2017) compares three approaches namely, *simultaneous simulation equations*, *internal*, and *external numerical differentiation* to determine the sensitivities as mentioned in Numerical Mathematics such as it is published in (Schittkowski, 2002). The methods were compared on the basis of constitutive models with internal variables. In this thesis, with the help of a numerical example, an overall insight is provided on the different aspects of material parameter identification detailed here.

## 1.3. Framework of the Thesis

The thesis focuses mainly on the different aspects of identification, concepts of local identifiability and the determination of sensitivities with the help of an example. This subsection outlines the structure of the thesis.

The thesis is composed of six chapters. *Chapter 2* introduces the basic concepts of Continuum Mechanics. The basic idea regarding the kinematics including the definitions of configuration, motion and different strain measures used are introduced. The stress measures used for the development of constitutive relations are also defined. Details about a set of governing equations known as *balance equations* of Continuum Mechanics is also explained to conclude the chapter.

In *Chapter 3*, the finite element method, used to solve partial differential equations, is introduced. It discusses the setting up of the Initial Boundary Value Problem (IBVP). The solution procedure known as method of vertical lines is then discussed. The method depicts the spatial discretization of the domain followed leading to system of DAEs. This is detailed in the next section. This system of DAEs are then discretized in the time domain resulting in set of non-linear system of equations. This can be done using simple methods like Backward-Euler scheme or complicated yet better high-order scheme called Runga-Kutta scheme. This is explained in detail. Finally, some discussions on the solution procedure for the set of non-linear equations using the Multilevel-Newton algorithm concludes the chapter.

The main content of the thesis is discussed in *Chapter 4*. Several aspects of parameter identification are discussed in detail in this chapter. At first, the setting up of the non-linear least square

(NLS) problem is detailed. Next, certain quality measures are introduced to show the quality of the solution. This is necessary as the NLS problem is ill-posed leading to multiple solutions. Another important aspect of identification known as *concept of local identifiability* is introduced in the subsequent section. It is necessary to know that the identified parameters are locally unique. A unique set of parameters is essential for a good prediction of the behavior of the material. This motivated investigations into the concept of identifiability. The chapter concludes by explaining different methods to determine the sensitivities with respect to displacement as well force.

*Chapter 5* details the concepts introduced in other chapters with the help of several examples. Simple examples are taken into consideration to study the identifiability in Solid Mechanics. Basic problems encountered in the case of large strain analyses are also outlined in this chapter. The determination of sensitivities are also investigated with the help of certain examples. Finally, a real example is analyzed to investigate all the concepts introduced for a complicated case. For this purpose, at first, the experimental set-up along with details about the specimen used is introduced. The material model used to characterize the behavior of the material is then introduced. An overstress-type viscoelastic model is used in this work. This is then followed by the discussion for the setting up of the identification problem with regards to the example. Finally, the result of the identification of the material parameters for equilibrium and the overstress part are discussed to conclude the chapter.

In the final chapter, the main ideas presented in the thesis is summarized, concluding the thesis.

# 2. Basics in Continuum Mechanics

Continuum Mechanics is a combination of mathematics with various physical laws to approximate behavior of a body $\mathcal{B}$, under different loading conditions. The body is assumed to be continuous and infinitely divisible into many particles or material points. In this research work, a very brief description outlining the fundamental relations in Continuum Mechanics is described. For a more comprehensive, please refer to numerous works by (Truesdell and Noll, 2004), (Marsden and Hughes, 1994), (Ogden, 1997), (Malvern, 1969), (Holzapfel, 2000) and (Haupt, 2002). In order to quantify material behavior in Continuum Mechanics, five important steps must be undertaken:

- Description of the kinematics
- Consideration of the associated loads
- Respecting the governing equations
- Development of a constitutive relation
- Formulation of the initial boundary value problem

Kinematics (originated from a Greek word "kinesis" meaning motion) is also referred to as geometry of motion and it describes the motion and deformation of a material body without reference to reason of motion (mechanical, thermal etc.). The first step in Continuum Mechanics begins with kinematics. The mechanical behavior of materials is approximated by certain equations called constitutive equations. These constitutive relations are governed by the balance equations in continuum mechanics. Both kinematics and constitutive relations are required to model the behavior of a material. This forms the basic of continuum mechanics.

## 2.1. Kinematics

In this section, the basics in kinematics, the different configurations and motion of a material body is introduced. Certain quantities to describe the kinematics like deformation gradient, strain measures etc. are also described.

### 2.1.1. Configuration and Motion

In Continuum Mechanics, a material body $\mathcal{B}$ is a body that occupies a three dimensional Euclidean space $\mathbb{E}^3$ with matter and has a mass. It is composed of infinite set of material points $\mathcal{B} = \{\mathcal{P}\}$, see (Haupt, 2002). The material body has to satisfy two important properties in order

to describe the kinematics, first being

$$\chi := \begin{cases} \mathcal{B} & \to \chi[\mathcal{B}] \subset \mathbb{R}^3 \\ \mathcal{P} & \to \chi(\mathcal{P}) = (x_1, x_2, x_3) \Longleftrightarrow \mathcal{P} = \chi^{-1}(x_1, x_2, x_3) \end{cases} \tag{2.1}$$

where $\mathcal{K} = \{\chi\}$ is set of one-to-one mappings with every mapping $\chi \in \mathcal{K}$ are called the configurations. This condition ensures that space occupied by one material point belongs to that point only and is not shared by any other material point. The second important property is the composition of two configurations $\chi_1 \in \mathcal{K}$ and $\chi_2 \in \mathcal{K}$ must be continuously differentiable,

$$\chi_1 \circ \chi_2^{-1} := \begin{cases} \chi_1[\mathcal{B}] & \to \chi_2[\mathcal{B}] \subset \mathbb{R}^3 \\ (x_1, x_2, x_3) & \to (y_1, y_2, y_3) = \chi_2(\chi_1^{-1}(x_1, x_2, x_3)). \end{cases} \tag{2.2}$$

This property ensures that two neighboring material points remain neighbors. The motion of a material body $\mathcal{B}$ is characterized with the parameter time $t$ as a series of configurations

$$t \to \chi_t := \begin{cases} \mathcal{B} & \to \chi_t[\mathcal{B}] \subset \mathbb{R}^3 \\ \mathcal{P} & \to \chi_t(\mathcal{P}) = (x_1(t), x_2(t), x_3(t)) \Longleftrightarrow \mathcal{P} = \chi_t^{-1}(x_1(t), x_2(t), x_3(t)), \end{cases} \tag{2.3}$$

where the time-dependent configuration $\chi_t$ is called the *current configuration* and is usually represented by number triplet $(x_1, x_2, x_3)$ called spatial coordinates. However, in order to define this motion, it is essential to introduce a configuration which is independent of time. This configuration is known as the *reference configuration*,

$$\mathcal{R} := \begin{cases} \mathcal{B} & \to \mathcal{R}[\mathcal{B}] \subset \mathbb{R}^3 \\ \mathcal{P} & \to \mathcal{R}(\mathcal{P}) = (X_1, X_2, X_3) \Longleftrightarrow \mathcal{P} = \mathcal{R}^{-1}(X_1, X_2, X_3) \end{cases} \tag{2.4}$$

represented by the number triplet $(X_1, X_2, X_3)$ called material coordinates. More often than not, the initial configuration is chosen as reference configuration. However, this is not obligatory. The different configurations are detailed in Fig. 2.1. The description of motion can be represented using these configurations and time $t$ by

$$\vec{x} = \vec{\chi}_t(\mathcal{R}^{-1}(\vec{X})) = \vec{\chi}_{\mathrm{R}}(\vec{X}, t). \tag{2.5}$$

Generally in the field of Solid Mechanics, the initial configuration is known and is mostly chosen as the reference configuration. The current configuration is determined by the alteration of the material points. This form of description is known as the Lagrangian description. In Fluid Mechanics, the current configuration is known and so the starting point is the current configuration. Such form of description is known as Eulerian description. The motion of a material point is described by the difference of position vectors in the current and the reference configurations

$$\vec{u}(\vec{X}, t) = \vec{x} - \vec{X} = \vec{\chi}_{\mathrm{R}}(\vec{X}, t) - \vec{X} \tag{2.6}$$

which is the displacement of the particle.

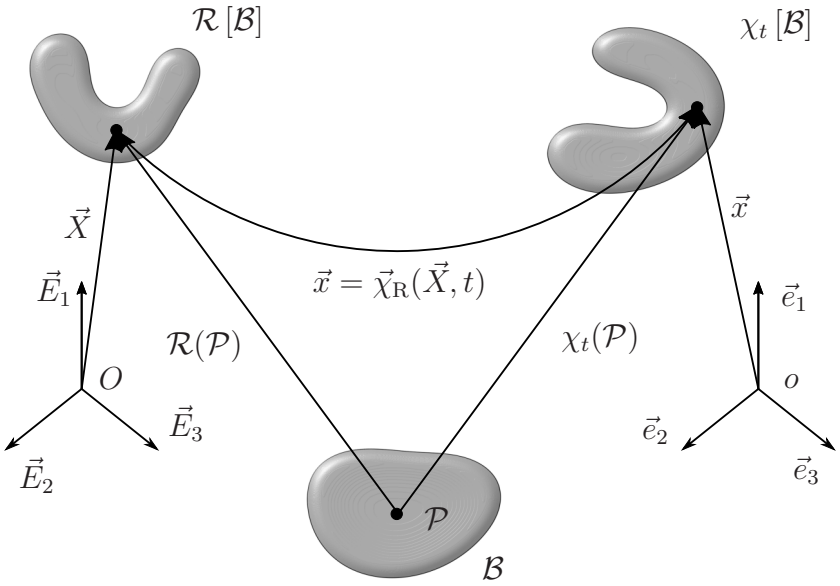


Figure 2.1.: Configurations

## 2.1.2. Deformation Gradient

One of the most crucial entity in continuum mechanics is the deformation gradient $\mathbf{F}$, which characterizes the deformation in the immediate neighborhood of a material point

$$\mathbf{F}(\vec{X}, t) = \mathrm{Grad}\, \vec{\chi}_{\mathrm{R}}(\vec{X}, t). \tag{2.7}$$

The gradient is the derivative with respect to the material coordinates $(X_1, X_2, X_3)$. The deformation gradient can also be expressed in the orthonormal bases in the current configuration $\vec{e}_i$ and the reference configuration $\vec{E}_{\mathrm{A}}$

$$\mathbf{F}(\vec{X}, t) = \mathrm{Grad}\, \vec{\chi}_{\mathrm{R}}(\vec{X}, t) = \frac{\partial \chi_{\mathrm{R}i}}{\partial X_{\mathrm{A}}} \vec{e}_i \otimes \vec{E}_{\mathrm{A}}. \tag{2.8}$$

The material line elements can be transformed from reference to current configuration by, see Fig. 2.2,

$$\mathrm{d}\vec{x} = \mathbf{F}\mathrm{d}\vec{X}. \tag{2.9}$$

For the derivation, please refer (Haupt, 2002). Material surface and volume elements can also be transformed from reference to current configuration by

$$\mathrm{d}\vec{a} = (\det \mathbf{F})\mathbf{F}^{-T}\mathrm{d}\vec{A} \tag{2.10}$$

$$\mathrm{d}v = (\det \mathbf{F})\mathrm{d}V \tag{2.11}$$

where $\det \mathbf{F}$ is the determinant of the deformation gradient with the important property $\det \mathbf{F} > 0$, due to the invertibility of the coordinate transformation.

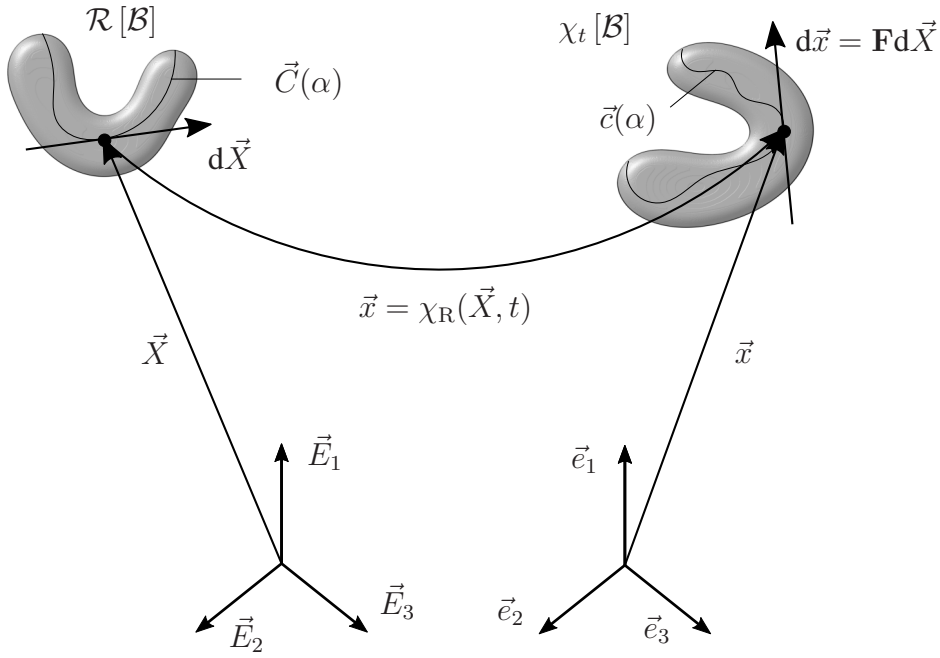


Figure 2.2.: Transformation of material line elements by the deformation gradient

### 2.1.3. Polar Decomposition

Even though deformation gradient is a crucial entity, it contains too much information to be used as a strain measure. From Eq.(2.8), it can be seen that the deformation gradient is a two point tensor. That means it contains information from both the configurations. Additionally, deformation gradient is not symmetric in general which makes it a difficult quantity to work with mathematically. It also accounts for the rigid body contributions (translation as well as rotation). This implies that the deformation gradient does not vanish for rigid body transformations. In order to circumvent these drawbacks, the polar decomposition theorem is applied and the deformation gradient is multiplicatively decomposed into

$$\mathbf{F} = \mathbf{R}\mathbf{U} = \mathbf{V}\mathbf{R}. \tag{2.12}$$

$\mathbf{R}$ is a two point orthogonal tensor (pure rotation) with the following properties

$$\mathbf{R}^{-1} = \mathbf{R}^T \rightarrow \det \mathbf{R} = 1. \tag{2.13}$$

$\mathbf{U}$ and $\mathbf{V}$ are called the right and left stretch tensors with the properties

$$\mathbf{U}^T = \mathbf{U} \quad \text{and} \quad \mathbf{V}^T = \mathbf{V}. \tag{2.14}$$

These tensors are one point tensors and are both positive definite i.e. $\vec{h} \cdot \mathbf{U}\vec{h} > 0$ for arbitrary vectors $\vec{h}$. Using these tensors the right and left Cauchy-Green tensors are introduced, see (Haupt, 2002),

$$\mathbf{C} = \mathbf{F}^T\mathbf{F} = \mathbf{U}^2, \quad \det \mathbf{C} = 1, \tag{2.15}$$

$$\mathbf{B} = \mathbf{F}\mathbf{F}^T = \mathbf{V}^2, \quad \det \mathbf{B} = 1. \tag{2.16}$$

Both the Cauchy-Green tensors are one point, symmetric tensors independent of the rigid body motions,

$$\text{Absence of motion } (\vec{x} = \vec{X}),\ \mathbf{F} = \mathbf{I} \rightarrow \mathbf{C} = \mathbf{B} = \mathbf{I} \tag{2.17}$$

$$\text{Rigid body motion } \mathbf{F} = \mathbf{Q} \rightarrow \mathbf{C} = \mathbf{B} = \mathbf{I} \tag{2.18}$$

where $\mathbf{Q}$ is an orthogonal tensor. It can be seen that under the absence of motion and presence of only rigid body motion both the left and right Cauchy-Green tensors are identity tensors. Thus, the right and left Cauchy-Green tensors can be used to define the strain tensors explained in Sec.2.1.4.

Another important property of the deformation gradient is the multiplicative decomposition of the tensor into an *isochoric* $\overline{\mathbf{F}}$and *volume-changing* $\hat{\mathbf{F}}$ part, see (Flory, 1961),

$$\mathbf{F} = \hat{\mathbf{F}}\overline{\mathbf{F}} \tag{2.19}$$

where

$$\hat{\mathbf{F}} = J^{\frac{1}{3}}\mathbf{I}, \quad \det\hat{\mathbf{F}} = \det\mathbf{F} = J, \tag{2.20}$$

$$\overline{\mathbf{F}} = J^{-\frac{1}{3}}\mathbf{F}, \quad \det\overline{\mathbf{F}} = 1. \tag{2.21}$$

This decomposition concept can also be applied to the polar decomposition with $\det\mathbf{U} = \det\mathbf{V} = \det\mathbf{F} = J$,

$$\overline{\mathbf{U}} = J^{-\frac{1}{3}}\mathbf{U} \tag{2.22}$$

$$\overline{\mathbf{V}} = J^{-\frac{1}{3}}\mathbf{V} \tag{2.23}$$

which leads to the polar decomposition of the isochoric deformation gradient part

$$\overline{\mathbf{F}} = \mathbf{R}\overline{\mathbf{U}} = \overline{\mathbf{V}}\mathbf{R}. \tag{2.24}$$

The unimodular (tensors with determinant $\pm 1$) right and left Cauchy-Green tensor can thus be defined in a similar manner as

$$\overline{\mathbf{C}} = \overline{\mathbf{F}}^T\overline{\mathbf{F}} = \overline{\mathbf{U}}^2, \tag{2.25}$$

$$\overline{\mathbf{B}} = \overline{\mathbf{F}}\overline{\mathbf{F}}^T = \overline{\mathbf{V}}^2. \tag{2.26}$$

### 2.1.4. Strain Measures

Using the right and left Cauchy-Green tensors certain strain measures are defined. One of the most important strain measure is the Green strain tensor,

$$\mathbf{E} = \frac{1}{2}(\mathbf{F}^T\mathbf{F} - \mathbf{I}) = \frac{1}{2}(\mathbf{C} - \mathbf{I}) = \frac{1}{2}(\mathbf{U}^2 - \mathbf{I}) \tag{2.27}$$

and the other is called Almansi strain tensor

$$\mathbf{A} = \frac{1}{2}(\mathbf{I} - \mathbf{F}^{-1}\mathbf{F}^{-T}) = \frac{1}{2}(\mathbf{I} - \mathbf{B}^{-1}) = \frac{1}{2}(\mathbf{I} - \mathbf{V}^{-2}). \tag{2.28}$$

Differentiating the Eq. 2.6 with respect to the material coordinates leads to

$$\mathbf{F} = \mathbf{I} + \mathbf{H} \quad \rightarrow \quad \mathbf{H} = \mathrm{Grad}\,\vec{u} \tag{2.29}$$

where $\mathbf{H}$ is the displacement gradient. The Green strain tensor can be represented in terms of the displacement gradient by

$$\mathbf{E} = \frac{1}{2}(\mathbf{H} + \mathbf{H}^T + \mathbf{H}^T\mathbf{H}). \tag{2.30}$$

The Green tensor operates on reference configuration while the Almansi tensor operates on the current configuration and are related to each other by

$$\mathbf{A} = \mathbf{F}^{-T}\mathbf{E}\mathbf{F}^{-1}, \quad \mathbf{E} = \mathbf{F}^T\mathbf{A}\mathbf{F}. \tag{2.31}$$

## 2.2. Stress Measures

Under the influence of different types of load, deformations occur within a body which leads to stresses. Various stress tensors have been introduced depending on the configuration on which it is characterized, see (Holzapfel, 2000) and (Haupt, 2002). To begin with, a force acting on the surface per area $\mathrm{d}\vec{a} = \vec{n}\mathrm{d}a$ of the deformed solid called surface traction $\vec{t}$ is introduced. For example, if a body is cut into two parts along an arbitrary plane surface, equal and opposite surface tractions are introduced on the surfaces (Newton's third law),

$$\mathrm{d}\vec{f} = \vec{t}\mathrm{d}a = \mathbf{T}\mathrm{d}\vec{a} \tag{2.32}$$

where $\mathbf{T}$ is the *Cauchy stress tensor*. The surface tractions are connected to the Cauchy stress tensor $\mathbf{T}$ by

$$\vec{t} = \mathbf{T}\vec{n}. \tag{2.33}$$

which is known as *Cauchy theorem*. Cauchy stress is often referred to as true stress as it is the actual force acting on the current deformed area. Hence, it is very difficult to measure this entity. This necessitates the introduction of other stress measures. Instead of considering the current deformed area, if the reference area is chosen, a new stress tensor called first Piola-Kirchhoff stress tensor $\mathbf{T}_\mathrm{R}$ is obtained,

$$\mathrm{d}\vec{f} = \vec{t}_\mathrm{R}\mathrm{d}A = \mathbf{T}_\mathrm{R}\mathrm{d}\vec{A}, \quad \mathrm{d}\vec{A} = \vec{n}_\mathrm{R}\mathrm{d}A. \tag{2.34}$$

This is also called engineering stress and is defined as

$$\mathbf{T}_\mathrm{R} = J\mathbf{T}\mathbf{F}^{-T}. \tag{2.35}$$

It is a two point non-symmetric stress tensor because the force is measured in the current configuration while the area considered is in the reference configuration. However, this is convenient for experimental measurement.

As it is not ideal to have information from both configurations in a stress measure, a one point symmetric stress tensor is desired which contains information pertaining to a single configuration. Thus, a new tensor called second Piola-Kirchhoff stress tensor $\widetilde{\mathbf{T}}$ is introduced. It is defined by applying the pull back operation of the Cauchy stress tensor,

$$\widetilde{\mathbf{T}} = J\mathbf{F}^{-1}\mathbf{T}\mathbf{F}^{-T}. \tag{2.36}$$

## 2.3. Balance Equations in Continuum Mechanics

In Sec. 2.1, the kinematics have been introduced. Another important ingredient in Continuum Mechanics is the fundamental principles of mechanics and are called balance equations. They are conservation of mass, Newton's laws of motion (conservation of linear and angular momentum) and the first and second laws of thermodynamics for a continuum. Only the equations are given in this work. For a more detailed explanation, see (Holzapfel, 2000; Haupt, 2002).

### 2.3.1. Balance of Mass

In a closed system, the mass of any subregion of the system must be conserved and is independent of motion and time. This condition can be written as a constraint as following

$$m(\mathcal{B}, t) = \int_V \rho_{\mathrm{R}}(\vec{X}, t)\mathrm{d}V = \int_v \rho(\vec{x}, t)\mathrm{d}v. \tag{2.37}$$

This means that the total mass should remain the same irrespective of the configuration,

$$\int_V (\rho_{\mathrm{R}} - J\rho)\mathrm{d}V = 0 \quad \forall V \tag{2.38}$$

where $J = \det \mathbf{F} = \rho_{\mathrm{R}}/\rho$. The formulation of balance of mass in the reference configuration states that the mass density $\rho_{\mathrm{R}}$ remains constant over time, i.e.,

$$\rho_{\mathrm{R}} = \rho_{\mathrm{R}}(\vec{X}) = \rho \det \mathbf{F}. \tag{2.39}$$

This results in the continuity equation,

$$\frac{\mathrm{d}\rho}{\mathrm{d}t} + \rho \operatorname{div} \vec{v} = 0 \rightarrow \frac{\partial \rho}{\partial t} + \operatorname{div}(\rho \vec{v}) = 0, \tag{2.40}$$

where $\vec{v}(\vec{x}, t)$ represents the velocity field.

### 2.3.2. Balance of Linear Momentum

According to Newton's second law published in Philosophiæ Naturalis Principia Mathematica *"Lex II: Mutationem motus proportionalem esse vi motrici impressae, et fieri secundum lineam rectam qua vis illa imprimitur"*. The translation provided by Andrew Motte reads *"The alteration of motion is ever proportional to the motive force impressed; and is made in the direction of the right line in which that force is impressed"*, see (Newton et al., 1729). This lead to the linear momentum which is essentially the mass of the material body $\mathcal{B}$ multiplied by its velocity,

$$\vec{I}(\mathcal{B},t) = \int\limits_V \rho_{\mathrm{R}}(\vec{X},t)\vec{v}(\vec{X},t)\mathrm{d}V = \int\limits_v \rho(\vec{x},t)\vec{v}(\vec{x},t)\mathrm{d}v. \tag{2.41}$$

The balance of linear momentum states that the time rate of change of total linear momentum is equal to the forces (body and surface) acting on the body. The representation in current configuration is

$$\frac{\mathrm{d}}{\mathrm{d}t}\int\limits_v \rho(\vec{x},t)\vec{v}(\vec{x},t)\mathrm{d}v = \int\limits_a \mathbf{T}(\vec{x},t)\vec{n}\mathrm{d}a + \int\limits_v \rho(\vec{x},t)\vec{k}(\vec{x},t)\mathrm{d}v \tag{2.42}$$

where $\vec{k}$ is the body force density in the current configuration. By the application of Gauss theorem along with the mass balance equation and Cauchy's theorem (2.33), the local form can be derived, see (Haupt, 2002),

$$\rho\dot{\vec{v}} = \operatorname{div}\mathbf{T} + \rho\vec{k}. \tag{2.43}$$

This is also known as equilibrium equation for $\dot{\vec{v}} = \vec{0}$.

The balance equation can also be represented in the reference configuration

$$\frac{\mathrm{d}}{\mathrm{d}t}\int\limits_V \rho_{\mathrm{R}}(\vec{X},t)\vec{V}(\vec{X},t)\mathrm{d}V = \int\limits_A \mathbf{T}_{\mathrm{R}}(\vec{X},t)\vec{n}_{\mathrm{R}}\mathrm{d}A + \int\limits_V \rho_{\mathrm{R}}(\vec{X},t)\vec{k}(\vec{X},t)\mathrm{d}V \tag{2.44}$$

which can be written in local form as

$$\rho_{\mathrm{R}}\dot{\vec{v}} = \operatorname{Div}\mathbf{T}_{\mathrm{R}} + \rho_{\mathrm{R}}\vec{k}. \tag{2.45}$$

$\operatorname{Div}$ represents the divergence in reference configuration whereas $\operatorname{div}$ represents the divergence in current configuration.

### 2.3.3. Balance of Angular Momentum

Similar to the balance of linear momentum, the balance of angular momentum states that the time rate of change of the total moment of momentum is equal to the moments exerted by the forces (body and surface) on the body. It is represented by

$$\frac{\mathrm{d}}{\mathrm{d}t}\int\limits_v (\vec{x}-\vec{c})\times\vec{v}\rho\mathrm{d}v = \int\limits_a (\vec{x}-\vec{c})\times\vec{t}\mathrm{d}a + \int\limits_v (\vec{x}-\vec{c})\times\vec{k}\rho\mathrm{d}v \tag{2.46}$$

where the torque applied is related to a fixed point $\vec{c}$ in space. Similar to the balance of linear momentum, by the application of Gauss theorem along with the mass balance equation and divergence theorem the local form can be derived,

$$\mathbf{T} = \mathbf{T}^T \tag{2.47}$$

which states the symmetry of the Cauchy stress tensor. This law provides little information for the formulation of boundary value problems. However, it provides certain restrictions on constitutive relations.

### 2.3.4. First Law of Thermodynamics - Balance of Energy

The first law of thermodynamics ensures that the energy is conserved. According to this law, the time rate of change of the total energy (kinetic and internal) of a body is equal to the rate at which work is done on the body (due to applied force both body and surface forces) and the rate at which heat is added to the body (volumetric as well as surface) by,

$$\frac{\mathrm{d}}{\mathrm{d}t}(K(\mathcal{B},t) + E(\mathcal{B},t)) = L(\mathcal{B},t) + Q(\mathcal{B},t). \tag{2.48}$$

Here, $K(\mathcal{B},t)$ is the kinetic energy of the body defined by

$$K(\mathcal{B},t) = \frac{1}{2}\int\limits_v \vec{v}(\vec{x},t)\cdot\vec{v}(\vec{x},t)\rho(\vec{x},t)\mathrm{d}v, \tag{2.49}$$

$E(\mathcal{B},t)$ is the internal energy which is defined as the volume integral of the internal energy density $e$,

$$E(\mathcal{B},t) = \int\limits_v \rho(\vec{x},t)e(\vec{x},t)\mathrm{d}v. \tag{2.50}$$

The mechanical power $L(\mathcal{B},t)$ due to applied force on the surface as well as the body force is defined as

$$L(\mathcal{B},t) = \int\limits_a \vec{t}\cdot\vec{v}\mathrm{d}a + \int\limits_v \vec{k}\cdot\rho\vec{v}\mathrm{d}v, \tag{2.51}$$

and the thermal energy $Q(\mathcal{B},t)$ by

$$Q(\mathcal{B},t) = \int\limits_a q(\vec{x},t)\mathrm{d}a + \int\limits_V \rho(\vec{x},t)r(\vec{x},t)\mathrm{d}v, \tag{2.52}$$

where $q(\vec{x},t)$ is the heat flux and $r(\vec{x},t)$ is the thermal energy production.

The conservation of energy can be written as

$$\frac{\mathrm{d}}{\mathrm{d}t}\left(\frac{1}{2}\int\limits_v \vec{v}\cdot\vec{v}\rho + \rho e\right)\mathrm{d}v = \int\limits_a \left(\vec{t}\cdot\vec{v} + q\right)\mathrm{d}a + \int\limits_v \left(\vec{k}\cdot\rho\vec{v} + \rho r\right)\mathrm{d}v \tag{2.53}$$

which, by the application of divergence theorem and application of the balance of linear and angular momentum, can be expressed in local form in current configuration as

$$\frac{\mathrm{d}}{\mathrm{d}t}e(\vec{x},t) = -\frac{1}{\rho}\operatorname{div}\vec{q}(\vec{x},t) + r(\vec{x},t) + \frac{1}{\rho}\mathbf{T}\cdot\mathbf{D}. \tag{2.54}$$

This is the energy equation, where $q = \vec{q}\cdot\vec{n}$. Here, $\mathbf{D}$ is the strain rate tensor which is defined as

$$\mathbf{D} = \frac{1}{2}(\mathbf{L} + \mathbf{L}^T) \tag{2.55}$$

where $\mathbf{L}$ is the spatial velocity gradient and is defined as

$$\mathbf{L} = \dot{\mathbf{F}}\mathbf{F}^{-1} = \operatorname{grad}\vec{v}(\vec{x},t). \tag{2.56}$$

### 2.3.5. Second Law of Thermodynamics - Balance of Entropy

A major drawback of the First law of thermodynamics is that it does not show the direction of heat flow. As long as the energy is conserved, the First law of thermodynamics does not enforce whether the heat is flowing from a cold to a hot object. Since this does not occur naturally, a second law is required to ensure that heat always flows from hot to cold objects. The second law of thermodynamics is also known as the principle of irreversibility. While the other balance equations led to different governing equations, this law is a restriction rather than a governing law. The entropy production of a closed system must always be non-negative. In simple words, it means that the entropy $S$ can within a closed system can never decrease. The entropy of a body can be expressed as

$$S(\mathcal{B},t) = \int_v s(\vec{x},t)\rho(\vec{x},t)\mathrm{d}v \tag{2.57}$$

where $s(\vec{x},t)$ is the specific entropy. The entropy supply $H$ from the surroundings is defined as

$$H = \int_a \Sigma\mathrm{d}a + \int_v \sigma\rho\mathrm{d}v = -\int_a \frac{\vec{q}}{\Theta}\cdot\vec{n}\mathrm{d}a + \int_v \frac{r}{\Theta}\rho\mathrm{d}v. \tag{2.58}$$

Here, $\Sigma$ is the surface component of the entropy supplied, $\vec{q}$ the heat flux vector and $\Theta$ the absolute temperature. $\sigma$ is the volume component of the entropy supplied. The entropy production is defined as

$$\Gamma = \int_v \gamma\rho\mathrm{d}v \geq 0. \tag{2.59}$$

The time rate of change of entropy is the sum of the entropy supply and the entropy production

$$\frac{\mathrm{d}}{\mathrm{d}t}S = H + \Gamma. \tag{2.60}$$

Since the entropy production $\Gamma$ is non-negative,

$$\Gamma = \dot{S} - H \geq 0. \tag{2.61}$$

This leads to a special form of the local entropy inequality.

$$\gamma = \dot{s} + \frac{1}{\rho\Theta}(\operatorname{div}\vec{q} - \rho r) - \frac{1}{\rho\Theta^2}\vec{q}\cdot\operatorname{grad}\Theta \geq 0 \tag{2.62}$$

which is rewritten in the Clausius-Duhem inequality

$$-\dot{\psi} - s\dot{\Theta} + \frac{1}{\rho}\mathbf{T}\cdot\mathbf{D} - \frac{1}{\rho\Theta}\vec{q}\cdot\operatorname{grad}\Theta \geq 0. \tag{2.63}$$

The Clausius-Duhem inequality provides the restriction that is essential to satisfy the condition of irreversibility. In order for the models to be thermodynamically consistent, the Clausius-Duhem inequality condition has to be satisfied.

# 3. Finite Element Method

In this chapter, the solution of the initial boundary value problem using the finite element method is explained in a nutshell. The basic equations and ideas are briefly discussed. For in-depth knowledge, the reader is advised to refer popular books on the topic like (Bathe, 2002; Zienkiewicz and Taylor, 2000b; Hughes, 1987; Wriggers, 2008).

In the studies conducted, the variational form of the balance of linear momentum being the first step is spatially discretized resulting in a system of DAE. For spatial discretization, the classical method is to divide the material body into discrete areas. The discretization can be linear or non-linear, see (Bathe, 2002; Zienkiewicz and Taylor, 2000b; Hughes, 1987; Wriggers, 2008). The method of vertical lines, see (Schiesser, 1991), is used here where first the spatial discretization is performed followed by the temporal discretization. The DAE-system is solved using the simple Backward-Euler scheme or high order time integration schemes to obtain a set of nonlinear equation systems. The high-order time integration schemes used are diagonally implicit Runge-Kutta (DIRK) methods (Hairer and Wanner, 1996). The use of Runge-Kutta procedures has inherent advantage of higher order time adaptivity, see (Ellsiepen and Hartmann, 2001). These non-linear equations are solved numerically using different widely known schemes like the Newton-Raphson scheme and the Multilevel Newton algorithm.

## 3.1. Initial Boundary Value Problem

The balance equations along with the constitutive equations on which the basics of continuum mechanics is developed cannot be solved analytically for real life problems. Only simple problems can be solved analytically. However, the complicated problems, called initial boundary value problems (so-called because the solution of such problems should also satisfy both the initial and the boundary conditions), are solved numerically using the finite element method. The most important condition of such problems is the well posedness. The initial boundary value problems should be well posed which implies the existence of a solution which is dependent on the boundary conditions.

The problem considered in this thesis is a quasi-static case and thereby the Right Hand Side RHS of the balance of linear momentum equation (2.43), vanishes leading to

$$\operatorname{div} \mathbf{T}(\vec{x}, t) + \rho \vec{k} = \vec{0}. \tag{3.1}$$

Of course, the constitutive equations representing the behavior of the material is definitely required to complete these equations. The second Piola-Kirchhoff stress tensor is used to define the elasticity relation and has the following structure

$$\widetilde{\mathbf{T}}(\vec{X}, t) = \widetilde{\mathbf{h}}(\mathbf{C}(\vec{X}, t), \mathbf{q}(\vec{X}, t)) \tag{3.2}$$

where

$$\dot{\mathbf{q}}(\vec{X},t) = \widetilde{\mathbf{r}}(\mathbf{C}(\vec{X},t), \mathbf{q}(\vec{X},t)) \tag{3.3}$$

is the corresponding evolution equation of the internal variables.

A large number of material models, like viscoelasticity, viscoplasticity etc., have such a structure consisting of an elasticity relationship (3.2), and its corresponding evolution equations (3.3). One of the most important aspect to formulate the initial boundary value problem is to know the boundary and initial conditions of the existing quantities. These can be formulated in either material or spatial representations. However, here only material representations are shown. The initial conditions for internal variables and displacements are formulated as

$$\mathbf{q}(\vec{X},t_0) = \mathbf{q}_0(\vec{X}) \quad \forall \vec{X} \in \mathcal{R}[\mathcal{B}], \tag{3.4}$$

$$\vec{u}(\vec{X},t_0) = \vec{u}_0(\vec{X}) \quad \forall \vec{X} \in \mathcal{R}[\mathcal{B}]. \tag{3.5}$$

Now, that the initial conditions are prescribed, it is also essential to describe the boundary conditions. There are three types of boundary conditions. In order to describe the boundary conditions, the boundary $\mathcal{R}[\mathcal{B}]$ is divided into different partial boundaries. The first kind of boundary condition called Dirichlet boundary condition or the geometric boundary condition $\delta_D\mathcal{R}[\mathcal{B}]$ describes the field variables like displacement or temperature etc. The second kind of boundary condition is called Neumann boundary condition $\delta_N\mathcal{R}[\mathcal{B}]$ that describes the directional derivatives of the field variables like tractions, heat flux etc. There is a third kind of boundary condition where both are connected like deformation dependent surface loads, convection called Robin boundary condition or mixed boundary condition (not applicable in this research work). $\delta_u\mathcal{R}[\mathcal{B}]$ denotes a partial boundary on which the displacements $\vec{u}(\vec{X},t)$ are specified. In addition, specified stress boundary conditions are conceivable on the boundary $\delta_s\mathcal{R}[\mathcal{B}]$. Both types of boundary conditions are mutually exclusive, i.e. either stress or displacement constraints can be specified

$$\delta_u\mathcal{R}[\mathcal{B}] \cup \delta_s\mathcal{R}[\mathcal{B}] = \delta\mathcal{R}[\mathcal{B}], \qquad \delta_u\mathcal{R}[\mathcal{B}] \cap \delta_s\mathcal{R}[\mathcal{B}] = \varnothing. \tag{3.6}$$

The Dirichlet boundary conditions are formulated on the boundary $\delta_u\mathcal{R}[\mathcal{B}]$,

$$\vec{u}(\vec{X},t) = \overline{\vec{u}}(\vec{X},t) \;\; \forall \vec{X} \in \delta_u\mathcal{R}[\mathcal{B}]. \tag{3.7}$$

The Neumann boundary conditions are formulated on the boundary $\delta_s\mathcal{R}[\mathcal{B}]$,

$$\vec{t}_{\mathrm{R}} = \mathbf{T}_{\mathrm{R}}\vec{n}_{\mathrm{R}} = \vec{s}(\vec{X},t) \quad \forall \vec{X} \in \delta_s\mathcal{R}[\mathcal{B}]. \tag{3.8}$$

The IBVP consists of a these initial and boundary conditions. Generally, it cannot be solved analytically. Thus, a numerical approximation is necessary. This forms the basis of finite element method. The initial and boundary conditions have been setup. The next step is the weak formulation of the momentum balance equation.

### Weak Formulation of the Momentum Balance

In material representation, Eq.(3.1) reads

$$\operatorname{Div} \mathbf{T}_{\mathrm{R}}(\vec{X}, t) + \rho_{\mathrm{R}} \vec{k} = \vec{0}. \tag{3.9}$$

The momentum balance equation is converted into weak formulation generally by applying principal of virtual displacements. There are alternative ways for weak formulation of the momentum balance equation (3.9), see (Hartmann, 2003). However, here only principal of virtual displacements is discussed. A test function (in this case virtual displacement) $\delta\vec{u}$ is multiplied with Eq.(3.9) and integrated over the entire volume to obtain

$$\int_V \Big( \operatorname{Div} \mathbf{T}_{\mathrm{R}}(\vec{X}, t) \cdot \delta\vec{u} + \rho_{\mathrm{R}} \vec{k} \cdot \delta\vec{u} \Big) \mathrm{d}V = 0. \tag{3.10}$$

These test functions vanish where Dirichlet boundary conditions are applied. With the help of Cauchy's theorem $\mathbf{T}_{\mathrm{R}} \vec{n}_{\mathrm{R}} = \vec{t}_{\mathrm{R}}$, the divergence theorem $\int \operatorname{Div}(\mathbf{T}_{\mathrm{R}}^{\mathrm{T}} \delta\vec{u}) \mathrm{d}V = \int (\mathbf{T}_{\mathrm{R}}^{\mathrm{T}} \delta\vec{u}) \cdot \vec{n}_{\mathrm{R}} \mathrm{d}A$, as well as the relation

$$\operatorname{Div} \mathbf{T}_{\mathrm{R}} \cdot \delta\vec{u} = \operatorname{Div}(\mathbf{T}_{\mathrm{R}}^{\mathrm{T}} \delta\vec{u}) - \mathbf{T}_{\mathrm{R}} \cdot \operatorname{Grad} \delta\vec{u}, \tag{3.11}$$

Eq.(3.10) can be reformulated as

$$\int_V \mathbf{T}_{\mathrm{R}} \cdot \operatorname{Grad} \delta\vec{u} \mathrm{d}V = \int_{\delta V} \vec{t}_{\mathrm{R}} \cdot \delta\vec{u} \mathrm{d}A + \int_V \rho_{\mathrm{R}} \vec{k} \cdot \delta\vec{u} \mathrm{d}V. \tag{3.12}$$

Applying the relation between first and second PK stress tensor $\mathbf{T}_{\mathrm{R}} = \mathbf{F}\widetilde{\mathbf{T}}$ to the above equation leads to

$$\int_V \widetilde{\mathbf{T}} \cdot \delta\mathbf{E} \mathrm{d}V = \int_{\delta V} \vec{t}_{\mathrm{R}} \cdot \delta\vec{u} \mathrm{d}\mathrm{d}A + \int_V \rho_{\mathrm{R}} \vec{k} \cdot \delta\vec{u} \mathrm{d}V. \tag{3.13}$$

For a more detailed derivation of Eq.(3.13), the reader is referred to (Quint, 2012; Rothe, 2014; Grafenhorst, 2018). The virtual strain $\delta\mathbf{E}$ describe the variation of the Green strain tensor and is given by

$$\delta\mathbf{E} = \frac{1}{2} \Big( \mathbf{F}^{\mathrm{T}} \operatorname{Grad} \delta\vec{u} + (\operatorname{Grad} \delta\vec{u})^{\mathrm{T}} \mathbf{F} \Big). \tag{3.14}$$

## 3.2. Solution Procedure: Method of Vertical Lines

The weak formulation (3.13) cannot be solved analytically in most real world problems and so numerical methods are applied to solve these problems. There are different ways to solve these problems and that forms the basis of finite elements. In this research work, the so-called method of vertical lines (MOL) is utilized to solve the problem. The MOL is a technique used to solve initial boundary value problems, in which the partial differential equations are converted into a system of ordinary differential equations (depending on the PDE) by spatially discretizing all

but one variable (time $t$), see (Schiesser, 1991). It can be shown that this system of differential equations in connection with the finite element method is a system of differential-algebraic equations. In Brenan et al. (1996), Ascher and Petzold (1998), Hairer et al. (1993), Hairer and Wanner (1996) and Rentrop et al. (1995) different approaches to solve systems of DAEs are presented. The second step is to do a temporal discretization leading to a set of non linear equations. By using the MOL, it is possible, in addition to using numerical methods like the most popular Newton-Raphson scheme, to use higher order time integration methods. Thus, diagonal-implicit Runge-Kutta methods can be used in the finite element method, see (Ellsiepen and Hartmann, 2001), (Hartmann, 2002) and (Bier and Hartmann, 2006), (Hartmann and Bier, 2008). A much more detailed and comprehensive outlook on the different aspects of the solution procedure is explained in (Hartmann, 2003).

## 3.3. Space Discretization

The integral form or the weak form needs to be solved numerically and hence the integrals are converted to a summation by discretizing the domain into finite elements with the corner points of each elements are known as the nodes (totally $n_n$ number of nodes). The entire domain $\mathcal{B}$ is approximated into a region $\mathcal{B}^h$ which is constituted of non-overlapping $n_e$ elements $\Omega_e \subset \mathcal{B}^h$, see Fig. 3.1. Typically for a three dimensional problem, tetrahedral and hexahedral elements are used

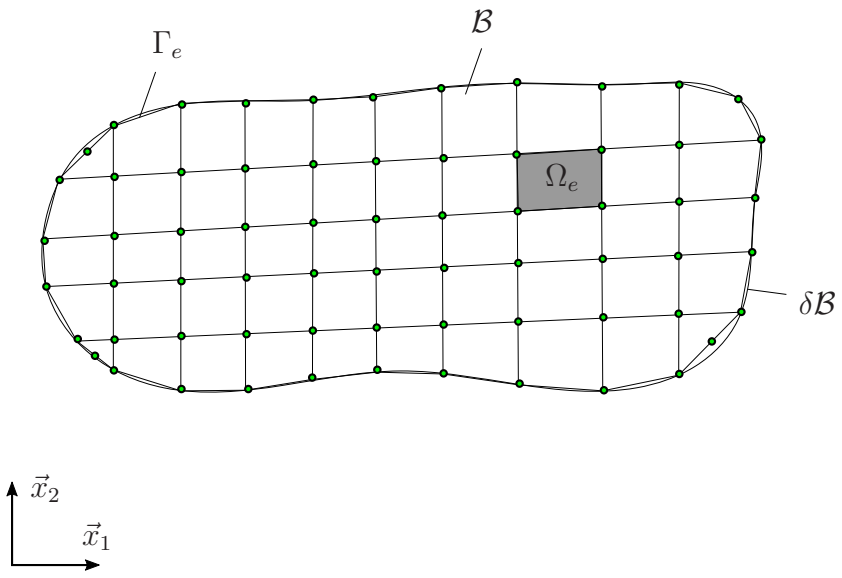


Figure 3.1.: Spatial discretization with finite elements

either in a *linear* or a *quadratic* sense. The terms linear and quadratic are attributed to the shape functions that are used (explained later in the section). For a detailed mathematical explanation of the different aspects of spatial discretization please refer (Bathe, 2002), (Zienkiewicz and Taylor, 2000b) and (Hughes, 1987).

The unknown values are calculated at the nodes. Certain interpolation functions are defined for each element to interpolate the values inside the element using the values calculated at nodes. These interpolation functions are called shape functions or ansatz functions. In finite elements, all the field variables need to be discretized. In this study, the field variable is the displacement $\vec{u}$. Not only is the field variable discretized, the virtual field variable is also discretized. The discretized variables are $\mathbf{u}^h \in \mathbb{R}^3$ and $\delta\mathbf{u}^h \in \mathbb{R}^3$ described on the nodes of the elements with the help of shape functions $N_a$ connected to particular node $a$

$$\vec{u}(\vec{x},t) \approx \mathbf{u}^h(\mathbf{x}^h,t) = \sum_{a=1}^{n_n} N_a(\mathbf{x}^h)\mathbf{u}_a^h(t) \tag{3.15}$$

$$\delta\vec{u}(\vec{x}) \approx \delta\mathbf{u}^h(\mathbf{x}^h) = \sum_{a=1}^{n_n} N_a(\mathbf{x}^h)\delta\mathbf{u}_a^h. \tag{3.16}$$

Here, $\mathbf{u}_a^h(t)$ and $\delta\mathbf{u}_a^h$ are the nodal displacements and the virtual nodal displacements respectively. In this research work, isoparametric formulation is followed which implies the usage of same shape functions for elements and for interpolation of the displacement field variable. Normally for the shape function, Lagrangian polynomials are selected and the elements of the reference configuration $\Omega_e$ or current configuration $\omega_e$ are transformed into a normed reference element $\Omega_\square$ using the local coordinates $\boldsymbol{\xi} = \{\xi,\eta,\zeta\}^T$,

$$\mathbf{x} = \chi_t^e(\boldsymbol{\xi}) \Leftrightarrow \boldsymbol{\xi} = \varphi_t^e(\mathbf{x}), \quad \mathbf{X} = \chi_{\mathrm{R}}^e(\boldsymbol{\xi}) \Leftrightarrow \boldsymbol{\xi} = \varphi_{\mathrm{R}}^e(\mathbf{X}), \tag{3.17}$$

where $\xi \in [-1,1]$, $\eta \in [-1,1]$ and $\zeta \in [-1,1]$, see Fig. 3.2. For the transformation of reference to the normed element, a quantity known as Jacobian $\mathbf{J}^e$ is used with $\det \mathbf{J}^e > 0$. For the transformation of current configurations to the normed element, the Jacobian $\mathbf{j}^e$ is used where $\det \mathbf{j}^e > 0$. The Jacobians are defined as

$$\mathbf{J}^e = \left[\frac{\mathrm{d}\mathbf{X}}{\mathrm{d}\boldsymbol{\xi}}\right] = \mathrm{Grad}_\xi\, \mathbf{X}, \quad \mathbf{j}^e = \left[\frac{\mathrm{d}\mathbf{x}}{\mathrm{d}\boldsymbol{\xi}}\right] = \mathrm{Grad}_\xi\, \mathbf{x}. \tag{3.18}$$

For the transference of the discretized equations to the normed element, a transformation of line elements are performed by using

$$\mathrm{d}\mathbf{X} = \mathbf{J}^e \mathrm{d}\boldsymbol{\xi}, \quad \mathrm{d}\mathbf{x} = \mathbf{j}^e \mathrm{d}\boldsymbol{\xi}, \quad \mathrm{d}\mathbf{x} = \mathbf{F}^e \mathrm{d}\mathbf{X} \ \text{ where } \ \mathbf{F}^e = \mathbf{j}^e \mathbf{J}^{e-1}. \tag{3.19}$$

The shape function has to follow certain property known as partition of unity. According to partition of unity, the shape function $N_a$ is 1 at a node $a$ and 0 at the other nodes. This implies that at a particular node $a$, only one shape function has the value of 1. In addition to this property, the sum of shape functions has to be one within an element.

Using all these concepts, the shape functions for the displacements $\vec{u}(\vec{x},t)$ as well as virtual displacements $\delta\vec{u}(\vec{x})$ within each element $e$ are introduced,

$$\mathbf{u}^h(\mathbf{x},t) = \mathbf{N}_{\mathrm{u}}^e(\varphi^e(\mathbf{x}))\mathbf{u}^e(t) = \mathbf{N}_{\mathrm{u}}^e(\varphi^e(\mathbf{x}))\boldsymbol{Z}_{\mathrm{a}}^e \boldsymbol{u}^{\mathrm{a}} = \mathbf{N}_{\mathrm{u}}^e(\varphi^e(\mathbf{x}))\{\boldsymbol{Z}_{\mathrm{u}}^e \boldsymbol{u} + \overline{\boldsymbol{Z}}_{\mathrm{u}}^e \overline{\boldsymbol{u}}(t)\} \tag{3.20}$$

$$\delta\mathbf{u}^h(\mathbf{x}) = \mathbf{N}_{\mathrm{u}}^e(\varphi^e(\mathbf{x}))\delta\mathbf{u}^e = \mathbf{N}_{\mathrm{u}}^e(\varphi^e(\mathbf{x}))\boldsymbol{Z}_{\mathrm{a}}^e \delta\boldsymbol{u}^{\mathrm{a}} = \mathbf{N}_{u}^e(\varphi^e(\mathbf{x}))\boldsymbol{Z}_{\mathrm{u}}^e \delta\boldsymbol{u}. \tag{3.21}$$

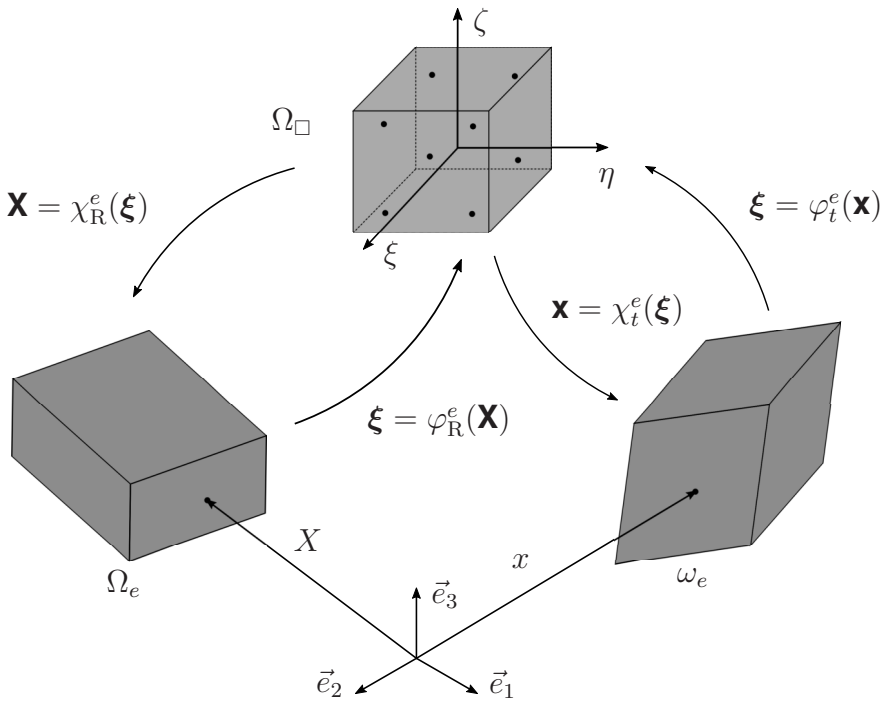


Figure 3.2.: Isoparametric transformation of a linear hexahedral element into the reference volume

Here, $\mathbf{N}^e_{\mathrm{u}} \in \mathbb{R}^{3\times n^e_{\mathrm{u}}}$ is the matrix of shape functions related to the displacements with $n^e_{\mathrm{u}}$ being the element degrees of freedom (DOF). $\boldsymbol{u}_{\mathrm{a}} \in \mathbb{R}^{n^e_{\mathrm{ua}}}$ is the displacement DOF of the entire mesh. The displacement DOF of the entire mesh is divided into unknown DOF $\boldsymbol{u} \in \mathbb{R}^{n_{\mathrm{u}}}$ and prescribed DOF $\overline{\boldsymbol{u}} \in \mathbb{R}^{n_{\mathrm{p}}}$. It can be seen here that $n_{\mathrm{a}} = n_{\mathrm{u}} + n_{\mathrm{p}}$ with $\boldsymbol{u}_{\mathrm{a}}{}^{\mathrm{T}} = \{\boldsymbol{u}^{\mathrm{T}} \;\; \overline{\boldsymbol{u}}^{\mathrm{T}}\}$. It is essential to define a variable to assemble the discretized field variable from the local variables within the element to global variables. For this purpose, the so-called incidence matrices $\boldsymbol{Z}^e_{\mathrm{u}} \in \mathbb{R}^{n^e_{\mathrm{u}}\times n_{\mathrm{u}}}$ and $\overline{\boldsymbol{Z}}^e_{\mathrm{u}} \in \mathbb{R}^{n^e_{\mathrm{u}}\times n_{\mathrm{p}}}$ are defined. The incidence matrices are merely composed of zeros and ones and basically functions as a filter to help with formal assembly and are thus not programmed, see (Hartmann, 2003). However, the introduction of incidence matrices aided in the development of new finite element schemes, see (Hartmann and Hamkar, 2010) and (Hartmann, 2005).

Now that the basics of the discretization procedure is detailed, Eq.(3.13) can be discretized

$$\widetilde{\pi}_{\mathrm{M}}(\vec{u}, \mathbf{q}, \delta\vec{u}, t) \rightarrow \widetilde{\pi}^h_{\mathrm{M}}(\boldsymbol{u}^h, \boldsymbol{q}, \delta\boldsymbol{u}^h, t). \tag{3.22}$$

In finite elements, the second Piola Kirchhoff stress tensor is expressed in Voigt notation

$$\widetilde{\mathbf{T}} = \{\widetilde{T}_{11} \;\; \widetilde{T}_{22} \;\; \widetilde{T}_{33} \;\; \widetilde{T}_{12} \;\; \widetilde{T}_{23} \;\; \widetilde{T}_{31}\}^{\mathrm{T}} \tag{3.23}$$

with the discretized form being

$$\widetilde{\mathbf{T}}^e = \mathbf{h}^e(\mathbf{C}^e(\mathbf{X}, t), \mathbf{q}^e(\mathbf{X}, t)). \tag{3.24}$$

Similarly, the virtual strain tensor can also be expressed as

$$\delta\mathbf{E} = \{\delta E_{11} \;\; \delta E_{22} \;\; \delta E_{33} \;\; 2\delta E_{12} \;\; 2\delta E_{23} \;\; 2\delta E_{31} \;\}^{\mathrm{T}} = \widetilde{\mathbf{B}}_{\mathrm{u}}\delta\mathbf{u}^{e}, \tag{3.25}$$

where $n_{en}$ is the number of nodes per element (for this thesis, $n_{en} = 8$ for linear elements and $n_{en} = 20$ for quadratic elements). The factor two in the shear components is to ensure that the scalar product in tensor and vector notation are identical, $\widetilde{\mathbf{T}} \cdot \delta\mathbf{E} = \delta\mathbf{E}^{\mathrm{T}}\widetilde{\mathbf{T}}$. Here, a matrix $\widetilde{\mathbf{B}}_{\mathrm{u}} = [\widetilde{\mathbf{B}}_{\mathrm{u}1}...\widetilde{\mathbf{B}}_{\mathrm{u}n_{en}}] \in \mathbb{R}^{6\times 3n_{\mathrm{u}}^{e}}$ called strain-displacement matrix for each node $a$ is introduced which contains the derivative of the shape functions with respect to the material coordinates. The discretized weak form of the momentum balance equation is obtained by the application of ansatz functions for displacement and virtual displacement, Eq.(3.20),(3.21), reads

$$\widetilde{\pi}_{\mathrm{M}}^{h}(\boldsymbol{u}^{h}, \boldsymbol{q}, \delta\boldsymbol{u}^{h}, t) = \delta\boldsymbol{u}^{\mathrm{T}} \sum_{e=1}^{n_e} \left\{ \boldsymbol{Z}_{\mathrm{u}}^{e^{\mathrm{T}}} \int_{\Omega_e} \widetilde{\mathbf{B}}_{\mathrm{u}}^{\;e^{\mathrm{T}}}(\boldsymbol{u}^{e}(t), \mathbf{X})\widetilde{\mathbf{T}}^{e}(\mathbf{X}, t)\mathrm{d}\Omega_e - \overline{\boldsymbol{p}}(t) \right\} \tag{3.26}$$

$$= \delta\boldsymbol{u}^{\mathrm{T}} \sum_{e=1}^{n_e} \left\{ \boldsymbol{Z}_{\mathrm{u}}^{e^{\mathrm{T}}} \int_{\Omega_e} \widetilde{\mathbf{B}}_{\mathrm{u}}^{\;e^{\mathrm{T}}}(\boldsymbol{u}^{e}(t), \mathbf{X})\mathbf{h}^{e}(\mathbf{C}^{e}(\mathbf{X}, t), \mathbf{q}^{e}(\mathbf{X}, t))\mathrm{d}\Omega_e - \overline{\boldsymbol{p}}(t) \right\}. \tag{3.27}$$

$\overline{\boldsymbol{p}}(t)$ is a vector containing the volume distributed loads and the tractions acting on the surface

$$\overline{\boldsymbol{p}}(t) := \int_{\Omega_e} \mathbf{N}_{\mathrm{u}}^{e\mathrm{T}}(\mathbf{X})\rho_{\mathrm{R}}(\mathbf{X})\mathbf{k}^{e}\mathrm{d}\Omega_e + \int_{\Gamma_e} \mathbf{N}_{\mathrm{u}}^{e\mathrm{T}}(\mathbf{X})\mathbf{s}(\mathbf{X}, t)\mathrm{d}\Gamma_e. \tag{3.28}$$

Due to the fact that the virtual displacements are arbitrary, $\delta\boldsymbol{u}_{\mathrm{a}}^{\mathrm{T}} = \{\delta\boldsymbol{u}^{\mathrm{T}} \;\; \delta\overline{\boldsymbol{u}}^{\mathrm{T}}\} = \{\delta\boldsymbol{u}^{\mathrm{T}} \;\; \boldsymbol{0}\}$, Eq.(3.26) yields a system of nonlinear equations

$$\widetilde{\boldsymbol{g}}_{\mathrm{u}}(\boldsymbol{u}, \boldsymbol{q}, t) = \sum_{e=1}^{n_e} \left\{ \boldsymbol{Z}_{\mathrm{u}}^{e^{\mathrm{T}}} \int_{\Omega_e} \widetilde{\mathbf{B}}_{\mathrm{u}}^{\;e^{\mathrm{T}}}(\boldsymbol{u}^{e}(t), \mathbf{X})\widetilde{\mathbf{T}}^{e}(\mathbf{X}, t)\mathrm{d}\Omega_e \right\} - \overline{\boldsymbol{p}}(t) = \boldsymbol{0}. \tag{3.29}$$

This equation is expressed with quantities relative to the reference configuration and can be expressed with quantities relative to the current configuration with the help of the push-forward operator in matrix form $\mathbf{F}_{23}^{e}$ by using the equation $\mathbf{S}^{e} = \mathbf{F}_{23}^{e}\widetilde{\mathbf{T}}^{e}$, see (Hartmann, 2003), with $\mathbf{S}^{e}$ being the weighted Cauchy stress. The equation in current configuration is expressed as

$$\boldsymbol{g}_{\mathrm{u}}(\boldsymbol{u}, \boldsymbol{q}, t) = \sum_{e=1}^{n_e} \left\{ \boldsymbol{Z}_{\mathrm{u}}^{e^{\mathrm{T}}} \int_{\Omega_e} \mathbf{B}_{\mathrm{u}}^{\;e^{\mathrm{T}}}(\boldsymbol{u}^{e}(t), \mathbf{x})\mathbf{S}^{e}(\mathbf{x}, t)\mathrm{d}\Omega_e \right\} - \overline{\boldsymbol{p}}(t) = \boldsymbol{0}. \tag{3.30}$$

The same equation expressed in reference configuration is

$$\boldsymbol{g}_{\mathrm{u}}(\boldsymbol{u}, \boldsymbol{q}, t) = \sum_{e=1}^{n_e} \left\{ \boldsymbol{Z}_{\mathrm{u}}^{e^{\mathrm{T}}} \int_{\Omega_e} \mathbf{B}_{\mathrm{u}}^{e\mathrm{T}}(\boldsymbol{u}^{e}(t), \mathbf{X})\mathbf{F}_{23}^{e}\widetilde{\mathbf{T}}^{e}(\mathbf{X}, t)\mathrm{d}\Omega_e \right\} - \overline{\boldsymbol{p}}(t) = \boldsymbol{0}. \tag{3.31}$$

The strain-displacement matrix $\widetilde{\mathbf{B}}^e_{\mathrm{u}}(\varphi^e(\mathbf{x}))$ is the derivative of the shape functions with respect to spatial coordinates and for 3D cases is defined as

$$\widetilde{\mathbf{B}}^e_{\mathrm{u}}(\varphi^e(\mathbf{x})) = [\widetilde{\mathbf{B}}^e_{\mathrm{u}1}...\widetilde{\mathbf{B}}^e_{\mathrm{u}n_{en}}] \in \mathbb{R}^{6\times 3n^e_{\mathrm{u}}}, \tag{3.32}$$

with each $\widetilde{\mathbf{B}}^e_{\mathrm{ua}}$ being

$$\begin{bmatrix} N^e_{\mathrm{u}a,x} & 0 & 0 \\ 0 & N^e_{\mathrm{u}a,y} & 0 \\ 0 & 0 & N^e_{\mathrm{u}a,z} \\ N^e_{\mathrm{u}a,y} & N^e_{\mathrm{u}a,x} & 0 \\ 0 & N^e_{\mathrm{u}a,z} & N^e_{\mathrm{u}a,y} \\ N^e_{\mathrm{u}a,z} & 0 & N^e_{\mathrm{u}a,x} \end{bmatrix}, \qquad a = 1, ..., n_{en}. \tag{3.33}$$

The shape function $N^e_{\mathrm{u}a}(\boldsymbol{\xi})$ is defined at the node $a$ within the domain $\Omega_\square$ with the local coordinates $\boldsymbol{\xi}$. The integration part in the Eq.(3.31) is numerically performed within each element using the well known Gauss quadrature rule, $\int_{-1}^{1} f(x)dx \approx \sum_{i=1}^{n} w_i f(x_i)$, see (Dhatt and Touzot, 1985) and (Schwarz and Köckler, 2013), resulting in

$$\boldsymbol{g}_{\mathrm{u}}(\boldsymbol{u}(t), \boldsymbol{q}(t), t) = \sum_{e=1}^{n_e} \boldsymbol{Z}_{\mathrm{u}}^{e^{\mathrm{T}}} \left\{ \sum_{i=1}^{n_\xi} \sum_{j=1}^{n_\eta} \sum_{k=1}^{n_\zeta} w_i w_j w_k \mathbf{B}_{\mathrm{u}}^{e^{\mathrm{T}}}(\boldsymbol{\xi}) \mathbf{S}^e(\boldsymbol{\xi}, t) \det \mathbf{J}^e(\boldsymbol{\xi}) \right\} - \overline{\boldsymbol{p}}(t) = \boldsymbol{0} \tag{3.34}$$

where $\boldsymbol{\xi}^{\mathrm{T}} = \{\xi_i, \eta_j, \zeta_k\}$ are the so-called Gauss points (integration points at which stresses and strains are calculated in finite elements) coordinates with the corresponding weighting factors $w_i$, $w_j$ and $w_k$ having $n_\xi$, $n_\eta$ and $n_\zeta$ in each local coordinate directions. Totally, there are $n_{\mathrm{GP}} = n_e \times n_\xi \times n_\eta \times n_\zeta$ number of Gauss points in the entire domain. $\mathbf{J}^e$ is the Jacobian to transform the coordinates from local to global coordinates.

Using the discretization Eq.(3.34), the internal variables are calculated at the Gauss points $\boldsymbol{\xi}_{ijk}$ so that the evolution equation (3.3) becomes

$$\dot{\mathbf{q}}^e(\boldsymbol{\xi}_{ijk}, t) = \tilde{\mathbf{r}}(\mathbf{C}(\boldsymbol{\xi}_{ijk}, t), \mathbf{q}^e(\boldsymbol{\xi}_{ijk}, t)), \quad \mathbf{q}^e \in \mathbb{R}^{n_q}. \tag{3.35}$$

The internal variables are formally assembled into a global vector $\boldsymbol{q}(t)$ with a length of $n_{\mathrm{Q}} = n_e \times n_{\mathrm{GP}} \times n_q$, where $n_q$ is the number of internal variables in each Gauss point and $n_{\mathrm{GP}}$ being the number of Gauss points in each element. Similar to the filtering of the displacements of each nodes from the global vector, an incidence matrix $\boldsymbol{Z}^e_q \in \mathbb{R}^{n_q \times n_{\mathrm{Q}}}$ is defined for internal variables also. The incidence matrix $\boldsymbol{Z}^e_q$ extracts the internal variable of each Gauss point of an element from the globally assembled vector $\boldsymbol{q}(t)$ by

$$\mathbf{q}^e(t) = \boldsymbol{Z}^e_q \boldsymbol{q}(t) \quad \mathbf{q}^e(\boldsymbol{\xi}, t) \in \mathbb{R}^{n_q}. \tag{3.36}$$

The assembly procedure of the internal variables is shown in Fig.3.3. Since the internal variables and their corresponding evolution equations are decoupled at each Gauss point, Eq.(3.36) can be inverted,

$$\boldsymbol{q}(t) = \sum_{e=1}^{n_e} \sum_{l=1}^{n_{\mathrm{GP}}} \boldsymbol{Z}_q^{e^{\mathrm{T}}} \mathbf{q}^e(\boldsymbol{\xi}_l, t). \tag{3.37}$$

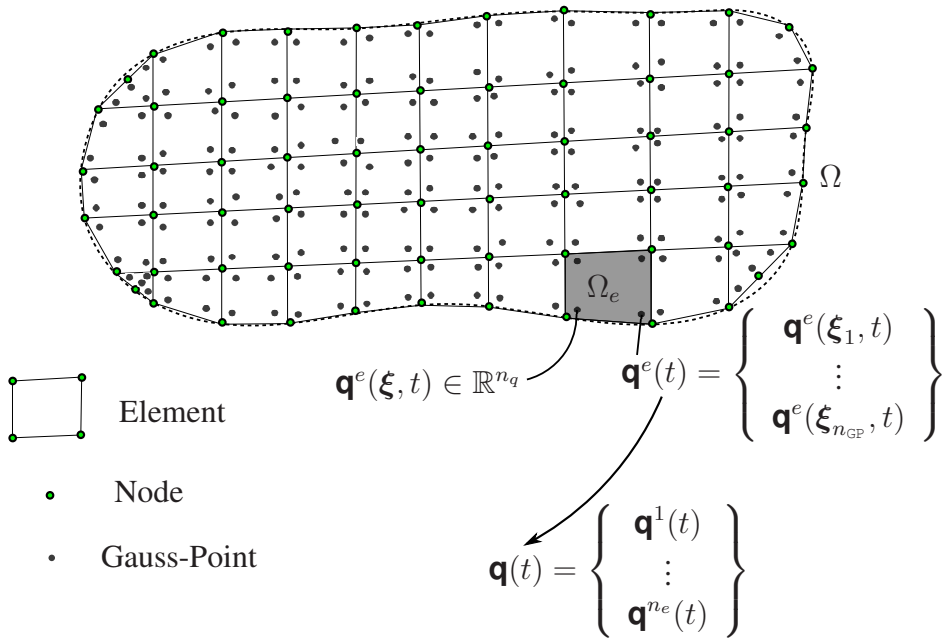


Figure 3.3.: Formal assembly of internal variables

Thus, the internal variables are calculated at each Gauss point and then formally assembled as a system of ordinary differential equations of first order which depends on the displacements $\boldsymbol{u}(t)$,

$$\dot{\boldsymbol{q}}(t) - \boldsymbol{r}(t, \boldsymbol{u}(t), \boldsymbol{q}(t)) = \boldsymbol{0}, \quad \boldsymbol{q}(t) \in \mathbb{R}^{n_{\text{Q}}}. \tag{3.38}$$

Eqs.(3.34) and (3.38) represent a DAE-system,

$$\boldsymbol{F}(t, \boldsymbol{y}(t), \dot{\boldsymbol{y}}(t)) \equiv \left\{ \begin{array}{c} \boldsymbol{g}(t, \boldsymbol{u}(t), \boldsymbol{q}(t)) \\ \dot{\boldsymbol{q}}(t) - \boldsymbol{r}(t, \boldsymbol{u}(t), \boldsymbol{q}(t)) \end{array} \right\} = \boldsymbol{0}. \tag{3.39}$$

A main disadvantage of the application of principal of virtual displacements is that the reaction forces cannot be calculated at the degrees of freedom where the displacements are prescribed. This is due to the fact that these degrees of freedom produce no virtual work. To circumvent this disadvantage, another variational principle called *Lagrange multiplier method* is used, see (Hartmann, 2003) and (Hartmann et al., 2008). In this method, to account for the geometrical boundary conditions, a constraint condition is formulated,

$$\boldsymbol{C}_{\text{c}}(\boldsymbol{u}_{\text{a}}) = \hat{\boldsymbol{u}} - \overline{\boldsymbol{u}} = \boldsymbol{M}^T \boldsymbol{u}_{\text{a}} - \overline{\boldsymbol{u}} = \boldsymbol{0}, \quad \text{with} \quad \boldsymbol{M} = \left[ \begin{array}{c} \boldsymbol{0}_{n_{\text{u}} \times n_{\text{p}}} \\ \\ \boldsymbol{I}_{n_{\text{p}}} \end{array} \right]. \tag{3.40}$$

$\boldsymbol{u}_{\text{a}}^T = \{\boldsymbol{u}^T, \hat{\boldsymbol{u}}^T\}$ is a vector of all nodal displacements which consists of unknown nodal displacements $\boldsymbol{u} \in \mathbb{R}^{n_{\text{u}}}$ as well as the degrees of freedom, $\hat{\boldsymbol{u}}$, where the displacements $\overline{\boldsymbol{u}} \in \mathbb{R}^{n_{\text{p}}}$ are prescribed. However, in the Lagrange multiplier method, the nodal displacement vector $\boldsymbol{u}_{\text{a}}^T$ is assumed to be unknown. The incidence matrix $\boldsymbol{M} \in \mathbb{R}^{(n_{\text{u}}+n_{\text{p}}) \times n_{\text{p}}}$ differentiates between known and

unknown displacements. In order to enforce the prescribed displacements $\overline{\boldsymbol{u}}$, the Lagrange multiplier vector $\boldsymbol{\lambda} \in \mathbb{R}^{n_\mathfrak{p}}$ is introduced and is interpreted as reaction forces vector. The application of this method transforms the Eq.(3.39) to

$$\boldsymbol{F}(t, \boldsymbol{y}(t), \dot{\boldsymbol{y}}(t)) \equiv \left\{ \begin{array}{c} \boldsymbol{g}_{\mathrm{a}}(t, \boldsymbol{u}_{\mathrm{a}}(t), \boldsymbol{q}(t)) + \boldsymbol{M}\boldsymbol{\lambda}(t) \\ \boldsymbol{C}_c(t, \boldsymbol{u}_{\mathrm{a}}(t)) \\ \dot{\boldsymbol{q}}(t) - \boldsymbol{r}(\boldsymbol{u}_{\mathrm{a}}(t), \boldsymbol{q}(t)) \end{array} \right\} = \boldsymbol{0} \tag{3.41}$$

where $\boldsymbol{y}^T(t) = \{\boldsymbol{u}_{\mathrm{a}}^T(t), \boldsymbol{\lambda}^T(t), \boldsymbol{q}^T(t)\}$ with the following initial conditions,

$$\boldsymbol{y}(t_0) \equiv \left\{ \begin{array}{c} \boldsymbol{u}_{\mathrm{a}}(t_0) \\ \boldsymbol{\lambda}(t_0) \\ \boldsymbol{q}(t_0) \end{array} \right\} = \left\{ \begin{array}{c} \boldsymbol{u}_{\mathrm{a}0} \\ \boldsymbol{\lambda}_0 \\ \boldsymbol{q}_0 \end{array} \right\} \equiv \boldsymbol{y}_0. \tag{3.42}$$

The DAE-system introduced by Eq.(3.41) is now discretized in the temporal domain according to the method of vertical lines.

## 3.4. Time Discretization

In most of the commercial softwares like Abaqus Implicit or Ansys, the temporal discretization is performed using Backward-Euler scheme. As a starting step, here also the Backward-Euler scheme is applied to the DAE-system (3.41). This results in the nonlinear system

$$\begin{aligned} \boldsymbol{g}\big(t_{n+1}, \boldsymbol{u}_{n+1}, \hat{\boldsymbol{u}}_{n+1}, \boldsymbol{q}_{n+1}\big) &= \boldsymbol{0}, \\ \overline{\boldsymbol{g}}\big(\boldsymbol{u}_{n+1}, \hat{\boldsymbol{u}}_{n+1}, \boldsymbol{q}_{n+1}\big) + \boldsymbol{\lambda}_{n+1} &= \boldsymbol{0}, \\ \boldsymbol{C}_c\big(t_{n+1}, \hat{\boldsymbol{u}}_{n+1}\big) &= \boldsymbol{0}, \\ \boldsymbol{I}\big(\boldsymbol{u}_{n+1}, \hat{\boldsymbol{u}}_{n+1}, \boldsymbol{q}_{n+1}\big) &= \boldsymbol{0}, \end{aligned} \tag{3.43}$$

with

$$\boldsymbol{I}\big(\boldsymbol{u}_{n+1}, \hat{\boldsymbol{u}}_{n+1}, \boldsymbol{q}_{n+1}\big) = \boldsymbol{q}_{n+1} - \boldsymbol{q}_n - \Delta t_n \, \boldsymbol{r}\big(\boldsymbol{u}_{n+1}, \hat{\boldsymbol{u}}_{n+1}, \boldsymbol{q}_{n+1}\big) \tag{3.44}$$

at each point in time $t_{n+1}$, $0 \leq t_{n+1} \leq T$, $t_{n+1} = t_n + \Delta t_n$, where $\Delta t_n$ is the step-size. It has to be noted that in other time integration schemes, the final iterated solution $\hat{\boldsymbol{u}} = \overline{\boldsymbol{u}}$ may not be reached, see (Hartmann and Hamkar, 2010). In the case of MLNA, the system (3.43) can be rewritten as

$$\begin{aligned} \boldsymbol{g}\big(t_{n+1}, \boldsymbol{u}_{n+1}, \boldsymbol{q}_{n+1}\big) &= \boldsymbol{0}, \\ \overline{\boldsymbol{g}}\big(\boldsymbol{u}_{n+1}, \boldsymbol{q}_{n+1}\big) + \boldsymbol{\lambda}_{n+1} &= \boldsymbol{0}, \\ \boldsymbol{I}\big(\boldsymbol{u}_{n+1}, \boldsymbol{q}_{n+1}\big) &= \boldsymbol{0}. \end{aligned} \tag{3.45}$$

under the assumption that $\hat{\boldsymbol{u}}$ is prescribed. The system of nonlinear equations (3.45) is solved using the Multilevel-Newton algorithm except for the second equation $(3.45)_2$. This is rather explicit in $\boldsymbol{\lambda}_{n+1}$ and hence is a downstream step. The Multilevel-Newton algorithm will be discussed in detail in the next section. Since it is called consistent initial conditions problem, see

(Hairer et al., 1993), the DAE-system (3.45) is also valid at the initial time $t_0$. For constitutive relations without any internal variables, like hyperelasticity etc., Eq.(3.45) reduces to

$$\begin{aligned} \boldsymbol{g}\big(t_{n+1}, \boldsymbol{u}_{n+1}\big) &= \boldsymbol{0}, \\ \overline{\boldsymbol{g}}\big(\boldsymbol{u}_{n+1}\big) + \boldsymbol{\lambda}_{n+1} &= \boldsymbol{0}. \end{aligned} \tag{3.46}$$

This system of non-linear equation $(3.46)_1$ can then be solved using the classical Newton-Raphson method.

## Diagonally-Implicit Runge-Kutta Methods

In finite elements, it is quite common to solve the DAE-system using the Diagonally-Implicit Runge-Kutta Methods. Even the Backward-Euler (also known as implicit Euler method) is a special case of the class of Runge-Kutta methods. Though the basics of DIRK-methods are discussed here, for more comprehensive explanation, refer to (Hairer et al., 1993; Hairer and Wanner, 1996; Hartmann, 2003). The DAE-system (3.41) can be solved using DIRK-methods and is explained here. In comparison to the Backward-Euler scheme, in addition to the step-size $\Delta t_n$ , different stages $s$ are introduced (number of stages can be varied upon the order of the time integration scheme used), where the stage values (function values at integration points)

$$\begin{aligned} \boldsymbol{g}\big(T_{ni}, \boldsymbol{U}_{ni}, \hat{\boldsymbol{U}}_{ni}, \boldsymbol{Q}_{ni}\big) &= \boldsymbol{0}, \\ \overline{\boldsymbol{g}}\big(\boldsymbol{U}_{ni}, \hat{\boldsymbol{U}}_{ni}, \boldsymbol{Q}_{ni}\big) + \boldsymbol{\Lambda}_{ni} &= \boldsymbol{0}, \\ \boldsymbol{C}_c\big(T_{ni}, \hat{\boldsymbol{U}}_{ni}\big) &= \boldsymbol{0}, \\ \boldsymbol{I}\big(\boldsymbol{U}_{ni}, \hat{\boldsymbol{U}}_{ni}, \boldsymbol{Q}_{ni}\big) &= \boldsymbol{0}, \end{aligned} \tag{3.47}$$

with

$$\boldsymbol{I}\big(\boldsymbol{U}_{ni}, \hat{\boldsymbol{U}}_{ni}, \boldsymbol{Q}_{ni}\big) = \boldsymbol{Q}_{ni} - \boldsymbol{S}^{\mathrm{q}}_{ni} - \Delta t_n \, a_{ii} \boldsymbol{r}\big(\boldsymbol{U}_{ni}, \hat{\boldsymbol{U}}_{ni}, \boldsymbol{Q}_{ni}\big) \tag{3.48}$$

with $T_{ni} = t_n + c_i \Delta t_n$ , $\Delta t_n = t_{n+1} - t_n$ have to be solved. $c_i$, $i = 1, \ldots, s$, and $a_{ij}$ ($a_{ij} = 0$ for $j < i$), are the coefficients of the Butcher array containing the weighting factors which is dependent on the time integration method, assembled in Appendix A.1 Tab. A.1, see for more details (Hairer et al., 1993; Hairer and Wanner, 1996). The condition $(3.47)_3$ is fulfilled in the final solution and hence the system (3.47) is simplified to

$$\begin{aligned} \boldsymbol{g}\big(T_{ni}, \boldsymbol{U}_{ni}, \boldsymbol{Q}_{ni}\big) &= \boldsymbol{0}, \\ \overline{\boldsymbol{g}}\big(T_{ni}, \boldsymbol{U}_{ni}, \boldsymbol{Q}_{ni}\big) + \boldsymbol{\Lambda}_{ni} &= \boldsymbol{0}, \\ \boldsymbol{I}\big(T_{ni}, \boldsymbol{U}_{ni}, \boldsymbol{Q}_{ni}\big) &= \boldsymbol{0}. \end{aligned} \tag{3.49}$$

The stage derivatives are determined by using the previously determined stage quantities

$$\dot{\boldsymbol{U}}_{ni} = \frac{\boldsymbol{U}_{ni} - \boldsymbol{S}^{\mathrm{u}}_{ni}}{\Delta t_n \, a_{ii}}, \qquad \dot{\boldsymbol{Q}}_{ni} = \frac{\boldsymbol{Q}_{ni} - \boldsymbol{S}^{\mathrm{q}}_{ni}}{\Delta t_n \, a_{ii}}, \qquad \dot{\boldsymbol{\Lambda}}_{ni} = \frac{\boldsymbol{\Lambda}_{ni} - \boldsymbol{S}^{\lambda}_{ni}}{\Delta t_n \, a_{ii}}. \tag{3.50}$$

The stage derivatives are required to determine the starting vectors

$$\begin{aligned}
\boldsymbol{S}_{ni}^{\mathrm{u}} &= \boldsymbol{u}_n + \Delta t_n \sum_{j=1}^{i-1} a_{ij} \dot{\boldsymbol{U}}_{nj}, \\
\boldsymbol{S}_{ni}^{\mathrm{q}} &= \boldsymbol{q}_n + \Delta t_n \sum_{j=1}^{i-1} a_{ij} \dot{\boldsymbol{Q}}_{nj}, \\
\boldsymbol{S}_{ni}^{\lambda} &= \boldsymbol{\Lambda}_n + \Delta t_n \sum_{j=1}^{i-1} a_{ij} \dot{\boldsymbol{\Lambda}}_{nj}.
\end{aligned} \tag{3.51}$$

The nodal displacements $\boldsymbol{U}_{ni}$, the reaction forces $\boldsymbol{\Lambda}_{ni}$ (negative Lagrange multipliers), and all internal variables $\boldsymbol{Q}_{ni}$ from all Gauss-points in the structure are the unknown stage quantities. The final values at time $t_{n+1}$ are given by

$$\begin{aligned}
\boldsymbol{u}_{n+1} &= \boldsymbol{u}_n + \Delta t_n \sum_{i=1}^{s} b_i \dot{\boldsymbol{U}}_{ni}, \\
\boldsymbol{q}_{n+1} &= \boldsymbol{q}_n + \Delta t_n \sum_{i=1}^{s} b_i \dot{\boldsymbol{Q}}_{ni}, \\
\boldsymbol{\lambda}_{n+1} &= \boldsymbol{\lambda}_n + \Delta t_n \sum_{i=1}^{s} b_i \dot{\boldsymbol{\Lambda}}_{ni},
\end{aligned} \tag{3.52}$$

where the $b_i$, $i = 1, \ldots, s$, are some additional weighting factors (coefficients of the Butcher array). In the case of the so-called Stiffly accurate DIRK methods, $a_{ij} = 0$ for $j > i$ and $a_{sj} = b_j$. In Ellsiepen and Hartmann (2001), a detailed analysis of different DIRK-methods are studied.The system of equation $(3.49)_{1,3}$ can be rewritten in the form

$$\begin{aligned}
\boldsymbol{G}_{ni}\big(\boldsymbol{U}_{ni}, \boldsymbol{\Lambda}_{ni}, \boldsymbol{Q}_{ni}\big) = \boldsymbol{g}\big(T_{ni}, \boldsymbol{U}_{ni}, \boldsymbol{\Lambda}_{ni}, \boldsymbol{Q}_{ni}\big) = \boldsymbol{0}, \\
\boldsymbol{L}_{ni}\big(\boldsymbol{U}_{ni}, \boldsymbol{Q}_{ni}\big) = \boldsymbol{l}\big(T_{ni}, \boldsymbol{U}_{ni}, \boldsymbol{Q}_{ni}\big) = \boldsymbol{0}.
\end{aligned} \tag{3.53}$$

This is a completely decoupled system of nonlinear equations represented in the form

$$\boldsymbol{R}_{ni}\big(\boldsymbol{U}_{ni}, \boldsymbol{\Lambda}_{ni}, \boldsymbol{Q}_{ni}\big) = \left\{ \begin{array}{c} \boldsymbol{G}_{ni}\big(\boldsymbol{U}_{ni}, \boldsymbol{\Lambda}_{ni}, \boldsymbol{Q}_{ni}\big) \\ \boldsymbol{L}_{ni}\big(\boldsymbol{U}_{ni}, \boldsymbol{Q}_{ni}\big) \end{array} \right\} = \boldsymbol{0} \tag{3.54}$$

and is solved using Multilevel-Newton algorithm for each stages $i$ in the time interval $[t_n, t_{n+1}]$.

## 3.5. Multilevel-Newton Algorithm

Multilevel-Newton algorithm is based on the concept that the decoupled system of nonlinear equations are solved, as the name suggests, at different levels. In finite elements, the system of

equations are solved at two levels, namely global level $\boldsymbol{G}$ (node level) and local level $\boldsymbol{L}$ (Gauss point level). The equilibrium equations are solved at a global level while the internal variables are computed at the local level. For details of mathematical development behind the Multilevel-Newton algorithm, see the original scheme (Rabbat et al., 1979), and for the discussion with regards to finite elements, see (Ellsiepen and Hartmann, 2001; Hartmann, 2005).

The start point of MLNA is the Eq.(3.53). As a first step, the implicit function theorem is applied to Eq.$(3.53)_2$. From hereon, the subscript $ni$ is omitted for brevity. Assuming that $\boldsymbol{L}$ is a sufficiently smooth function, there exists a function $\boldsymbol{Q}(\boldsymbol{U})$ in the vicinity of the solution. This function is substituted for $\boldsymbol{L}$ in the Eq.$(3.53)_1$

$$\boldsymbol{G}(\boldsymbol{U}, \boldsymbol{Q}(\boldsymbol{U})) = \boldsymbol{0} \tag{3.55}$$

which results in a nonlinear system of equations in variable $\boldsymbol{U}$. The classical Newton-Raphson method is applied to the above equation to determine variable $\boldsymbol{U}$ leading to the linear system of equations in every iteration step $m$

$$\left[\frac{\partial \boldsymbol{G}}{\partial \boldsymbol{U}} + \frac{\partial \boldsymbol{G}}{\partial \boldsymbol{Q}} \frac{\mathrm{d}\boldsymbol{Q}}{\mathrm{d}\boldsymbol{U}}\right]^{(m)} \Delta \boldsymbol{U} = -\boldsymbol{G}(\boldsymbol{U}^{(m)}, \boldsymbol{Q}^{(m)}). \tag{3.56}$$

$\Delta \boldsymbol{U} = \boldsymbol{U}^{(m+1)} - \boldsymbol{U}^{(m)}$ describes the increase in the quantity $\boldsymbol{U}$. The differentials $\partial \boldsymbol{G}/\partial \boldsymbol{U}$ and $\partial \boldsymbol{G}/\partial \boldsymbol{Q}$ can be explicitly calculated. The unknown $\mathrm{d}\boldsymbol{Q}/\mathrm{d}\boldsymbol{U}$ is indirectly calculated at the local Gauss-point level. This is obtained by the application of the chain-rule to the function

$$\boldsymbol{L}(\boldsymbol{U}, \boldsymbol{Q}(\boldsymbol{U})) = \boldsymbol{0} \tag{3.57}$$

which results in

$$\frac{\partial \boldsymbol{L}}{\partial \boldsymbol{U}} + \frac{\partial \boldsymbol{L}}{\partial \boldsymbol{Q}} \frac{\mathrm{d}\boldsymbol{Q}}{\mathrm{d}\boldsymbol{U}} = \boldsymbol{0} \quad \rightarrow \quad \left[\frac{\partial \boldsymbol{L}}{\partial \boldsymbol{Q}}\right] \frac{\mathrm{d}\boldsymbol{Q}}{\mathrm{d}\boldsymbol{U}} = -\frac{\partial \boldsymbol{L}}{\partial \boldsymbol{U}}. \tag{3.58}$$

Since the internal variables $\boldsymbol{Q}$ are decoupled from Gauss-point to Gauss-point, they can be determined by applying the classical Newton-Raphson method on the local level.

The Multilevel-Newton algorithm is summarized in Tab. 3.1.

Table 3.1.: Multilevel-Newton algorithm in the $i$-th stage of time-step $t_n \rightsquigarrow t_{n+1}$

**Given:** $\boldsymbol{U}_{ni}^{(0)} = \boldsymbol{U}_{ni}$ , $\boldsymbol{Q}_{ni}^{(0)} = \boldsymbol{Q}_{ni}$, $\Delta t_n$ , $T_{ni}$, $a_{ii}$, $\boldsymbol{S}_{ni}$

**Repeat** $m = 0, \ldots$

*local level* (given: $\boldsymbol{U}_{ni}^{(m)}$, argument vector $\boldsymbol{y} := (T_{ni}, \boldsymbol{U}_{ni}^{(m)}, \boldsymbol{Q}_{ni}^{(m)})$)

local integration step

$$\boldsymbol{L}(\boldsymbol{U}_{ni}^{(m)}, \boldsymbol{Q}_{ni}^{(m)}) = \boldsymbol{0} \qquad \rightsquigarrow \boldsymbol{Q}_{ni}^{(m)} \tag{3.59}$$

consistent linearization

$$\left[\left.\frac{\partial \boldsymbol{L}}{\partial \boldsymbol{Q}}\right|_{\boldsymbol{y}}\right] \left.\frac{\mathrm{d}\boldsymbol{Q}}{\mathrm{d}\boldsymbol{U}}\right|_{\boldsymbol{y}} = -\left.\frac{\partial \boldsymbol{L}}{\partial \boldsymbol{U}}\right|_{\boldsymbol{y}} \qquad \rightsquigarrow \left.\frac{\mathrm{d}\boldsymbol{Q}}{\mathrm{d}\boldsymbol{U}}\right|_{\boldsymbol{y}} \tag{3.60}$$

*global level*

solve linear system of equations

$$\left[\left.\frac{\partial \boldsymbol{G}}{\partial \boldsymbol{U}}\right|_{\boldsymbol{y}} + \left.\frac{\partial \boldsymbol{G}}{\partial \boldsymbol{Q}}\right|_{\boldsymbol{y}} \left.\frac{\mathrm{d}\boldsymbol{Q}}{\mathrm{d}\boldsymbol{U}}\right|_{\boldsymbol{y}}\right] \Delta \boldsymbol{U}_{ni} = -\boldsymbol{G}(\boldsymbol{y}) \qquad \rightsquigarrow \Delta \boldsymbol{U}_{ni} \tag{3.61}$$

Update of global variables

$$\boldsymbol{U}_{ni}^{(m+1)} \leftarrow \boldsymbol{U}_{ni}^{(m)} + \Delta \boldsymbol{U}_{ni} \qquad \rightsquigarrow \boldsymbol{U}_{ni}^{(m+1)} \tag{3.62}$$

**Until** the convergence criterion is fulfilled

# 4. Parameter Identification

The basics in Continuum Mechanics which is used to develop constitutive models were introduced in Chapter 2. These models are characterized using different parameters. In order to predict the response of a material under various loads, it is essential to identify the material parameters accurately. To this extent, experiments are performed to identify these parameters. *Material parameter identification* is the calibration of these experimental data to the constitutive model to obtain the material parameters within a certain range of application, see (Mahnken and Stein, 1996; Kreißig, 1998; Scheday, 2003; Hartmann et al., 2003) and (Hartmann and Gilbert, 2018).

In this chapter, different aspects of material parameter identification are addressed. First and foremost, the methodology is introduced to show how the problem is set up. It is important to be able to quantify the quality of the identified material parameters. Thus, different quality measures of identification procedure are introduced. One of the most important yet hardly discussed aspect is the concept of local identifiability of the material parameters. It can be widely seen that many researchers identify material parameters without making sure that the identified parameters are addressed by the experimental data. However, in this thesis, effort is taken to understand the basics of identifiability with various simple examples. In order to finish the identification procedure, it is essential that the sensitivity (also known as the functional matrix) vanishes at the local minimum. Thus, it is essential to determine these sensitivities of the parameters. It is possible to determine these sensitivities using different methods. These methods are explained in detail to conclude the chapter.

## 4.1. Methodology

The first step of material parameter identification is performing experiments on the material. Once the experiments are performed, the constitutive model is developed or known model is taken which are characterized by different material parameters. For successful material parameter identification, two basic data sets are required namely experiment data as well as the data from the model response, called simulated data. It is assumed that both these data sets are available a priori. Once these data sets are available, the material parameter identification process is performed. Before discussing how a material parameter problem is set up, insights into the nonlinear least-square problem, which forms the basis of material parameter identification, see (Nocedal and Wright, 1999), are required and thereby introduced. The square of the norm of the residuum $\mathbf{r}(\boldsymbol{\kappa})$,

$$\mathbf{r}(\boldsymbol{\kappa}) = \boldsymbol{s}(\boldsymbol{\kappa}) - \boldsymbol{d} \tag{4.1}$$

should be minimized. If the experimental data $\boldsymbol{d} \in \mathbb{R}^{n_\mathrm{d}}$ and the simulated data $\boldsymbol{s} \in \mathbb{R}^{n_\mathrm{d}}$ don't coincide temporally, a linear interpolation has to be applied either to the experimental data or the simulated data. Whether the interpolation is done on the experiment or the simulation data set is done on a case-to-case basis. Here, $\boldsymbol{\kappa} \in \mathbb{R}^{n_\kappa}$ is the set of material parameters that characterize the constitutive model. The $L_2$-norm of the residuum is called the objective function (also referred to as the goal function) and is represented as

$$f(\boldsymbol{\kappa}) = \frac{1}{2}\|\mathbf{r}(\boldsymbol{\kappa})\|^2 = \frac{1}{2}\mathbf{r}^T(\boldsymbol{\kappa})\mathbf{r}(\boldsymbol{\kappa}) = \frac{1}{2}\sum_{i=1}^{n_\mathrm{d}}(s_i(\boldsymbol{\kappa}) - d_i)^2 \quad \rightarrow \quad \min \tag{4.2}$$

under the inequality constraints

$$\kappa_{\min j} \leq \kappa_j \leq \kappa_{\max j}, \quad j = 1, \ldots, n_\kappa, \tag{4.3}$$

This is an ill-posed problem and might lead to multiple solutions. The factor $1/2$ does not change the problem and is chosen to avoid a factor 2 in the calculation of derivatives. Of course, the inequality constraints mean that it is essential to know certain properties of the parameters. For example, for Poisson's ratio it is known that the value lies between $[0, 0.5]$. These values are then defined as $\kappa_{\min}$ and $\kappa_{\max}$ respectively in determining Poisson's ratio. In some cases, if these inequality constraints are not assigned, the identified material parameters can lead to non-physical results. For linear least-square problems due to the linear dependence of the parameters on the simulation, the objective function is reduced to

$$f(\boldsymbol{\kappa}) = \frac{1}{2}\|\boldsymbol{A\kappa} - \boldsymbol{d}\|^2 = \frac{1}{2}\left(\boldsymbol{\kappa}^T\boldsymbol{A}^T\boldsymbol{A\kappa} - 2\boldsymbol{\kappa}^T\boldsymbol{A}^T\boldsymbol{d} + \boldsymbol{d}^T\boldsymbol{d}\right) \quad \rightarrow \quad \min. \tag{4.4}$$

For linear least-square case, the application of Gâteaux-derivative* to Eq.(4.4) leads to

$$\mathsf{D}\, f(\boldsymbol{\kappa})[\boldsymbol{h}] = \boldsymbol{h}^T\boldsymbol{A}^T\{\boldsymbol{A\kappa} - \boldsymbol{d}\} = \boldsymbol{h}^T \underbrace{\left\{\left[\boldsymbol{A}^T\boldsymbol{A}\right]\boldsymbol{\kappa} - \boldsymbol{A}^T\boldsymbol{d}\right\}}_{\mathrm{d}f(\boldsymbol{\kappa})/\mathrm{d}\boldsymbol{\kappa}} \stackrel{!}{=} 0, \tag{4.5}$$

i.e. for any arbitrary directions $\boldsymbol{h}$, the system of linear equations

$$\left[\boldsymbol{A}^T\boldsymbol{A}\right]\boldsymbol{\kappa} = \boldsymbol{A}^T\boldsymbol{d}, \tag{4.6}$$

has to hold, see, for example, (Beck and Arnold, 1977; Lawson and Hanson, 1995).

For NLS-problems, the application of Gâteaux-derivative to Eq.(4.2) yields

$$\mathsf{D}\, f(\boldsymbol{\kappa})[\boldsymbol{h}] = \frac{\mathrm{d}}{\mathrm{d}\lambda} f(\boldsymbol{\kappa} + \lambda\boldsymbol{h})\Big|_{\lambda=0} = \left\{\frac{\mathrm{d}f}{\mathrm{d}\boldsymbol{\kappa}}\right\}^T \boldsymbol{h} = \boldsymbol{h}^T\left[\frac{\mathrm{d}\boldsymbol{s}(\boldsymbol{\kappa})}{\mathrm{d}\boldsymbol{\kappa}}\right]^T \{\boldsymbol{s}(\boldsymbol{\kappa}) - \boldsymbol{d}\} \stackrel{!}{=} 0, \tag{4.7}$$

i.e. for any arbitrary $\boldsymbol{h}$ we have the system of non-linear equations (necessary condition of a local minimum)

$$\left.\frac{\mathrm{d}f(\boldsymbol{\kappa})}{\mathrm{d}\boldsymbol{\kappa}}\right|_{\boldsymbol{\kappa}=\boldsymbol{\kappa}^*} = \boldsymbol{J}^T(\boldsymbol{\kappa}^*)\{\boldsymbol{s}(\boldsymbol{\kappa}^*) - \boldsymbol{d}\} \stackrel{!}{=} \boldsymbol{0}. \tag{4.8}$$

*Gâteaux-derivative is $\mathsf{D}_x\, f(x)[h] = \frac{\mathrm{d}}{\mathrm{d}\lambda} f(x + \lambda h)\Big|_{\lambda=0}$

Here, $\boldsymbol{J}(\boldsymbol{\kappa}) = \boldsymbol{D}(\boldsymbol{\kappa}) := \mathrm{d}\mathbf{r}(\boldsymbol{\kappa})/\mathrm{d}\boldsymbol{\kappa} = \mathrm{d}\boldsymbol{s}(\boldsymbol{\kappa})/\mathrm{d}\boldsymbol{\kappa}$, $\boldsymbol{J} \in \mathbb{R}^{n_\mathrm{d} \times n_\kappa}$ is the Jacobian or also called functional matrix, which must be equal to zero at a local minimum $\boldsymbol{\kappa}^*$.

Generally, different physical quantities like force, displacement etc. are assembled in the residuum vector. Additionally, the number of data points of these quantities may be of different order. It may lead to the NLS-algorithm prioritizing one quantity over the other. To circumvent this problem, weighting matrix $\boldsymbol{W} \in \mathbb{R}^{n_\mathrm{d} \times n_\mathrm{d}}$ (commonly, a diagonal matrix) is introduced, see (Hartmann, 2001a), such that

$$\tilde{\mathbf{r}} = \boldsymbol{W}\mathbf{r} \tag{4.9}$$

Now, the NLS-problem reads

$$f(\boldsymbol{\kappa}) = \frac{1}{2}\{\boldsymbol{W}\mathbf{r}(\boldsymbol{\kappa})\}^T \boldsymbol{W}\mathbf{r}(\boldsymbol{\kappa}) = \frac{1}{2}\{\boldsymbol{W}\{\boldsymbol{s}(\boldsymbol{\kappa}) - \boldsymbol{d}\}\}^T\{\boldsymbol{W}\{\boldsymbol{s}(\boldsymbol{\kappa}) - \boldsymbol{d}\}\} \rightarrow \min \tag{4.10}$$

The necessary condition for the minimum in the solution $\boldsymbol{\kappa} = \boldsymbol{\kappa}^*$ for Eq.(4.10) is given by

$$\boldsymbol{F}(\boldsymbol{\kappa}) = \frac{\mathrm{d}f}{\mathrm{d}\boldsymbol{\kappa}} = \boldsymbol{D}^T(\boldsymbol{\kappa})\boldsymbol{W}^T\boldsymbol{W}\{\boldsymbol{s}(\boldsymbol{\kappa}) - \boldsymbol{d}\} \stackrel{!}{=} \boldsymbol{0}, \quad \rightarrow \quad \boldsymbol{\kappa}^* \tag{4.11}$$

representing a system of non-linear equations to determine the material parameters $\boldsymbol{\kappa}^*$. Here, $\boldsymbol{D}$, the functional matrix reads

$$\boldsymbol{D}(\boldsymbol{\kappa}) = \boldsymbol{J}(\boldsymbol{\kappa}) = \frac{\mathrm{d}\tilde{\mathbf{r}}(\boldsymbol{\kappa})}{\mathrm{d}\boldsymbol{\kappa}} = \frac{\mathrm{d}\boldsymbol{W}\boldsymbol{s}(\boldsymbol{\kappa})}{\mathrm{d}\boldsymbol{\kappa}}, \tag{4.12}$$

$\boldsymbol{D} \in \mathbb{R}^{n_\mathrm{d} \times n_\kappa}$, is required, is often referred to as the *sensitivity matrix* or shortly *sensitivity*. This holds for Gauss-Newton-like algorithms as well, see for example (Schittkowski, 2002; Nocedal and Wright, 1999; Lawson and Hanson, 1995). There are different methods to determine these sensitivities which will be discussed later on in Section 4.4.

Now that the problem is set up, see Eq.(4.2), the next important question is how to solve this nonlinear problem. There are different numerical iterative methods to solve this problem, see (Bazaraa et al., 1993; Dennis and Schnabel, 1996; Björck, 1996; Nocedal and Wright, 1999). In this research work, the trust-region-reflective algorithm is used to solve this problem. For detailed description of the trust-region-reflective algorithm, please refer (Moré and Sorensen, 1983). The algorithm is already implemented in Matlab ® in the subroutine `lsqnonlin.m`. In linear optimization cases, it may happen that a nearly singular matrix $\boldsymbol{J}^T\boldsymbol{J} = \boldsymbol{A}^T\boldsymbol{A}$ may lead to highly sensitive results, see (Hartmann, 2001a) were a hyperelastic case was studied. Such drawbacks can be overcome by performing singular value decomposition techniques, or by regularization techniques, see (Tikhonov et al., 1995).

Since the NLS is an ill-posed problem which might lead to multiple solutions, the quality of the identification needs to be investigated, see (Kreissig et al., 2001; Rauchs et al., 2010; Krämer et al., 2015) and (Hartmann and Gilbert, 2018) where different qualitative measures are introduced. One such entity is the correlation matrix. In the non-linear case, we have two possibilities. One approach is the application of Taylor-expansion of the residual in the neighborhood of the solution $\boldsymbol{\kappa}^*$ (which is the local minimum), see (Björck, 1996),

$$\mathbf{r}(\boldsymbol{\kappa}) = \mathbf{r}(\boldsymbol{\kappa}^*) + \left.\frac{\mathrm{d}\mathbf{r}}{\mathrm{d}\boldsymbol{\kappa}}\right|_{\boldsymbol{\kappa}=\boldsymbol{\kappa}^*} \{\boldsymbol{\kappa} - \boldsymbol{\kappa}^*\} = \mathbf{r}(\boldsymbol{\kappa}^*) + \boldsymbol{J}(\boldsymbol{\kappa}^*)\{\boldsymbol{\kappa} - \boldsymbol{\kappa}^*\}, \tag{4.13}$$

leading to the linear optimization problem

$$f(\boldsymbol{\kappa}) = \frac{1}{2}\|\mathbf{r}(\boldsymbol{\kappa}^*) + \boldsymbol{J}(\boldsymbol{\kappa}^*)\{\boldsymbol{\kappa} - \boldsymbol{\kappa}^*\}\|. \tag{4.14}$$

The alternate approach is to approximate the objective function by a quadratic function at the solution point $\Delta\boldsymbol{\kappa} = \boldsymbol{\kappa} - \boldsymbol{\kappa}^*$

$$\hat{f}(\boldsymbol{\kappa}) = f(\boldsymbol{\kappa}^*) + \left\{\frac{\mathrm{d}f(\boldsymbol{\kappa})}{\mathrm{d}\boldsymbol{\kappa}}\right\}^T\Bigg|_{\boldsymbol{\kappa}=\boldsymbol{\kappa}^*} \Delta\boldsymbol{\kappa} + \frac{1}{2}\Delta\boldsymbol{\kappa}^T\left[\frac{\mathrm{d}^2 f(\boldsymbol{\kappa})}{\mathrm{d}\boldsymbol{\kappa}\mathrm{d}\boldsymbol{\kappa}}\right]\Bigg|_{\boldsymbol{\kappa}=\boldsymbol{\kappa}^*} \Delta\boldsymbol{\kappa}, \tag{4.15}$$

where the Hessian is

$$\boldsymbol{H}(\boldsymbol{\kappa}) = \frac{\mathrm{d}^2 f(\boldsymbol{\kappa})}{\mathrm{d}\boldsymbol{\kappa}\mathrm{d}\boldsymbol{\kappa}} = \left[\frac{\partial^2 f(\boldsymbol{\kappa})}{\partial\kappa_i\partial\kappa_j}\right] = \left[\sum_{k=1}^{n_\mathrm{d}}\left(\frac{\partial^2 s_k(\boldsymbol{\kappa})}{\partial\kappa_i\partial\kappa_j}(s_k(\boldsymbol{\kappa}) - d_k) + \frac{\partial s_k(\boldsymbol{\kappa})}{\partial\kappa_i}\frac{\partial s_k(\boldsymbol{\kappa})}{\partial\kappa_j}\right)\right]. \tag{4.16}$$

$\mathrm{d}f(\boldsymbol{\kappa})/\mathrm{d}\boldsymbol{\kappa}$ is the Jacobian and has to vanish in the local minimum $\boldsymbol{\kappa}^*$, see Eq.(4.8).

## 4.2. Measures of Optimization Quality

The NLS problem, as set up in Eq.(4.2) is an ill-posed problem and consequently, does not ensure that a unique solutions always exists. Obviously, the quality of the identified results can then be questioned. To address this issue, certain indicators are introduced to get a better understanding of the final results. They are namely the confidence interval, correlation between the identified material parameters and the coefficient of determination, see (Krämer et al., 2015) and (Hartmann and Gilbert, 2018) in the context of material parameter identification.

**Confidence Interval** The quantity confidence interval is used to identify the plausible range of values for the parameter of interest. The confidence interval is approximated by linearizing the non-linear model at the optimized parameter $\boldsymbol{\kappa}^*$, see (Krämer et al., 2015) and (Hartmann and Gilbert, 2018), leading to

$$\mathbf{r}(\boldsymbol{\kappa}) = \mathbf{r}(\boldsymbol{\kappa}^*) + \boldsymbol{J}(\boldsymbol{\kappa}^*)(\boldsymbol{\kappa} - \boldsymbol{\kappa}^*). \tag{4.17}$$

The covariance matrix is symmetric and is approximated by

$$\mathbf{P} \approx s^2\left[\boldsymbol{J}^T(\boldsymbol{\kappa}^*)\boldsymbol{J}(\boldsymbol{\kappa}^*)\right]^{-1} \tag{4.18}$$

where $s$ is the standard deviation and $s^2$ denotes the variance defined by

$$s^2 = \frac{1}{n_\mathrm{d} - 1}\sum_{i=1}^{n_\mathrm{d}}(r_i - \overline{r})^2, \tag{4.19}$$

with the mean-value $\overline{r} = (\sum_{i=1}^{n_\mathrm{d}} r_i)/n_\mathrm{d}$. Variances are the diagonal entries of the covariance matrix and non-diagonal entries are the covariances. Due to this fact, the covariance matrix is

also called the variance-covariance matrix. Covariance is a measure of dependence of material parameters on each other. It characterizes how a change in one parameter affects the other material parameter. In other words, it quantifies linear dependence of parameters. It gives an idea about the response of the constitutive model to changes in two parameters. When two parameters vary directly it implies a positive covariance, while the inverse proportionality of two parameters signifies a negative covariance. The covariance matrix reads

$$\mathbf{P} = \begin{bmatrix} s^2_{\kappa_1} & \text{cov}(\kappa_1, \kappa_2) & \dots & \text{cov}(\kappa_1, \kappa_{n_\kappa}) \\ & s^2_{\kappa_2} & \dots & \text{cov}(\kappa_2, \kappa_{n_\kappa}) \\ & & \ddots & \vdots \\ \text{sym} & & & s^2_{\kappa_{n_\kappa}} \end{bmatrix}.$$

The range of the confidence interval is determined by taking the square root of the variances of the covariance matrix. Therefore, the confidence interval of the parameter $\kappa_i$ is

$$\kappa_i^{\text{conf}} = \kappa_i^* \pm \Delta\kappa_i^* \in \mathbb{R}^{n_\kappa} \quad \text{with} \quad \Delta\kappa_i^* = \sqrt{s^2_{\kappa_i}} \in \mathbb{R}^{n_\kappa}, i = 1, \dots, n_\kappa. \tag{4.20}$$

**Correlation Coefficient** The information regarding the correlation between two material parameters $\kappa_i$ and $\kappa_j$ is enclosed within the covariance matrix $\mathbf{P}$. The correlation coefficient represents the nonorthogonality between two parameters. The correlation between parameters is assembled in the correlation matrix $\boldsymbol{C}$ and is calculated from the covariance matrix by

$$C_{ij} = \frac{P_{ij}}{\sqrt{P_{ii}P_{jj}}} =: \text{corr}(\kappa_i, \kappa_j). \tag{4.21}$$

It is clear that $c_{ii} = 1$ and the non-diagonal elements $c_{ij}$ represent the degree to which the two material parameters are linearly correlated and they lie within the interval $[-1, 1]$. The correlation matrix reads

$$\mathbf{C} = \begin{bmatrix} 1 & \text{corr}(\kappa_1, \kappa_2) & \dots & \text{corr}(\kappa_1, \kappa_m) \\ & 1 & & \text{corr}(\kappa_2, \kappa_m) \\ & & \ddots & \\ \text{sym} & & & 1 \end{bmatrix}.$$

If $C_{ij} = \pm 1$, $i \neq j$, this indicates that the parameter $\kappa_i$ and $\kappa_j$ completely depend on each other. Direct dependency is represented by a positive correlation. Furthermore, a negative correlation indicates inverse proportionality among the two parameters. When the parameters are strongly correlated, the uncertainty in the parameter identification may also be high, see (Šimůnek and Hopmans, 2002). This quantity may be taken as a measure to determine non-adjustable parameters when the parameters are strongly correlated to each other. A strong correlation can be seen for $\mid c_{ij} \mid > 0.8$. However, the acceptable thresholds for this measure is mostly defined based on experience of the user.

**Coefficient of Determination** The coefficient of determination is the measure of how well a model explains and predicts future outcomes. The coefficient is also known as $R$-squared (or $R^2$) and is used as a guideline to measure the accuracy of the model. $R^2$ is defined by

$$R^2 = 1 - \frac{\sum_{i=1}^{n_\mathrm{d}} (d_i - s_i)^2}{\sum_{i=1}^{n_\mathrm{d}} (d_i - \bar{d})^2} \quad \text{with} \quad \bar{d} = \frac{1}{n_\mathrm{d}} \sum_{i=1}^{n_\mathrm{d}} d_i, \tag{4.22}$$

see, for example, (Draper and Smith, 1998). The coefficient $R^2$ is expressed as a value between the interval $[0, 1]$. The value of one indicates a perfect fit, which is extremely rare since there will be almost always some noise in the experimental data. If the value is close to zero, it indicates that the constitutive model fails to reproduce the experimental data. However, this value alone will not give an appropriate quality of the fit even if the value of $R^2$ may be in the vicinity of one, see (Anscombe, 1973).

To conclude, the indicators $\boldsymbol{\kappa}^{\mathrm{conf}}$ of Eq.(4.20), $C_{ij}$ of Eq.(4.21), and $R^2$ of Eq.(4.22) are chosen as quality measures of the material parameter identification process.

## 4.3. Local Identifiability

The ill-posedness of the NLS problem Eq.(4.2) raises the question of uniqueness of the solution. Is it possible to uniquely identify material parameters? Is there a measure that quantifies the uniqueness of the identified parameters? These questions are addressed in (Beck and Arnold, 1977; Beveridge and Schechter, 1970) and the answers to these questions is known as the concept of local identifiability. Identifiability problem can be defined as the necessary conditions under which there exists a unique local minimum for a particular set of material parameters. In certain cases, it is essential to identify parameters separately rather than simultaneously. According to Beck and Arnold (1977), if the sensitivities are linearly dependent within the range of measurements, the parameters cannot be simultaneously and uniquely determined (local minimum). The Hessian Eq.(4.16) can be generally approximated by

$$\boldsymbol{H} \approx \boldsymbol{J}^T \boldsymbol{J} = \left[ \frac{\partial s_k(\boldsymbol{\kappa})}{\partial \kappa_i} \frac{\partial s_k(\boldsymbol{\kappa})}{\partial \kappa_j} \right] \tag{4.23}$$

for small terms $\partial^2 s_k / \partial \kappa_i \partial \kappa_j (s_k - d_k)$ (in comparison to $\boldsymbol{J}^T \boldsymbol{J}$), or in linear least-square problems by $\boldsymbol{H} = \boldsymbol{A}^T \boldsymbol{A}$.

In order to fulfil the necessary condition (4.8) and for non-vanishing and positive definite subdeterminants of the Hessian, $D_r$,

$$D_r = \begin{vmatrix} H_{11} & H_{12} & \dots & H_{1r} \\ H_{21} & H_{22} & \dots & H_{2r} \\ \vdots & & & \vdots \\ H_{r1} & H_{r2} & \dots & H_{rr} \end{vmatrix}, \tag{4.24}$$

i.e. for $r = 1, \ldots, n_\kappa$, for an unique local minimum to exist the following condition has to be satisfied,

$$D_r > 0. \tag{4.25}$$

In some cases, there might exist a minimum, but it is not unique (examples of such cases are shown in Section 5.1)

$$\det \boldsymbol{H}(\boldsymbol{\kappa}^*) = 0. \tag{4.26}$$

According to Beck and Arnold (1977), when using weighted residuals, the determinant of the Hessian may not always be zero. In those cases a new quantity is introduced,

$$\xi_p = \frac{\det \boldsymbol{H}}{(n_\kappa{}^{-1}\mathrm{tr}\,(\boldsymbol{H}))^{n_\kappa}}. \tag{4.27}$$

If $\xi_p > 0$, there exists a unique local minimum and if the value vanishes, this means that a local minimum doesn't exist. Thus, in cases where weighted residuals are used, it is advised to calculate $\xi_p$ to determine identifiability of material parameters.

## 4.4. Determination of Sensitivities

Another important aspect of the identifiability problem is the determination of functional matrix. In this section, different methods to determine the functional matrix $\boldsymbol{D}$ or Jacobian $\boldsymbol{J}$, see Eq.(4.12), also known as *sensitivity matrix* or shortly *sensitivity* are detailed. Here, only a basic idea is given. For more comprehensive discussion, refer (Schittkowski, 2002; Nocedal and Wright, 1999; Lawson and Hanson, 1995; Hartmann, 2017). In the identification of material parameters, determination of sensitivities is an essential and computationally costly procedure. Different methods are available to determine the sensitivity matrix. The three main approaches discussed in this section are *simultaneous sensitivity equations (SSE)*, *external numerical differentiation (END)* and *internal numerical differentiation (IND)*. The classical and most widely used method for determining these sensitivities is END. The parameters to be identified are altered by a small value and the function is again evaluated. However, if the algorithm requires the sensitivities to be accurate, END is not sufficient enough. In such cases, IND and SSE methods can be used to obtain the sensitivities. SSE needs more evaluations of the RHS thus is not computationally efficient. Thus, IND provides a great alternative, see (Bock, 1981, 1983; Bettendorf, 2019) for a more detailed explanation on the topic. In this section, these three methods are discussed within the context of the finite element method using constitutive equations of evolutionary-type.

### 4.4.1. Simultaneous Sensitivity Equations

In order to determine the sensitivities, the starting point is the DAE-system explained in Chapter 3, see Eq.(3.39),

$$\boldsymbol{F}(t, \boldsymbol{y}(t), \dot{\boldsymbol{y}}(t)) \equiv \left\{ \begin{array}{c} \boldsymbol{g}(t, \boldsymbol{u}(t), \boldsymbol{q}(t)) \\ \dot{\boldsymbol{q}}(t) - \boldsymbol{r}(t, \boldsymbol{u}(t), \boldsymbol{q}(t)) \end{array} \right\} = \boldsymbol{0}. \tag{4.28}$$

The DAE-system is differentiated with respect to the parameters $\boldsymbol{\kappa}$ resulting in a matrix DAE-system

$$\begin{aligned} \boldsymbol{0} &= \frac{\partial \boldsymbol{g}}{\partial \boldsymbol{u}}\frac{\partial \boldsymbol{u}}{\partial \boldsymbol{\kappa}} + \frac{\partial \boldsymbol{g}}{\partial \boldsymbol{q}}\frac{\partial \boldsymbol{q}}{\partial \boldsymbol{\kappa}} + \frac{\partial \boldsymbol{g}}{\partial \boldsymbol{\kappa}}, \\ \frac{\partial \dot{\boldsymbol{q}}}{\partial \boldsymbol{\kappa}} &= \frac{\partial \boldsymbol{r}}{\partial \boldsymbol{u}}\frac{\partial \boldsymbol{u}}{\partial \boldsymbol{\kappa}} + \frac{\partial \boldsymbol{r}}{\partial \boldsymbol{q}}\frac{\partial \boldsymbol{q}}{\partial \boldsymbol{\kappa}} + \frac{\partial \boldsymbol{r}}{\partial \boldsymbol{\kappa}}. \end{aligned} \tag{4.29}$$

Here, $\partial \boldsymbol{u}/\partial \boldsymbol{\kappa} \in \mathbb{R}^{n_\mathrm{u} \times n_\kappa}$ and $\partial \boldsymbol{q}/\partial \boldsymbol{\kappa} \in \mathbb{R}^{n_\mathrm{Q} \times n_\kappa}$ are the sensitivities that have to be determined.

The initial conditions of the nodal displacements are independent of the parameters leading to the initial sensitivities with respect to $\boldsymbol{u}$ being $\boldsymbol{0}$ as well, $\partial \boldsymbol{u}(0)/\partial \boldsymbol{\kappa} = \boldsymbol{0}$. The initial sensitivities for the internal variables must be provided as they are commonly dependent on the material parameters, $\partial \boldsymbol{q}(0)/\partial \boldsymbol{\kappa} = \partial \boldsymbol{q}_0/\partial \boldsymbol{\kappa}$. The total number of equations combining Eq.(4.28) and Eq.(4.29) that requires solving is $n_\mathrm{u} + n_\mathrm{Q} + (n_\mathrm{u} + n_\mathrm{Q}) \times n_\kappa = (n_\mathrm{u} + n_\mathrm{Q})(1 + n_\kappa)$. Depending on the spatial discretization, the size of $\boldsymbol{q}$ might itself be millions in number. Thus, this may lead to an extremely inefficient, computationally expensive methods. The DAE-systems are then discretized in the temporal domain.

In classical finite element approach, a Backward-Euler time-integration method is applied to the equations Eq.(4.28) and Eq.(4.29) leading to

$$\begin{aligned} \boldsymbol{g}(t_{n+1}, \boldsymbol{u}_{n+1}, \boldsymbol{q}_{n+1}) &= \boldsymbol{0}, \\ \boldsymbol{I}(t_{n+1}, \boldsymbol{u}_{n+1}, \boldsymbol{q}_{n+1}) &= \boldsymbol{0}, \\ \frac{\partial \boldsymbol{g}}{\partial \boldsymbol{u}_{n+1}}\frac{\partial \boldsymbol{u}_{n+1}}{\partial \boldsymbol{\kappa}} + \frac{\partial \boldsymbol{g}}{\partial \boldsymbol{q}_{n+1}}\frac{\partial \boldsymbol{q}_{n+1}}{\partial \boldsymbol{\kappa}} + \frac{\partial \boldsymbol{g}}{\partial \boldsymbol{\kappa}} &= \boldsymbol{0}, \\ \frac{\partial \boldsymbol{q}_{n+1}}{\partial \boldsymbol{\kappa}} - \frac{\partial \boldsymbol{q}_n}{\partial \boldsymbol{\kappa}} - \Delta t_n \left( \frac{\partial \boldsymbol{r}}{\partial \boldsymbol{u}_{n+1}}\frac{\partial \boldsymbol{u}_{n+1}}{\partial \boldsymbol{\kappa}} + \frac{\partial \boldsymbol{r}}{\partial \boldsymbol{q}_{n+1}}\frac{\partial \boldsymbol{q}_{n+1}}{\partial \boldsymbol{\kappa}} + \frac{\partial \boldsymbol{r}}{\partial \boldsymbol{\kappa}} \right) &= \boldsymbol{0}. \end{aligned} \tag{4.30}$$

It must be noted that

$$\frac{\partial \dot{\boldsymbol{q}}}{\partial \boldsymbol{\kappa}} = \frac{\partial}{\partial \boldsymbol{\kappa}}\frac{\mathrm{d}\boldsymbol{q}}{\mathrm{d}t} = \frac{\mathrm{d}}{\mathrm{d}t}\frac{\partial \boldsymbol{q}}{\partial \boldsymbol{\kappa}}. \tag{4.31}$$

Here, Eq.$(4.30)_2$ is abbreviated by

$$\boldsymbol{I}(t_{n+1}, \boldsymbol{u}_{n+1}, \boldsymbol{q}_{n+1}) = \boldsymbol{q}_{n+1} - \boldsymbol{q}_n - \Delta t_n \, \boldsymbol{r}(t_{n+1}, \boldsymbol{u}_{n+1}, \boldsymbol{q}_{n+1}). \tag{4.32}$$

The non-linear equation systems, $(4.30)_{1,2}$, are decoupled from $(4.30)_{3,4}$. Thus, different specific procedures can be applied to each sets of equations. The general solution procedure entails solving Eqns.$(4.30)_{1,2}$ first and then substitution in Eqns.$(4.30)_{3,4}$ and finally solving. The Multilevel-Newton algorithm detailed in Chapter 3, see summary in Tab. 3.1, is applied to solve the system of equations, (4.30), simultaneously.

### 4.4.2. External Numerical Differentiation

Mostly, researchers use the most simple yet time consuming method of applying external numerical differentiation using finite difference scheme, in particular a forward difference scheme. In

this simple method, the sensitivities (4.12) are approximated by

$$\frac{\mathrm{d}\tilde{\boldsymbol{u}}_{n+1}}{\mathrm{d}\boldsymbol{\kappa}} \approx \sum_{j=1}^{n_\kappa} \frac{\tilde{\boldsymbol{u}}(\boldsymbol{\kappa} + \Delta\kappa_j \overline{\boldsymbol{e}}_j) - \tilde{\boldsymbol{u}}(\boldsymbol{\kappa})}{\Delta\kappa_j} \overline{\boldsymbol{e}}_j^T, \tag{4.33}$$

$$\frac{\mathrm{d}\boldsymbol{\lambda}_{n+1}}{\mathrm{d}\boldsymbol{\kappa}} \approx \sum_{j=1}^{n_\kappa} \frac{\boldsymbol{\lambda}(\boldsymbol{\kappa} + \Delta\kappa_j \overline{\boldsymbol{e}}_j) - \boldsymbol{\lambda}(\boldsymbol{\kappa})}{\Delta\kappa_j} \overline{\boldsymbol{e}}_j^T. \tag{4.34}$$

The vectors $\tilde{\boldsymbol{u}}(\boldsymbol{\kappa})$ and $\boldsymbol{\lambda}(\boldsymbol{\kappa})$ are determined by solving the DAE-system $(4.30)_{1,2}$ using MLNA scheme. Here, the results $\tilde{\boldsymbol{u}}_{n+1}$, $n = 0, \ldots, N-1$, must be calculated and stored with best possible accuracy since it is required to calculate the sensitivities. Besides, the entire finite element program has to be run $n_\kappa + 1$-times with slightly perturbed material parameters $\boldsymbol{\kappa} + \Delta\kappa_j \overline{\boldsymbol{e}}_j$, $j = 1, \ldots, n_\kappa$ in order to determine the sensitivities. The resulting vectors of the required nodal displacements $\tilde{\boldsymbol{u}}_{n+1}(\boldsymbol{\kappa} + \Delta\kappa_j \overline{\boldsymbol{e}}_j)$ have to be stored as well. Thus, it is computationally expensive to determine sensitivities, when the number of material parameters as well as the number of experiments to identify are high.

## 4.4.3. Internal Numerical Differentiation

*Internal Numerical Differentiation* is the fastest method of the three approaches discussed here. The detailed explanation in this section will show the reason for this. Internal numerical differentiation is applied with one important assumption. The entire time integration step is assumed to be dependent on the parameters $\boldsymbol{\kappa}$, see (Bock, 1983; Schittkowski, 2002). This is valid for the stage quantities, the stage derivatives as well as the starting values for Runge-Kutta-type methods described in Section 3.4. Application of the Backward-Euler scheme on Eq.(4.28) results in

$$\begin{aligned} \boldsymbol{g}(t_{n+1}, \boldsymbol{u}_{n+1}(\boldsymbol{\kappa}), \boldsymbol{q}_{n+1}(\boldsymbol{\kappa}), \boldsymbol{\kappa}) &= \boldsymbol{0}, \\ \tilde{\boldsymbol{l}}(t_{n+1}, \boldsymbol{u}_{n+1}(\boldsymbol{\kappa}), \boldsymbol{q}_{n+1}(\boldsymbol{\kappa}), \boldsymbol{q}_n(\boldsymbol{\kappa}), \boldsymbol{\kappa}) &= \boldsymbol{0}, \end{aligned} \tag{4.35}$$

see Eq.(4.32),

$$\tilde{\boldsymbol{l}}\big(t_{n+1}, \boldsymbol{u}_{n+1}(\boldsymbol{\kappa}), \boldsymbol{q}_{n+1}(\boldsymbol{\kappa}), \boldsymbol{q}_n(\boldsymbol{\kappa}), \boldsymbol{\kappa}\big) = \boldsymbol{q}_{n+1}(\boldsymbol{\kappa}) - \boldsymbol{q}_n(\boldsymbol{\kappa}) - \Delta t_n \, \boldsymbol{r}\big(t_{n+1}, \boldsymbol{u}_{n+1}(\boldsymbol{\kappa}), \boldsymbol{q}_{n+1}(\boldsymbol{\kappa}), \boldsymbol{\kappa}\big). \tag{4.36}$$

There are two solution paths that can be adopted from this point, see (Schittkowski, 2002; Hartmann, 2017). One method is to apply the MLNA and the other is to apply chain rule to the system of equations (4.35). Both the methods are detailed below.

### 4.4.3.1. Sensitivities based on Multi-Level Newton Algorithm

The first method is similar to the works by Andresen et al. (1996); Mahnken and Stein (1996, 1997). This is based on the implicit function theorem, where it is assumed that a function $\hat{\boldsymbol{q}}(\boldsymbol{u}_{n+1}(\boldsymbol{\kappa}), \boldsymbol{\kappa})$ exists. This is inserted into the equilibrium equations $(4.35)_1$,

$$\boldsymbol{g}(\boldsymbol{u}_{n+1}(\boldsymbol{\kappa}), \hat{\boldsymbol{q}}(\boldsymbol{u}_{n+1}(\boldsymbol{\kappa}), \boldsymbol{\kappa}), \boldsymbol{\kappa}) = \boldsymbol{0}, \tag{4.37}$$

see also (Krämer, 2016). Eq.(4.37) is derived with respect to the parameters $\boldsymbol{\kappa}$ leading to the linear system (after certain rearrangements)

$$\left[\frac{\partial \boldsymbol{g}}{\partial \boldsymbol{u}_{n+1}} + \frac{\partial \boldsymbol{g}}{\partial \boldsymbol{q}_{n+1}}\frac{\partial \hat{\boldsymbol{q}}}{\partial \boldsymbol{u}_{n+1}}\right]\frac{\partial \boldsymbol{u}_{n+1}}{\partial \boldsymbol{\kappa}} = -\frac{\partial \boldsymbol{g}}{\partial \boldsymbol{\kappa}} - \frac{\partial \boldsymbol{g}}{\partial \boldsymbol{q}_{n+1}}\frac{\partial \hat{\boldsymbol{q}}}{\partial \boldsymbol{\kappa}}. \tag{4.38}$$

Here, the coefficient matrix on the left-hand side of Eq.(4.38) is the same as that in the MLNA (global system), see Tab. 3.1, it is the same as the tangential stiffness matrix. If, in the MLNA, the convergence criteria $\boldsymbol{I} = \boldsymbol{0}$ and $\boldsymbol{g} = \boldsymbol{0}$ are satisfied, then the determined tangential stiffness matrix can be used in Eq.(4.38) to solve the system of equations with multiple right-hand sides without further calculation of the tangential stiffness matrix again. This definitely saves time. In case of finite element simulations that make use of direct solver (LU-decomposition), this is essentially only back-substitution. As explained in the Chapter 3, only a formal assembly of internal variables are carried out leading to decoupling between Gauss-point to Gauss-point. This means that the quantity $\partial\hat{\mathbf{q}}/\partial\boldsymbol{\kappa}$ is determined on "local level" (Gauss-point level) of the MLNA scheme. The function $\hat{\boldsymbol{q}}(\boldsymbol{u}_{n+1}(\boldsymbol{\kappa}), \boldsymbol{\kappa})$ is inserted into the integration step of the internal variables $(4.30)_2$ yielding the equation

$$\tilde{\boldsymbol{I}}(\boldsymbol{u}_{n+1}(\boldsymbol{\kappa}), \hat{\boldsymbol{q}}(\boldsymbol{u}_{n+1}(\boldsymbol{\kappa}), \boldsymbol{\kappa}), \boldsymbol{q}_n(\boldsymbol{\kappa}), \boldsymbol{\kappa}) = \boldsymbol{0}. \tag{4.39}$$

The derivative of the equation with respect to the parameters $\boldsymbol{\kappa}$ results in

$$\frac{\partial \tilde{\boldsymbol{I}}}{\partial \boldsymbol{u}_{n+1}}\frac{\partial \boldsymbol{u}_{n+1}}{\partial \boldsymbol{\kappa}} + \frac{\partial \tilde{\boldsymbol{I}}}{\partial \boldsymbol{q}_{n+1}}\frac{\partial \hat{\boldsymbol{q}}}{\partial \boldsymbol{u}}\frac{\partial \boldsymbol{u}_{n+1}}{\partial \boldsymbol{\kappa}} + \frac{\partial \tilde{\boldsymbol{I}}}{\partial \boldsymbol{q}_{n+1}}\frac{\partial \boldsymbol{q}_{n+1}}{\partial \boldsymbol{\kappa}} + \frac{\partial \tilde{\boldsymbol{I}}}{\partial \boldsymbol{q}_n}\frac{\mathrm{d}\mathbf{q}_n}{\mathrm{d}\boldsymbol{\kappa}} + \frac{\partial \tilde{\boldsymbol{I}}}{\partial \boldsymbol{\kappa}} = \boldsymbol{0}, \tag{4.40}$$

where

$$\frac{\partial \tilde{\boldsymbol{I}}}{\partial \boldsymbol{q}_n} = -\boldsymbol{1}.$$

Eq.(4.40) can be rewritten as

$$\left[\frac{\partial \tilde{\boldsymbol{I}}}{\partial \boldsymbol{u}_{n+1}} + \frac{\partial \tilde{\boldsymbol{I}}}{\partial \boldsymbol{q}_{n+1}}\frac{\partial \hat{\boldsymbol{q}}}{\partial \boldsymbol{u}}\right]\frac{\partial \boldsymbol{u}_{n+1}}{\partial \boldsymbol{\kappa}} + \frac{\partial \tilde{\boldsymbol{I}}}{\partial \boldsymbol{q}_{n+1}}\frac{\partial \boldsymbol{q}_{n+1}}{\partial \boldsymbol{\kappa}} - \frac{\mathrm{d}\mathbf{q}_n}{\mathrm{d}\boldsymbol{\kappa}} + \frac{\partial \tilde{\boldsymbol{I}}}{\partial \boldsymbol{\kappa}} = \boldsymbol{0}. \tag{4.41}$$

From the local level of MLNA of Tab. 3.1, it is known that

$$\frac{\partial \tilde{\boldsymbol{I}}}{\partial \boldsymbol{u}_{n+1}} + \frac{\partial \tilde{\boldsymbol{I}}}{\partial \boldsymbol{q}_{n+1}}\frac{\partial \hat{\boldsymbol{q}}}{\partial \boldsymbol{u}} = \boldsymbol{0}. \tag{4.42}$$

Substituting Eq.(4.42) in Eq.(4.41) leads to

$$\frac{\partial \tilde{\mathbf{I}}}{\partial \mathbf{q}_{n+1}}\frac{\partial \boldsymbol{q}_{n+1}}{\partial \boldsymbol{\kappa}} = \frac{\mathrm{d}\mathbf{q}_n}{\mathrm{d}\boldsymbol{\kappa}} - \frac{\partial \tilde{\mathbf{I}}}{\partial \boldsymbol{\kappa}}, \tag{4.43}$$

Eqns.(4.42) and (4.43) are now substituted into the system (4.38) resulting in

$$\left[\frac{\partial \boldsymbol{g}}{\partial \boldsymbol{u}_{n+1}} - \frac{\partial \boldsymbol{g}}{\partial \boldsymbol{q}_{n+1}}\frac{\partial \tilde{\mathbf{I}}}{\partial \mathbf{q}_{n+1}}^{-1}\frac{\partial \tilde{\boldsymbol{I}}}{\partial \boldsymbol{u}_{n+1}}\right]\frac{\partial \boldsymbol{u}_{n+1}}{\partial \boldsymbol{\kappa}} = -\frac{\partial \boldsymbol{g}}{\partial \boldsymbol{\kappa}} + \frac{\partial \boldsymbol{g}}{\partial \boldsymbol{q}_{n+1}}\frac{\partial \tilde{\mathbf{I}}}{\partial \mathbf{q}_{n+1}}^{-1}\left[-\frac{\mathrm{d}\mathbf{q}_n}{\mathrm{d}\boldsymbol{\kappa}} + \frac{\partial \tilde{\mathbf{I}}}{\partial \boldsymbol{\kappa}}\right]. \tag{4.44}$$

Here, the matrix $\partial\tilde{\boldsymbol{I}}/\partial\boldsymbol{q}_{n+1}$ is already calculated from the previous iteration (local level in MLNA). At the Gauss-point level, small linear systems with $n_\kappa$ right-hand sides with a dimension $n_\mathrm{q}$ have to be solved,

$$\frac{\partial\tilde{\mathbf{I}}}{\partial\mathbf{q}_{n+1}}\frac{\partial\hat{\mathbf{q}}}{\partial\boldsymbol{\kappa}} = \frac{\mathrm{d}\mathbf{q}_n}{\mathrm{d}\boldsymbol{\kappa}} - \frac{\partial\tilde{\mathbf{I}}}{\partial\boldsymbol{\kappa}} \tag{4.45}$$

where $\tilde{\mathbf{I}} \in \mathbb{R}^{n_\mathrm{q}}$ and $\mathbf{q}_n \in \mathbb{R}^{n_\mathrm{q}}$ evaluated at time $t_n$, represent the local integration step of the Backward Euler method, in element $e$ at Gauss-point $\boldsymbol{\xi}^{(k)}$.

For a model without any internal variables, like for example hyperelastic models, equation (4.44) reduces to

$$\left[\frac{\partial\boldsymbol{g}}{\partial\boldsymbol{u}_{n+1}}\right]\frac{\partial\boldsymbol{u}_{n+1}}{\partial\boldsymbol{\kappa}} = -\frac{\partial\boldsymbol{g}}{\partial\boldsymbol{\kappa}}. \tag{4.46}$$

It is now clear that computing the sensitivities on Gauss-point level (4.43), $\partial\hat{\boldsymbol{q}}/\partial\boldsymbol{\kappa}$, and solving the linear system with global tangential stiffness matrix (4.38) at the end of the MLNA yields the sensitivities $\partial\boldsymbol{u}/\partial\boldsymbol{\kappa}$, which are required in Eq.(4.12). The sensitivities $\partial\hat{\mathbf{q}}/\partial\boldsymbol{\kappa}$ computed in Eq.(4.45) at time $t_n$ are stored for the next time-step $t_{n+1}$. The sensitivity $\partial\hat{\mathbf{q}}/\partial\boldsymbol{\kappa}$ at time-step $t_n$ becomes the quantity $\mathrm{d}\mathbf{q}_n/\mathrm{d}\boldsymbol{\kappa}$ for the next time-step $t_{n+1}$. This implies that $n_\mathrm{el} \times n_\mathrm{GP} \times n_\mathrm{q} \times n_\kappa$ number of quantities need to be saved. This is a major drawback of this method: huge amount of storage. Another major drawback is the fact that in the case of black-box finite element programs, it is not possible to access the algorithm to perform internal numerical differentiation. *In this context, it is to be pointed out that even though a huge amount of space is required for IND when compared to END, IND is much more faster than END.* That is the biggest advantage of IND, especially when there are a high number of material parameters to be identified.

#### 4.4.3.2. Sensitivities Based on Chain Rule

Another method to perform the internal numerical differentiation is to apply the chain rule to the system of equations (4.35), see (Hartmann, 2017), yielding

$$\begin{aligned}
\frac{\partial\boldsymbol{g}}{\partial\boldsymbol{u}_{n+1}}\frac{\partial\boldsymbol{u}_{n+1}}{\partial\boldsymbol{\kappa}} + \frac{\partial\boldsymbol{g}}{\partial\boldsymbol{q}_{n+1}}\frac{\partial\boldsymbol{q}_{n+1}}{\partial\boldsymbol{\kappa}} + \frac{\partial\boldsymbol{g}}{\partial\boldsymbol{\kappa}} &= \boldsymbol{0} \\
\frac{\partial\tilde{\boldsymbol{I}}}{\partial\boldsymbol{u}_{n+1}}\frac{\partial\boldsymbol{u}_{n+1}}{\partial\boldsymbol{\kappa}} + \frac{\partial\tilde{\mathbf{I}}}{\partial\mathbf{q}_{n+1}}\frac{\partial\boldsymbol{q}_{n+1}}{\partial\boldsymbol{\kappa}} + \frac{\partial\tilde{\boldsymbol{I}}}{\partial\boldsymbol{q}_n}\frac{\mathrm{d}\mathbf{q}_n}{\mathrm{d}\boldsymbol{\kappa}} + \frac{\partial\tilde{\mathbf{I}}}{\partial\boldsymbol{\kappa}} &= \boldsymbol{0}.
\end{aligned} \tag{4.47}$$

If the sensitivities $\dfrac{\partial\boldsymbol{q}_{n+1}}{\partial\boldsymbol{\kappa}}$ with respect to the internal variables from Eq.$(4.47)_2$ is brought to the left-hand side of the equation

$$\frac{\partial\boldsymbol{q}_{n+1}}{\partial\boldsymbol{\kappa}} = -\left[\frac{\partial\tilde{\mathbf{I}}}{\partial\mathbf{q}_{n+1}}\right]^{-1}\left[\frac{\partial\tilde{\boldsymbol{I}}}{\partial\boldsymbol{u}_{n+1}}\frac{\partial\boldsymbol{u}_{n+1}}{\partial\boldsymbol{\kappa}} - \frac{\partial\tilde{\boldsymbol{I}}}{\partial\boldsymbol{q}_n}\frac{\mathrm{d}\mathbf{q}_n}{\mathrm{d}\boldsymbol{\kappa}} + \frac{\partial\tilde{\boldsymbol{I}}}{\partial\boldsymbol{\kappa}}\right], \tag{4.48}$$

is obtained. The Eq. (4.48) is then inserted into the Eq.$(4.47)_1$, to obtain the the linear system of equations

$$\left[\frac{\partial \boldsymbol{g}}{\partial \boldsymbol{u}_{n+1}} - \frac{\partial \boldsymbol{g}}{\partial \boldsymbol{q}_{n+1}}\left[\frac{\partial \tilde{\mathbf{l}}}{\partial \mathbf{q}_{n+1}}\right]^{-1}\frac{\partial \tilde{\boldsymbol{l}}}{\partial \boldsymbol{u}_{n+1}}\right]\frac{\partial \boldsymbol{u}_{n+1}}{\partial \boldsymbol{\kappa}} = -\frac{\partial \boldsymbol{g}}{\partial \boldsymbol{\kappa}} + \frac{\partial \boldsymbol{g}}{\partial \boldsymbol{q}_{n+1}}\left[\frac{\partial \tilde{\mathbf{l}}}{\partial \mathbf{q}_{n+1}}\right]^{-1}\left[-\frac{\mathrm{d}\mathbf{q}_n}{\mathrm{d}\boldsymbol{\kappa}} + \frac{\partial \tilde{\mathbf{l}}}{\partial \boldsymbol{\kappa}}\right]. \tag{4.49}$$

Thus, the sensitivities $\partial \boldsymbol{u}/\partial \boldsymbol{\kappa} \in \mathbb{R}^{n_{\mathrm{u}} \times n_\kappa}$ and $\partial \boldsymbol{q}/\partial \boldsymbol{\kappa} \in \mathbb{R}^{n_{\mathrm{Q}} \times n_\kappa}$ can be determined by solving this linear system of equations.

### 4.4.4. Sensitivities of Reaction Force

The basics of the reaction force computation by the application of Lagrange multiplier method has been detailed in Section 3.3, see Eq.(3.41) (recapped here),

$$\boldsymbol{F}(t, \boldsymbol{y}(t), \dot{\boldsymbol{y}}(t)) \equiv \left\{\begin{array}{c} \boldsymbol{g}_{\mathrm{a}}(t, \boldsymbol{u}_{\mathrm{a}}(t), \boldsymbol{q}(t)) + \boldsymbol{M}\boldsymbol{\lambda}(t) \\ \boldsymbol{C}_c(t, \boldsymbol{u}_{\mathrm{a}}(t)) \\ \dot{\boldsymbol{q}}(t) - \boldsymbol{r}(\boldsymbol{u}_{\mathrm{a}}(t), \boldsymbol{q}(t)) \end{array}\right\} = \boldsymbol{0} \tag{4.50}$$

where $\boldsymbol{y}^T(t) = \{\boldsymbol{u}_{\mathrm{a}}^T(t), \boldsymbol{\lambda}^T(t), \boldsymbol{q}^T(t)\}$ with the following initial conditions,

$$\boldsymbol{y}(t_0) \equiv \left\{\begin{array}{c} \boldsymbol{u}_{\mathrm{a}}(t_0) \\ \boldsymbol{\lambda}(t_0) \\ \boldsymbol{q}(t_0) \end{array}\right\} = \left\{\begin{array}{c} \boldsymbol{u}_{\mathrm{a}0} \\ \boldsymbol{\lambda}_0 \\ \boldsymbol{q}_0 \end{array}\right\} \equiv \boldsymbol{y}_0. \tag{4.51}$$

For a comprehensive explanation, see (Hartmann, 2017). Now, discretizing this equation in temporal domain using the Backward-Euler method leads to Eq.(3.45) (recapped here)

$$\begin{aligned} \boldsymbol{g}\big(t_{n+1}, \boldsymbol{u}_{n+1}, \boldsymbol{q}_{n+1}\big) &= \boldsymbol{0}, \\ \overline{\boldsymbol{g}}\big(\boldsymbol{u}_{n+1}, \boldsymbol{q}_{n+1}\big) + \boldsymbol{\lambda}_{n+1} &= \boldsymbol{0}, \\ \boldsymbol{l}\big(\boldsymbol{u}_{n+1}, \boldsymbol{q}_{n+1}\big) &= \boldsymbol{0}. \end{aligned} \tag{4.52}$$

The determination of sensitivities $\partial \boldsymbol{u}/\partial \boldsymbol{\kappa} \in \mathbb{R}^{n_{\mathrm{u}} \times n_\kappa}$ and $\partial \boldsymbol{q}/\partial \boldsymbol{\kappa} \in \mathbb{R}^{n_{\mathrm{Q}} \times n_\kappa}$ based on Eqns.$(4.52)_1$ and $(4.52)_3$ has been explained in the Section 4.4.3. Similarly, differentiating Eq.$(4.52)_2$ with respect to $\boldsymbol{\kappa}$ leads to

$$\frac{\mathrm{d}\boldsymbol{\lambda}_{n+1}}{\mathrm{d}\boldsymbol{\kappa}} = -\frac{\partial \overline{\boldsymbol{g}}}{\partial \boldsymbol{u}_{n+1}}\frac{\partial \boldsymbol{u}_{n+1}}{\partial \boldsymbol{\kappa}} - \frac{\partial \overline{\boldsymbol{g}}}{\partial \boldsymbol{q}_{n+1}}\frac{\partial \boldsymbol{q}_{n+1}}{\partial \boldsymbol{\kappa}} - \frac{\partial \overline{\boldsymbol{g}}}{\partial \boldsymbol{\kappa}}. \tag{4.53}$$

Substituting the sensitivity (4.48) in the Eq.(4.53) yields

$$\frac{\mathrm{d}\boldsymbol{\lambda}_{n+1}}{\mathrm{d}\boldsymbol{\kappa}} = -\left[\frac{\partial \overline{\boldsymbol{g}}}{\partial \boldsymbol{u}_{n+1}} - \frac{\partial \overline{\boldsymbol{g}}}{\partial \boldsymbol{q}_{n+1}}\frac{\partial \tilde{\mathbf{l}}^{-1}}{\partial \mathbf{q}_{n+1}}\frac{\partial \tilde{\boldsymbol{l}}}{\partial \boldsymbol{u}_{n+1}}\right]\frac{\partial \boldsymbol{u}_{n+1}}{\partial \boldsymbol{\kappa}} + \frac{\partial \overline{\boldsymbol{g}}}{\partial \boldsymbol{q}_{n+1}}\frac{\partial \tilde{\mathbf{l}}^{-1}}{\partial \mathbf{q}_{n+1}}\left[\frac{\mathrm{d}\mathbf{q}_n}{\mathrm{d}\boldsymbol{\kappa}} - \frac{\partial \tilde{\mathbf{l}}}{\partial \boldsymbol{\kappa}}\right] - \frac{\partial \overline{\boldsymbol{g}}}{\partial \boldsymbol{\kappa}}. \tag{4.54}$$

For a model without any internal variables, like for example hyperelastic models, the Eq.(4.54) reduces to

$$\frac{\mathrm{d}\boldsymbol{\lambda}_{n+1}}{\mathrm{d}\boldsymbol{\kappa}} = -\frac{\partial \overline{\boldsymbol{g}}}{\partial \boldsymbol{u}_{n+1}} \frac{\partial \boldsymbol{u}_{n+1}}{\partial \boldsymbol{\kappa}} - \frac{\partial \overline{\boldsymbol{g}}}{\partial \boldsymbol{\kappa}}. \tag{4.55}$$

From the equation it is clear that only a matrix multiplication is required to determine sensitivities of the reaction forces, as all the other values are readily available from the solution of the MLNA. Thus, this is a computationally effective method.

## 4.5. Extension to DIRK Methods

In this section, the procedure for determination of sensitivities is extended to DIRK methods. The DAE system Eq.(3.41) is discretized in time and the resulting solution Eq.(3.52) is dependent on the parameters $\boldsymbol{\kappa}$,

$$\begin{aligned}
\boldsymbol{u}_{n+1}(\boldsymbol{\kappa}) &= \boldsymbol{u}_n(\boldsymbol{\kappa}) + \Delta t_n \sum_{i=1}^{s} b_i \dot{\boldsymbol{U}}_{ni}(\boldsymbol{\kappa}), \\
\boldsymbol{q}_{n+1}(\boldsymbol{\kappa}) &= \boldsymbol{q}_n(\boldsymbol{\kappa}) + \Delta t_n \sum_{i=1}^{s} b_i \dot{\boldsymbol{Q}}_{ni}(\boldsymbol{\kappa}), \\
\boldsymbol{\lambda}_{n+1}(\boldsymbol{\kappa}) &= \boldsymbol{\lambda}_n(\boldsymbol{\kappa}) + \Delta t_n \sum_{i=1}^{s} b_i \dot{\boldsymbol{\Lambda}}_{ni}(\boldsymbol{\kappa}).
\end{aligned} \tag{4.56}$$

In the case of stiffly accurate DIRK Methods, the final solution at each time $t_{n+1}$ is directly provided by the non-linear system, $\boldsymbol{u}_{n+1}(\boldsymbol{\kappa}) = \boldsymbol{U}_{ns}(\boldsymbol{\kappa})$, $\boldsymbol{q}_{n+1}(\boldsymbol{\kappa}) = \boldsymbol{Q}_{ns}(\boldsymbol{\kappa})$, $\boldsymbol{\lambda}_{n+1}(\boldsymbol{\kappa}) = \boldsymbol{\Lambda}_{ns}(\boldsymbol{\kappa})$. Thus, the derivatives of the stage derivatives and the starting values with respect to $\boldsymbol{\kappa}$,

$$\frac{\mathrm{d}\dot{\boldsymbol{U}}_{ni}}{\mathrm{d}\boldsymbol{\kappa}} = \frac{1}{\Delta t_n\, a_{ii}} \left[ \frac{\mathrm{d}\boldsymbol{U}_{ni}}{\mathrm{d}\boldsymbol{\kappa}} - \frac{\mathrm{d}\boldsymbol{S}^{\mathrm{u}}_{ni}}{\mathrm{d}\boldsymbol{\kappa}} \right], \qquad \frac{\mathrm{d}\dot{\boldsymbol{Q}}_{ni}}{\mathrm{d}\boldsymbol{\kappa}} = \frac{1}{\Delta t_n\, a_{ii}} \left[ \frac{\mathrm{d}\boldsymbol{Q}_{ni}}{\mathrm{d}\boldsymbol{\kappa}} - \frac{\mathrm{d}\boldsymbol{S}^{\mathrm{q}}_{ni}}{\mathrm{d}\boldsymbol{\kappa}} \right], \tag{4.57}$$

are required with

$$\frac{\mathrm{d}\boldsymbol{S}^{\mathrm{u}}_{ni}}{\mathrm{d}\boldsymbol{\kappa}} = \frac{\mathrm{d}\boldsymbol{u}_n}{\mathrm{d}\boldsymbol{\kappa}} + \Delta t_n \sum_{j=1}^{i-1} \frac{\mathrm{d}\dot{\boldsymbol{U}}_{nj}}{\mathrm{d}\boldsymbol{\kappa}}, \qquad \frac{\mathrm{d}\boldsymbol{S}^{\mathrm{q}}_{ni}}{\mathrm{d}\boldsymbol{\kappa}} = \frac{\mathrm{d}\boldsymbol{q}_n}{\mathrm{d}\boldsymbol{\kappa}} + \Delta t_n \sum_{j=1}^{i-1} \frac{\mathrm{d}\dot{\boldsymbol{Q}}_{nj}}{\mathrm{d}\boldsymbol{\kappa}}. \tag{4.58}$$

This implies that the derivatives Eq.(4.57) must be stored additionally and the following dependencies

$$\begin{aligned}
\boldsymbol{g}\big(T_{ni}, \boldsymbol{U}_{ni}(\boldsymbol{\kappa}), \boldsymbol{Q}_{ni}(\boldsymbol{\kappa}), \boldsymbol{\kappa}\big) &= \boldsymbol{0}, \\
\boldsymbol{I}\big(T_{ni}, \boldsymbol{U}_{ni}(\boldsymbol{\kappa}), \boldsymbol{Q}_{ni}(\boldsymbol{\kappa}), \boldsymbol{S}^{\mathrm{q}}_{ni}(\boldsymbol{\kappa}), \boldsymbol{\kappa}\big) &= \boldsymbol{0}, \\
\overline{\boldsymbol{g}}\big(T_{ni}, \boldsymbol{U}_{ni}, \boldsymbol{Q}_{ni}\big) + \boldsymbol{\Lambda}_{ni} &= \boldsymbol{0}
\end{aligned} \tag{4.59}$$

are obtained. The derivatives $\mathrm{d}\boldsymbol{U}/\mathrm{d}\boldsymbol{\kappa}$ and $\mathrm{d}\boldsymbol{Q}/\mathrm{d}\boldsymbol{\kappa}$ are required. The conditions for the implicit function theorem is assumed to be fulfilled, see discussions in (Hartmann, 2017)). A function

$\boldsymbol{Q}_{ni} = \hat{\boldsymbol{Q}}(\boldsymbol{U}_{ni}(\boldsymbol{\kappa}), \boldsymbol{\kappa})$ is defined to describe the stage quantities of the internal variables and is then inserted into Eq.(4.59)$_1$,

$$\boldsymbol{g}\big(T_{ni}, \boldsymbol{U}_{ni}(\boldsymbol{\kappa}), \hat{\boldsymbol{Q}}(\boldsymbol{U}_{ni}(\boldsymbol{\kappa}), \boldsymbol{\kappa}), \boldsymbol{\kappa}\big) = \boldsymbol{0}, \tag{4.60}$$

and the derivative with respect to $\boldsymbol{\kappa}$ is calculated omitting the temporal index $ni$ for brevity,

$$\left[\frac{\partial \boldsymbol{g}}{\partial \boldsymbol{U}} + \frac{\partial \boldsymbol{g}}{\partial \boldsymbol{Q}} \frac{\mathrm{d}\hat{\boldsymbol{Q}}}{\mathrm{d}\boldsymbol{U}}\right] \frac{\mathrm{d}\boldsymbol{U}}{\mathrm{d}\boldsymbol{\kappa}} = -\frac{\partial \boldsymbol{g}}{\partial \boldsymbol{\kappa}} - \frac{\partial \boldsymbol{g}}{\partial \boldsymbol{Q}} \frac{\partial \hat{\boldsymbol{Q}}}{\partial \boldsymbol{\kappa}}. \tag{4.61}$$

It may be noted that the quantity within the braces on the left hand side (LHS) is the same as the tangential stiffness from non-linear solver. The matrix $\partial \hat{\boldsymbol{Q}}/\partial \boldsymbol{\kappa}$ is obtained from the Eq.(4.59)$_2$ by applying again the chain rule

$$\left[\frac{\partial \boldsymbol{I}}{\partial \boldsymbol{U}} + \frac{\partial \boldsymbol{I}}{\partial \boldsymbol{Q}} \frac{\mathrm{d}\hat{\boldsymbol{Q}}}{\mathrm{d}\boldsymbol{U}}\right] \frac{\mathrm{d}\boldsymbol{U}}{\mathrm{d}\boldsymbol{\kappa}} + \frac{\partial \boldsymbol{I}}{\partial \boldsymbol{Q}} \frac{\partial \hat{\boldsymbol{Q}}}{\partial \boldsymbol{\kappa}} + \frac{\partial \boldsymbol{I}}{\partial \boldsymbol{S}^{\mathrm{q}}} \frac{\mathrm{d}\hat{\boldsymbol{S}}^{\mathrm{q}}}{\mathrm{d}\boldsymbol{\kappa}} + \frac{\partial \boldsymbol{I}}{\partial \boldsymbol{\kappa}} = \boldsymbol{0}. \tag{4.62}$$

From Eq.(4.42), it is already known that the quantity within the braces on the LHS vanishes, see (Hartmann, 2017). With $\partial \boldsymbol{I}/\partial \hat{\boldsymbol{S}}^{\mathrm{q}} = -\boldsymbol{1}$, the linear system

$$\frac{\partial \boldsymbol{I}}{\partial \boldsymbol{Q}} \frac{\partial \hat{\boldsymbol{Q}}}{\partial \boldsymbol{\kappa}} = \frac{\mathrm{d}\hat{\boldsymbol{S}}^{\mathrm{q}}}{\mathrm{d}\boldsymbol{\kappa}} - \frac{\partial \boldsymbol{I}}{\partial \boldsymbol{\kappa}} \tag{4.63}$$

is solved in each stage at each Gauss-points. This solution is then inserted into Eq.(4.61). These sensitivities can be determined with the help of *Acegen* which is explained in detail in Sec.4.6. Once these quantities are available, the sensitivity of the Lagrange-multipliers can be determined by substitution.

## 4.6. Implementation of Parameter Identification Procedure

The entire finite element program has been written in a FORTRAN based code *TASAFEM*, see (Hartmann, 2006). The material models are also implemented in TASAFEM. In certain cases, the FE program Abaqus is also used. To identify the parameters, the algorithm already implemented in Matlab ® in the subroutine `lsqnonlin.m` is used. The Matlab routine calls the FE program TASAFEM in order to compare the experimental data and simulation data. The sensitivities derived in (4.44) and (4.54) can be determined using Acegen, (Korelc, 1997, 2002, 2009). The material model and the corresponding sensitivity measures are programmed using the Acegen plugin in Mathematica. Acegen outputs FORTRAN routines which are then combined with the in-house FEM code TASAFEM to determine the sensitivities. These sensitivities are then fed to the Matlab program which identifies the material parameters. The following flowchart depicts the flowchart of the entire identification procedure when using IND method for determining sensitivities with TASAFEM, see Fig.4.6. In the case of black-box FEM solvers like Abaqus and Ansys, IND cannot be used and thus END is used to solve the parameter identification problem.

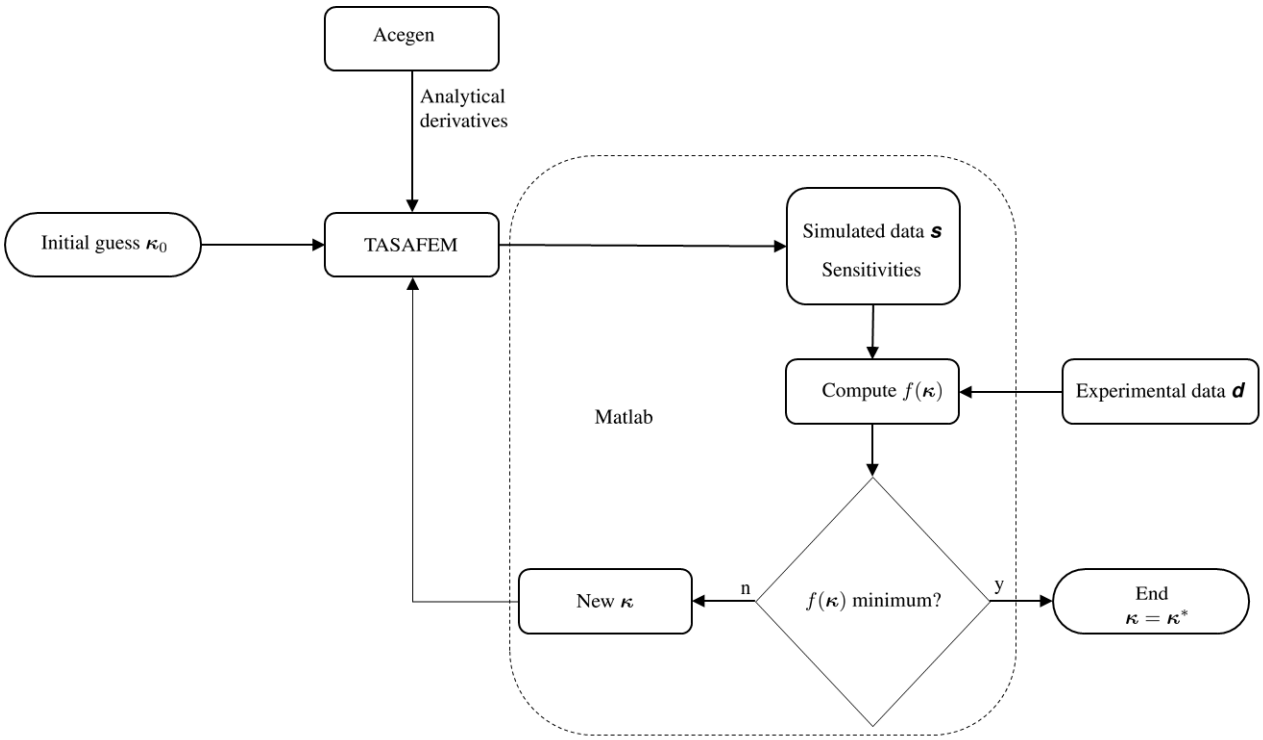


Figure 4.1.: Flowchart of the entire identification procedure when using IND

# 5. Examples

In this chapter, at first several examples to understand the concept of local identifiability is investigated. Different cases based on classical examples of small strain like uniaxial tension, biaxial tension etc. along with examples of large strain like indentation tests are investigated. Based on these investigations, a complex real world example for parameter identification using finite elements, including the determination of sensitivities, is discussed. A carbon black-filled rubber specimen was used to perform biaxial experiments. An extension of the overstress-type viscoelastic model according to Hartmann (2002) was assumed to be the constitutive model. The FORTRAN based code *TASAFEM*, see (Hartmann, 2006), was extended to include the model as well as the calculation of sensitivities explained in Section 4.4. Finally, the computational cost for the identification process using different methods to determine sensitivities are compared.

## 5.1. Investigation of Local Identifiability

In this section, a few examples are studied to understand the concept of identifiability. Wherever analytical sensitivities could be calculated, they have been provided. The best example to study identifiability in the context of mechanics is problems of linear, isotropic elasticity. The stress-strain relation for this case is given by

$$\mathbf{T} = K(\operatorname{tr}\mathbf{E})\mathbf{I} + 2G\mathbf{E}^D = \frac{E}{1+\nu}\left(\mathbf{E} + \frac{\nu}{1-2\nu}(\operatorname{tr}\mathbf{E})\mathbf{I}\right). \tag{5.1}$$

Here, $K = E/(3(1-2\nu))$ is the bulk modulus, $G = E/(2(1+\nu))$ the shear modulus, $E$ the Young's modulus and $\nu$ the Poisson's ratio. The representation $(5.1)_1$ of the elasticity relation is common in constitutive modeling, like for example, viscoplasticity or viscoelasticity. $\operatorname{tr}\mathbf{E} = \varepsilon_{11}+\varepsilon_{22}+\varepsilon_{33}$ is the first invariant of the linearized strain tensor $\mathbf{E} = (\operatorname{grad}\vec{u}(\vec{x}) + \operatorname{grad}^T\vec{u}(\vec{x}))/2$. $\mathbf{E}^D = \mathbf{E} - \big((\operatorname{tr}\mathbf{E})/3\big)\mathbf{I}$ is the deviator operator.

In the following subsections, identification of the material parameters $K$ and $G$ (or $E$ and $\nu$) on the basis of simple tension, two-layered specimens under tensile load, torsion, and thick-walled tubes under internal pressure (with one or two layers) are presented. To investigate identifiability, synthetic data are generated using the known parameters $K$ and $G$ (assumed as $K = 20\,\mathrm{MPa}$, $G = 15\,\mathrm{MPa}$, i.e. $E = 36\,\mathrm{MPa}$ and $\nu = 0.2$). Using these synthetic data as 'experimental data', the material parameters are re-identified, see (Hartmann and Gilbert, 2018) for a more comprehensive explanation.

### 5.1.1. Uniaxial Tensile Test

A uniaxial tensile problem in $x_1$-direction (compression is included as well) is assumed to obtain from Eq.(5.1)

$$\sigma_{11} = E\varepsilon_{11} = \frac{9KG}{3K+G}\varepsilon_{11}, \qquad \varepsilon_{22} = \varepsilon_{33} = -\nu\varepsilon_{11} = -\frac{3K-2G}{6K+2G}\varepsilon_{11}, \tag{5.2}$$

i.e. $\sigma_{11} = h(\varepsilon_{11}, K, G)$ and $\varepsilon_{22} = g(\varepsilon_{11}, K, G)$. This equation is investigated with regards to the quality measures and concept of identifiability. In the first case, only the (experimental) information in axial direction is considered, while, in the second example, both axial and lateral experimental information are considered.

#### 5.1.1.1. Pure Axial Information

It is assumed that experimental data is provided at only two points $(\varepsilon/2, d_1)$ and $(\varepsilon, d_2)$ where $\varepsilon/2$ and $\varepsilon$ are the given strains. $d_1$ and $d_2$ are the experimental measurements, i.e. in this case, the axial stresses at the strain levels $\varepsilon/2$ and $\varepsilon$. Exact stress data is assumed leading to the first term in the Hessian (4.16) vanishing. The Jacobian reads

$$\boldsymbol{J}(\boldsymbol{\kappa}) = \begin{bmatrix} \dfrac{\partial h(\varepsilon/2, K, G)}{\partial K} & \dfrac{\partial h(\varepsilon/2, K, G)}{\partial G} \\ \dfrac{\partial h(\varepsilon, K, G)}{\partial K} & \dfrac{\partial h(\varepsilon, K, G)}{\partial G} \end{bmatrix} = \begin{bmatrix} \dfrac{9G^2\varepsilon}{2\,(G+3\,K)^2} & \dfrac{27K^2\varepsilon}{2\,(G+3\,K)^2} \\ \dfrac{9G^2\varepsilon}{(G+3\,K)^2} & \dfrac{27K^2\varepsilon}{(G+3\,K)^2} \end{bmatrix}, \tag{5.3}$$

and the Hessian reads

$$\boldsymbol{H} = \boldsymbol{J}^T\boldsymbol{J} = \begin{bmatrix} \dfrac{405G^4\varepsilon^2}{4(G+3K)^4} & \dfrac{1215G^2K^2\varepsilon^2}{4(G+3K)^4} \\ \text{sym.} & \dfrac{3645K^4\varepsilon^2}{4(G+3K)^4} \end{bmatrix} \tag{5.4}$$

where the determinant $\det \boldsymbol{H} = 0$. This means that a unique local minimum is not possible. Since the determinant vanishes, other quality measures are also not calculated. If the goal function $f(K, G)$, along with the material parameters $\boldsymbol{\kappa}^T = \{K, G\}$ are plotted, see Fig.5.1, it can be seen that there is no unique local minimum. From the contour plot 5.1(b), a valley can be observed where there is no local solution and an infinite number of possible $K$ and $G$ combinations exists. This is due to the lack of information in the lateral direction. Obviously, if the same model is expressed in terms of Young's modulus and the Poisson's ratio, it can be clearly seen that the lack of lateral information make $\nu$ indeterminable. This very simple problem emphasizes the importance of the concept of identifiability and the need to perform identifiability studies, especially for complex boundary-value problems.

#### 5.1.1.2. Axial and Lateral Information

In this example, in addition to the axial information, the lateral information is also provided to the identification problem. The lateral strain is given in Eq.$(5.2)_2$. Similar to the first case, the

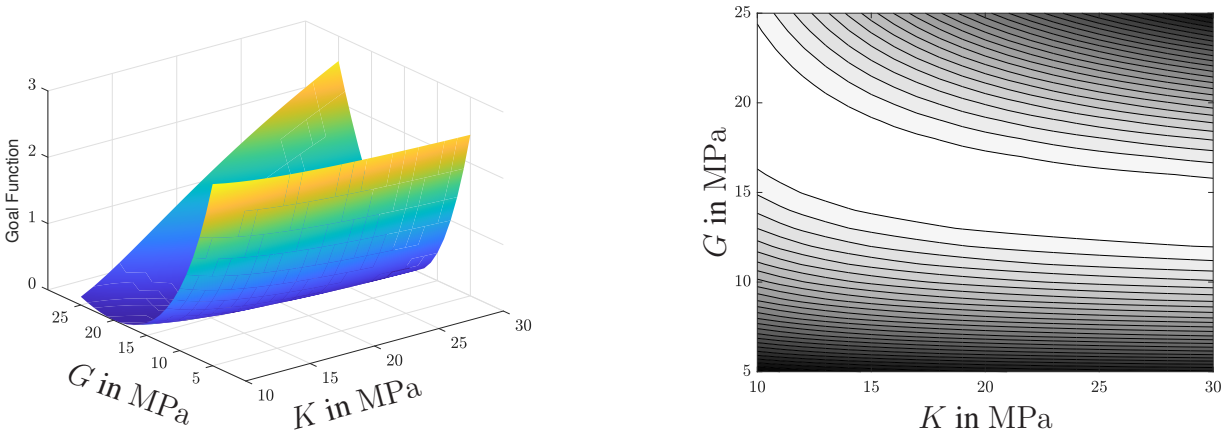


(a) Surface plot $f(K, G)$ (b) Contour plot $f(K, G)$

Figure 5.1.: Pure axial experimental information in tensile test

exact data is prescribed at two data points $\varepsilon/2$ and $\varepsilon$ leading to the Jacobian

$$\boldsymbol{J}(\boldsymbol{\kappa}) = \begin{bmatrix} \dfrac{\partial h(\varepsilon/2, K, G)}{\partial K} & \dfrac{\partial h(\varepsilon/2, K, G)}{\partial G} \\ \dfrac{\partial h(\varepsilon, K, G)}{\partial K} & \dfrac{\partial h(\varepsilon, K, G)}{\partial G} \\ \dfrac{\partial g(\varepsilon/2, K, G)}{\partial K} & \dfrac{\partial g(\varepsilon/2, K, G)}{\partial G} \\ \dfrac{\partial g(\varepsilon, K, G)}{\partial K} & \dfrac{\partial g(\varepsilon, K, G)}{\partial G} \end{bmatrix} = \begin{bmatrix} \dfrac{9G^2\varepsilon}{2(G+3K)^2} & \dfrac{27K^2\varepsilon}{2(G+3K)^2} \\ \dfrac{9G^2\varepsilon}{(G+3K)^2} & \dfrac{27K^2\varepsilon}{(G+3K)^2} \\ -\dfrac{9G\varepsilon}{4(G+3K)^2} & \dfrac{9K\varepsilon}{4(G+3K)^2} \\ -\dfrac{9G\varepsilon}{2(G+3K)^2} & \dfrac{9K\varepsilon}{2(G+3K)^2} \end{bmatrix} \tag{5.5}$$

with the Hessian being

$$\boldsymbol{H} = \boldsymbol{J}^T\boldsymbol{J} = \begin{bmatrix} \dfrac{405G^2\varepsilon^2\left(4G^2+1\right)}{16(G+3K)^4} & \dfrac{405GK\varepsilon^2\left(12GK-1\right)}{16(G+3K)^4} \\ \text{sym.} & \dfrac{405K^2\varepsilon^2\left(36K^2+1\right)}{16(G+3K)^4} \end{bmatrix}. \tag{5.6}$$

The determinant of the Hessian (5.6) reads

$$\det \boldsymbol{H} = \frac{164025G^2K^2\varepsilon^4}{64(G+3K)^6}, \tag{5.7}$$

and all the sub-determinant exists and is positive. Fig. 5.2 shows that there exists a local minimum and that unique identification is possible. Due to the mixing of strains and stress residuals, as expected, the dimensions are different which are weighted by using weighting matrices, for importance of weighing the residuum see Sec. 5.1.1.4. However, such weighting matrices have no influence on the notion of identifiability, see (Beck and Arnold, 1977). Thus, those matrices are ignored in these simple examples.

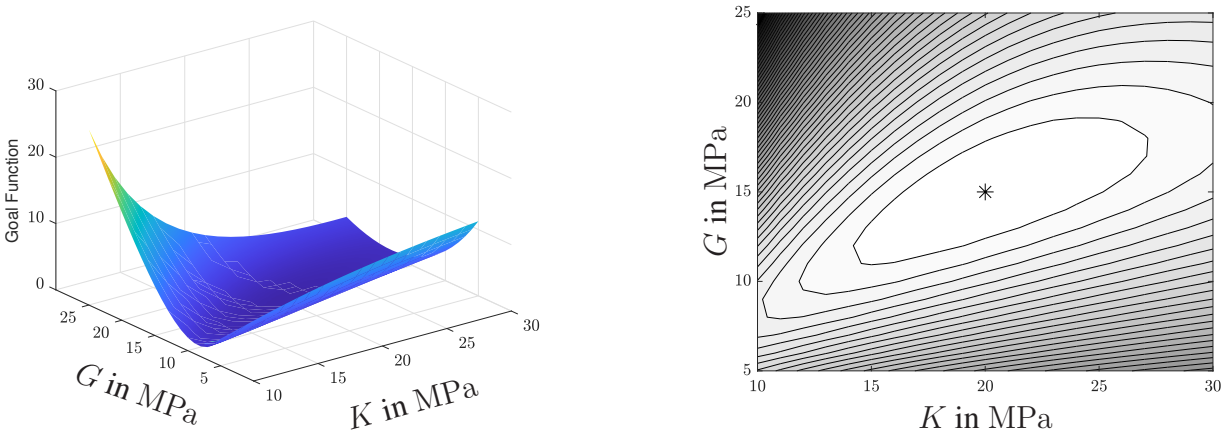


(a) Surface plot $f(K, G)$ (b) Contour plot $f(K, G)$

Figure 5.2.: Axial and lateral information in tensile test

### 5.1.1.3. Axial and Lateral Information with Perturbed Data

In order to study the quality measures of the identification detailed in Sec. 4.2, it must be ensured that the variance is a non-zero number. Since, using exact synthetic data produced by the model leads to a zero variance, certain perturbations are provided to the synthetic data. It must also be noted that in actual experiments, noise always exists. At first, exact data is generated using the model and then the data is perturbed by a standard deviation of 3%, see Figs. 5.3(a) and 5.3(b).

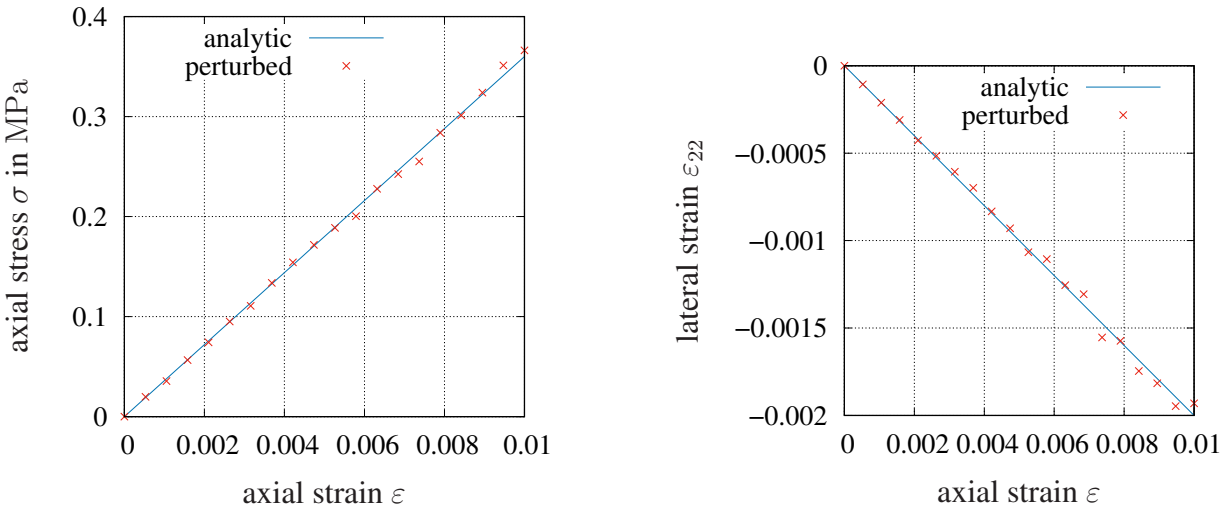


(a) Axial stress/strain diagram (b) Lateral strain/axial strain diagram

Figure 5.3.: Perturbed axial and lateral data in tensile test

Perturbation is done for both the axial and lateral data and re-identification is performed. In this example, a very good identification, $R^2 = 0.998$, with the material parameters $K =$

$20.014 \pm 7.72\,\mathrm{MPa}$ and $G = 15.01 \pm 1.44\,\mathrm{MPa}$ instead of $K = 20\,\mathrm{MPa}$ and $G = 15\,\mathrm{MPa}$ are obtained. The determinant of the approximated Hessian (4.23) is $\det \boldsymbol{H} \approx 3.8 \times 10^{-10} \approx 0$. The determinant of the Hessian vanishes as is to be expected when using weighted residuals. In such cases, the value of $\xi_p$ is to be checked. $\xi_p = 0.0002$ in this case is a positive number indicating the existence of a local unique minimum, see (Beck and Arnold, 1977) for more detailed explanation of $\xi_p$. The variance $s^2 = 1.8 \times 10^{-6}$. The correlation between the parameter is, see Eq.(4.21),

$$\boldsymbol{C} = \begin{bmatrix} 1 & -0.8421 \\ -0.8421 & 1 \end{bmatrix}.$$

The correlation matrix indicates that the material parameters $K$ and $G$ are correlated to each other on the basis of the given experimental data.

If the parameter set $(E, \nu)$ for this data would be determined, the correlation matrix is an identity matrix, i.e. there exists no correlation between those parameters, which are directly addressed by the experimental data. Fig. 5.4 shows that there exists a local minimum and that

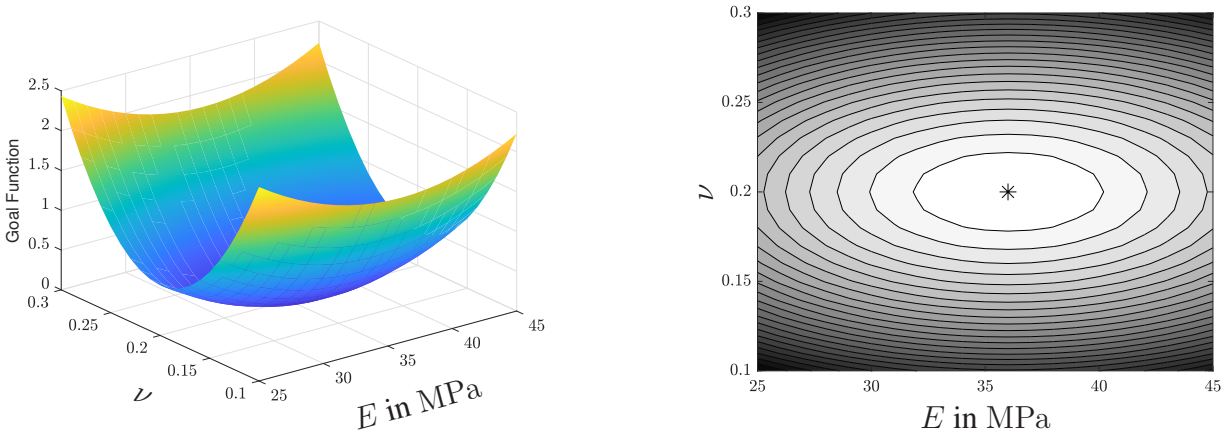


(a) Surface plot $f(E, \nu)$ (b) Contour plot $f(E, \nu)$

Figure 5.4.: Axial and lateral information in tensile test

unique identification is possible. Depending on the value of the correlation between material parameters, the shape of the contour in the contour plots vary. If the value is close to zero, the contour resembles a circle, see Fig. 5.4(b). The further the value is from zero, the shape becomes more and more elliptical, see Fig. 5.3(b).

#### 5.1.1.4. Importance of Weighting

Before going into further investigation about the local identifiability, the importance of weighting the residuum has to be detailed. In the previous section, it was emphasized that in some cases it is essential to weight the residuum, for example, in the case where data vector comprises of different quantities like force and surface displacements. This is also valid for cases when there is a large disparity in the number of data points of individual quantities. The importance of

weights is explained here with a very simple example. Firstly, a simple elastic case with material parameters $K = 200\,\mathrm{MPa}$ and $G = 15\,\mathrm{MPa}$ are assumed. It is also assumed that axial and lateral information exist. For axial information there exists $n_\mathrm{d} = 1000$ and for lateral information there exists $n_\mathrm{d} = 5$. If the residuum is left unweighted, the identification process results in $K = 158.63\,\mathrm{MPa}$ and $G = 15.07\,\mathrm{MPa}$. However, if the residuum is weighted appropriately, then exact parameters are re-identified. Thus, it is always essential to weigh the residuum appropriately whenever necessary, see Eq.(4.9).

#### 5.1.1.5. Two-layered Materials

In the case of two-layered materials with different material properties, for instance in bi-metallic strips, layered functionally graded polymers, or even in biomechanical applications such as arteries, the identification of material parameters of the individual layers is far more challenging that in the single layer case. If it is possible to separate the layers, then it is easier to identify the material parameters of individual layers. However, in cases where the separation isn't possible, identification becomes complicated. For example, in human radial arteries, layer separation is extremely difficult. That is one reason why the problem of identification with regards to arteries is still an open problem, see (Gilbert et al., 2016). In the following investigations, a general and more directly example is investigated. First, a tensile test of a two-layered material is considered, see Fig. 5.5. With regard to arteries, this can be interpreted as the *ring test*, see (Cox, 1982, 1983;

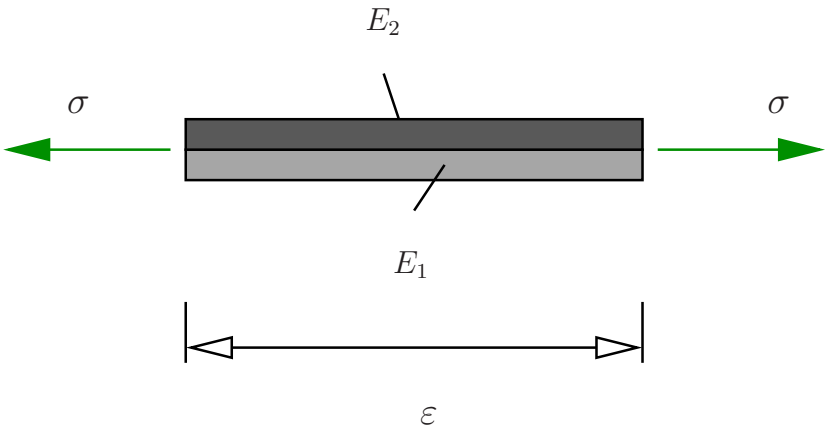


Figure 5.5.: Two materials in parallel, see (Hartmann and Gilbert, 2018)

Consigny et al., 1986).

Similar to the other examples two prescribed strains $\varepsilon/2$ and $\varepsilon$ are assumed with $E_1$ and $E_2$, the Young's moduli of the two materials, that are in parallel. For the materials in parallel, the total stress is the sum of the contributions from the two layers,

$$\sigma = \sigma_1 + \sigma_2 = E_1\varepsilon + E_2\varepsilon = h(\varepsilon, E_1, E_2) = (E_1 + E_2)\varepsilon. \tag{5.8}$$

The Jacobian reads

$$\boldsymbol{J} = \begin{bmatrix} \dfrac{\partial h(\varepsilon/2, E_1, E_2)}{\partial E_1} & \dfrac{\partial h(\varepsilon/2, E_1, E_2)}{\partial E_2} \\ \dfrac{\partial h(\varepsilon, E_1, E_2)}{\partial E_1} & \dfrac{\partial h(\varepsilon, E_1, E_2)}{\partial E_2} \end{bmatrix} = \begin{bmatrix} E_2(\varepsilon/2) & E_1(\varepsilon/2) \\ E_2\varepsilon & E_1\varepsilon \end{bmatrix} \tag{5.9}$$

and the Hessian at the prescribed data points is given by

$$\boldsymbol{H} = \boldsymbol{J}^T\boldsymbol{J} = \begin{bmatrix} E_2^2 & E_1E_2 \\ E_1E_2 & E_1^2 \end{bmatrix} \frac{5\varepsilon^2}{4}. \tag{5.10}$$

Here, the $\det \boldsymbol{H} = 0$, which indicates that there is no unique solution.

This hold for the constitutive equations modeled with $\boldsymbol{\kappa}^T = \{K_1, G_1, K_2, G_2\}$.

$$\boldsymbol{J} = \begin{pmatrix} \frac{9{G_1}^2\varepsilon}{2(G_1+3K_1)^2} & \frac{27{K_1}^2\varepsilon}{2(G_1+3K_1)^2} & \frac{9{G_2}^2\varepsilon}{2(G_2+3K_2)^2} & \frac{27{K_2}^2\varepsilon}{2(G_2+3K_2)^2} \\ \frac{9{G_1}^2\varepsilon}{(G_1+3K_1)^2} & \frac{27{K_1}^2\varepsilon}{(G_1+3K_1)^2} & \frac{9{G_2}^2\varepsilon}{(G_2+3K_2)^2} & \frac{27{K_2}^2\varepsilon}{(G_2+3K_2)^2} \end{pmatrix} \tag{5.11}$$

is the Jacobian at the two experimental points with prescribed strains, $\varepsilon/2$ and $\varepsilon$. The Hessian reads

$$\boldsymbol{H} = \begin{pmatrix} \frac{405{G_1}^4\varepsilon^2}{4(G_1+3K_1)^4} & \frac{1215{G_1}^2{K_1}^2\varepsilon^2}{4(G_1+3K_1)^4} & \frac{405{G_1}^2{G_2}^2\varepsilon^2}{4(G_1+3K_1)^2(G_2+3K_2)^2} & \frac{1215{G_1}^2{K_2}^2\varepsilon^2}{4(G_1+3K_1)^2(G_2+3K_2)^2} \\ \frac{1215{G_1}^2{K_1}^2\varepsilon^2}{4(G_1+3K_1)^4} & \frac{3645{K_1}^4\varepsilon^2}{4(G_1+3K_1)^4} & \frac{1215{G_2}^2{K_1}^2\varepsilon^2}{4(G_1+3K_1)^2(G_2+3K_2)^2} & \frac{3645{K_1}^2{K_2}^2\varepsilon^2}{4(G_1+3K_1)^2(G_2+3K_2)^2} \\ \frac{405{G_1}^2{G_2}^2\varepsilon^2}{4(G_1+3K_1)^2(G_2+3K_2)^2} & \frac{1215{G_2}^2{K_1}^2\varepsilon^2}{4(G_1+3K_1)^2(G_2+3K_2)^2} & \frac{405{G_2}^4\varepsilon^2}{4(G_2+3K_2)^4} & \frac{1215{G_2}^2{K_2}^2\varepsilon^2}{4(G_2+3K_2)^4} \\ \frac{1215{G_1}^2{K_2}^2\varepsilon^2}{4(G_1+3K_1)^2(G_2+3K_2)^2} & \frac{3645{K_1}^2{K_2}^2\varepsilon^2}{4(G_1+3K_1)^2(G_2+3K_2)^2} & \frac{1215{G_2}^2{K_2}^2\varepsilon^2}{4(G_2+3K_2)^4} & \frac{3645{K_2}^4\varepsilon^2}{4(G_2+3K_2)^4} \end{pmatrix}. \tag{5.12}$$

with the determinant $\det \boldsymbol{H} = 0$. Thus, unique material parameters cannot be expected for a layered material from a tensile test since only a globally (integral) measured force and no measured stresses within each layer are available. This means that for two-layered materials, it is essential that information from each layers need to be fed to the optimizer. In such cases, strain data or displacement data from each layer can be used to identify the parameters.

### 5.1.2. Torsion

In the case of linear elasticity, a linear distribution of shear stress over the radius is expected for the torsion of thick-walled circular tubes. Naturally, constant shear stress can be assumed in the case of thin-walled tubes, see (Timoschenko and Goodier, 1985),

$$M_T = G\frac{I_T}{L_0}\vartheta. \tag{5.13}$$

Here, $M_T$ is the torque, $\vartheta$ the torsional angle, $I_T = 2\pi R^3 d$ the polar moment of inertia, $R$ the mean radius, $d$ the tube's wall thickness, and $L_0$ the length (or height) of the specimen. Obviously, from Eq.(5.13) it is clear that only the shear modulus $G$ can be determined from the

torsion experiments. Hence, a combined tension-torsion experiment is required to provide both the elastic modulus and the shear modulus. A simple example can be demonstrated with the help of the axial information from the Section 5.1.1.3 and synthetic torque data calculated using $G = 15\,\mathrm{MPa}$, $\vartheta = 0.34\,\mathrm{rad}$, $R = 10\,\mathrm{mm}$, $d = 1\,\mathrm{mm}$ and $L_0 = 100\,\mathrm{mm}$. When using axial data along with the torque data, $K = 19.67 \pm 0.43\,\mathrm{MPa}$ and $G = 15.07 \pm 0.24\,\mathrm{MPa}$ are obtained which is a very good approximation of the parameters. The value of $\det \boldsymbol{H} = 0.043$ which indicates a local minimum. Thus it may be noted that if lateral information is not accessible, it is sufficient to combine axial data (integral quantity) from uniaxial experiment with torque (another integral quantity) that can be measured by performing torsion experiments, to identify the bulk modulus $K$ and shear modulus $G$.

Measurement of purely integral quantities like axial force and/or the resulting torque will not provide sufficient information to determine all four material parameters in the case of a two-layered tube under tension and torsion (two parameters each from each layers), see discussion in Section 5.1.1.5. In such cases, displacement or strain values under tension or torsion from individual layers need to be addressed to identify the parameters.

## 5.1.3. Biaxial Tensile Tests

In recent years, the biaxial tensile experiments are getting attractive, due to the fact that good digital full-field measurement systems (digital image correlation – DIC) are available at reasonable prices. For biaxial experiments involving metal specimens, see, for instance, (Hannon and Tiernan, 2008), or regarding polymer foils, for example, (Ognedal et al., 2012; Lamkanfi et al., 2015; Hartmann et al., 2018a), and the literature cited therein. However, a major drawback of biaxial tensile tests is that it is inappropriate to develop new material models as the stress state in the center region of the specimen is unknown. Thus, these experiments are mainly used to perform material parameter identification and validation of already existing constitutive models, see (Schmaltz and Willner, 2013, 2014; Hanabusa et al., 2013).

For the analysis of biaxial tests, two separate cases are considered. The first case is based on analytical estimation of the plane stress problem meanwhile the second case is based on the numerical estimation.

### 5.1.3.1. Analytical

The analytical estimation of an plane stress problem can be summarized from Eq.(5.1)

$$\begin{Bmatrix} \sigma_{xx} \\ \sigma_{yy} \\ \tau_{xy} \end{Bmatrix} = \frac{E}{1-\nu^2} \begin{bmatrix} 1 & \nu & 0 \\ \nu & 1 & 0 \\ 0 & 0 & \frac{1-\nu}{2} \end{bmatrix} \begin{Bmatrix} \varepsilon_{xx} \\ \varepsilon_{yy} \\ \gamma_{xy} \end{Bmatrix}. \tag{5.14}$$

A quarter of a cruciform specimen, see Fig. 5.6, is investigated (thickness $t = 1\,\mathrm{mm}$) in the following examples.

**Equibiaxial tests and re-identification using exact force data** As a first case, displacements of $u_x = u_y = 0.4\,\mathrm{mm}$ are assumed to be applied at the end of both arms of the one

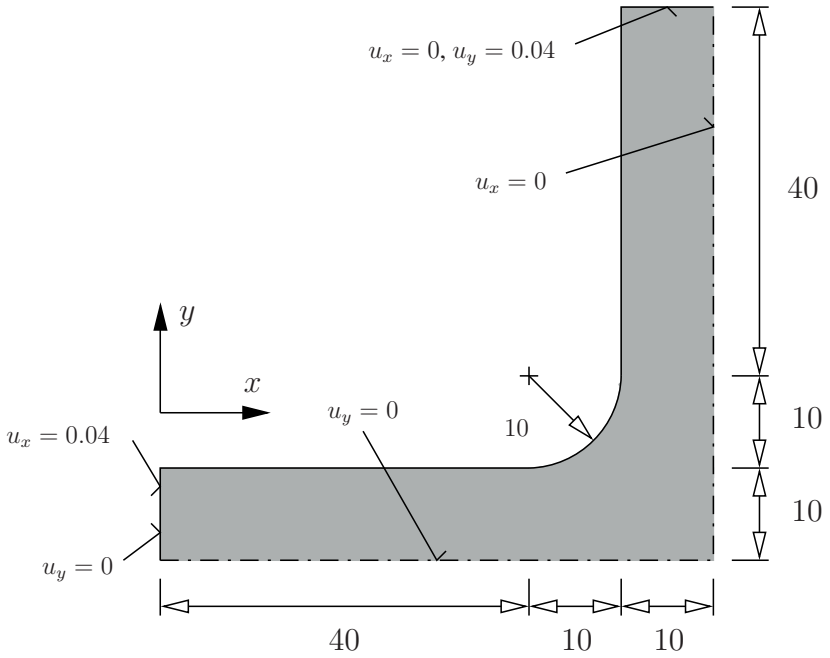


Figure 5.6.: Geometry and boundary conditions (measures in $\mathrm{mm}$), see (Hartmann and Gilbert, 2018)

quarter of the specimen (because of symmetry) and the resulting stresses at the arms $\sigma_{xx}$ and $\sigma_{yy}$ are calculated from the Eq.(5.14). In the equibiaxial case the stresses are identical, $\sigma_{xx} = \sigma_{yy}$. It is assumed that only these integral quantities are available. Using the synthetic data, a re-identification process was performed. It was found out that the result of re-identification is $\det \boldsymbol{H} \approx 0$, implying no local unique minimum. This implies that the elasticity parameters $E$ and $\nu$ are not uniquely identifiable (valid for $K$ and $G$ as well). This phenomenon can be seen in the analytical estimation of an equibiaxial plane stress problem. Under the assumption of symmetry $\sigma := \sigma_{xx} = \sigma_{yy}$ and $\varepsilon := \varepsilon_{xx} = \varepsilon_{yy}$ as well as $\gamma_{xy} = 0$ yields

$$\sigma = \frac{E}{1-\nu}\varepsilon. \tag{5.15}$$

Thus only one equation (one information) is available to determine two material parameters. Thus, a non-equibiaxial test has to be carried out to obtain the material parameters.

**Biaxial tests and re-identification using exact force data** Instead of equibiaxial tests, if a biaxial tensile test with $u_x = 0.4\,\mathrm{mm}$ (horizontal arm) and $u_y = u_x/4$ (vertical arm) are performed, for the measured force $\sigma_{xx} \neq \sigma_{yy}$, a non-vanishing determinant of the Hessian, $\det \boldsymbol{H} \approx 0.0001$ is obtained with exact representation of the "experimental" data, $R^2 = 1$. The prescribed material parameters can be re-identified exactly and the confidence interval is zero for both parameters while the other quality measures cannot be analysed due to vanishing variance. Thus, the data have to be perturbed.

**Biaxial tests and re-identification using perturbed force data** The force data of $\sigma_{xx}$ and $\sigma_{yy}$ from the previous test is perturbed (10 data points are chosen). The result of the re-identification obtained is $E = 35.71 \pm 2.1\text{MPa}$ and $\nu = 0.21 \pm 0.14$. It can be noted that the confidence interval of the Poisson's ratio is not adequate even though the parameters are unique, $\det \boldsymbol{H} \approx 0.00012$. This can also be seen from the correlation coefficient $C_{12} = -0.81$ which indicates a strong correlation. From this example, it is clear that using purely an integral quantity like force is not adequate to identify material parameters with sufficient quality.

### 5.1.3.2. Numerical

In the following, finite element computations are done with the same assumed material parameters $E = 36\,\text{MPa}$ and $\nu = 0.2$ (representing $K = 30\,\text{MPa}$ and $G = 15\,\text{MPa}$). Fig. 5.7(a) represents the geometry and the meshing of the cruciform specimen. The FE computations are performed in Abaqus using C3D8 elements. It is assumed that access to DIC-system is available (nodal displacements from synthetic data). This provides with the information about the in-plane surface displacements in the center region of the specimen. Here, the nodal displacements of the direct problem is taken (the quadrilateral region of the mesh in the center, see Fig.5.7(b)) along with the force data – both are perturbed by a standard deviation of $3\%$ (10 data points).

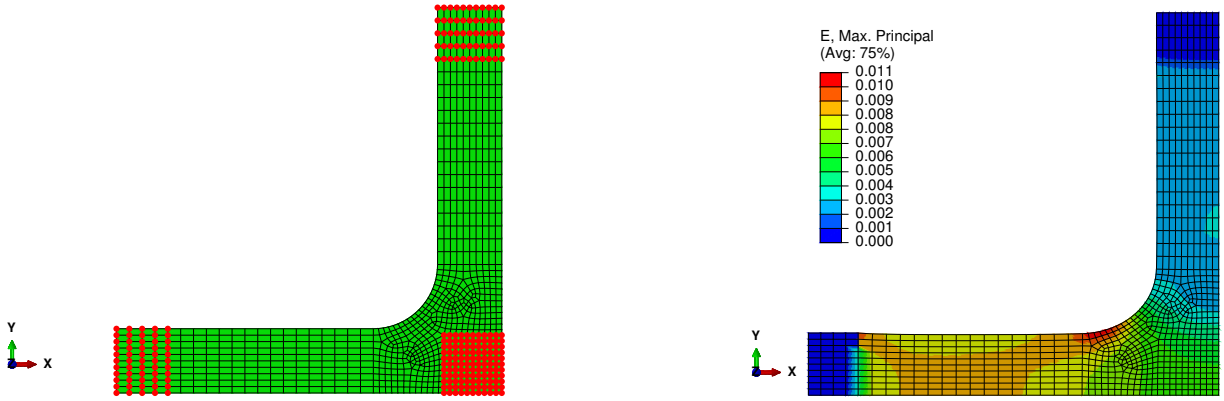


(a) Geometry and mesh of the specimen (measures in $\text{mm}$)

(b) Maximum principal strain

Figure 5.7.: Biaxial tensile test

**Biaxial tests and re-identification using perturbed force data and surface displacements** Re-identification is performed for $u_x = 0.4\,\text{mm}$ (horizontal arm) and $u_y = u_x/4$ (vertical arm) so that the tests are non-equibiaxial. Since the surface displacements are also used, the residual needs to be weighted. The parameters obtained by re-identification are $E = 35.34 \pm 0.0125\,\text{MPa}$ and $\nu = 0.21 \pm 0.008$ with a very small confidence interval. The correlation coefficient is $C_{12} = -0.24$ showing very weak correlation. The variance $s^2 = 2.3 \times 10^{-6}$ while the determinant of the Hessian $\det \boldsymbol{H} \approx 2.4 \times 10^{-8}$. However, the low value of $\det \boldsymbol{H}$ doesn't imply that the parameters are not identifiable. $\xi_p = 0.24$ represents that there exists a local unique

solution. This clearly shows that the two material parameters can be reliably identified if force data along with full-field information are considered for identification.

**Equibiaxial tests and re-identification using perturbed force data and surface displacements** From the previous study, a certain question arises – whether an equibiaxial tensile test can be used to determine reliable parameters using perturbed force and full-field data. A displacement of $u_x = u_y = 0.4\,\mathrm{mm}$ is applied on both the arms and the forces $F_x$ and $F_y$ as well as surface displacements are measured. These data are then perturbed and parameters are re-identified. The value $\xi_p = 0.012$ shows local unique minimum can be achieved. However, confidence interval is relatively high, $E = 34.78 \pm 5.24$ MPa with $\nu = 0.19 \pm 0.13$. The correlation coefficient between the material parameters are also very strong, $C_{12} = -0.92$.

It has to be noted that when exact data for force and full-field information was used to identify the parameters for equibiaxial case re-identifying exact parameters. This means that that full-field information can minimize problems in identification to a certain extent. However, for a two-layered specimen the same problems as in the case of uniaxial tensile tests occur as information is available only from the surface of one of the specimen. Thus, in two-layered specimen problems, the unique parameters are indeterminable unless surface information from two different layers are available.

## 5.1.4. Thick-walled Tube under Internal Pressure

A different possibility to determine the parameters of elasticity is the case of a thick-walled tube under internal pressure $p$. The internal pressure is prescribed and the radial displacements at the outer surface are measured (either by optical measurements, see the method described in (Hartmann et al., 2003), or by an appropriate sensor, see (Bier et al., 2007)). Another possibility is to apply strain gauges to determine the circumferential strains, see (Lefebvre et al., 1983; Carnavas and Page, 1998). A thick-walled tube under internal pressure is a classical example of inhomogeneous deformation with the displacements at the outer surface. The problem is formulated as

$$\hat{u}(r_o, p, E, \nu) = u(r_o, p, K, G) = \frac{2pr_o}{E}\frac{1-\nu^2}{d_r^2-1} = \frac{pr_o(4G+3K)}{2(d_r^2-1)(G^2+3KG)}, \tag{5.16}$$

and the axial stress

$$\sigma_z(p, K, G) = \frac{2p\nu}{d_r^2-1} = \frac{2p(3K-2G)}{(d_r^2-1)\,(2G+6K)}, \tag{5.17}$$

where $d_r = r_o/r_i$ is the thickness ratio of the outer and inner radius $r_o$ and $r_i$, see (Lehmann, 1984; Hartmann and Gilbert, 2018; Hartmann et al., 2018b) (for $\varepsilon_z = 0$ and $p_o = 0$). The axial stress is constant over the radius so that the resulting force, measured by a testing machine, is $F_z = \sigma_z a$ with the cross-section $a = \pi(r_o^2 - r_i^2)$. Fig. 5.8(a) represents the boundary-value problem.

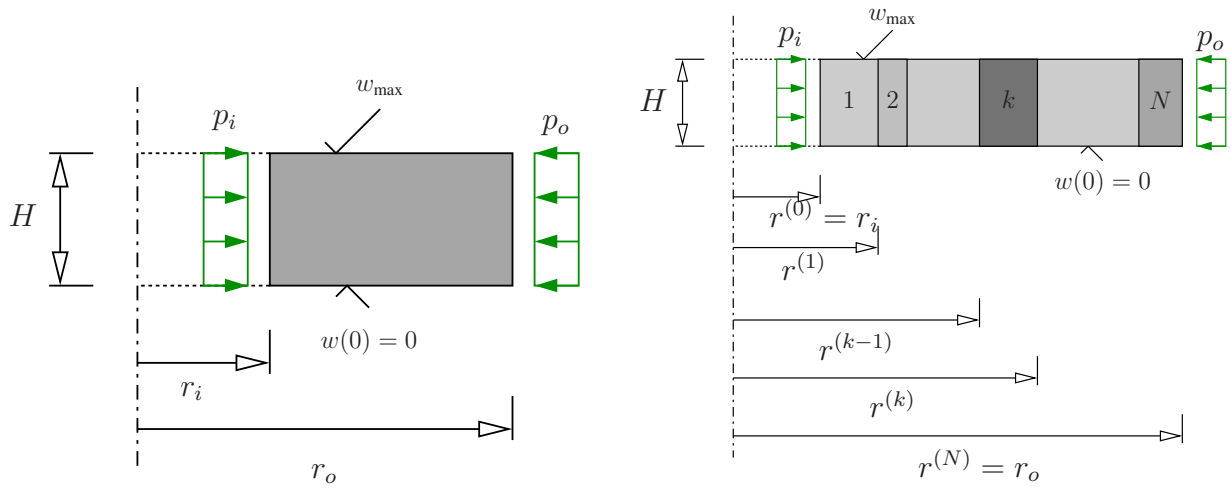


(a) One layer (b) Several layers

Figure 5.8.: Single and multi-layered thick-walled tube under internal and external pressure with axial strain, see (Hartmann and Gilbert, 2018)

#### 5.1.4.1. Pure Radial Information

It is assumed that experimental data exists for two pressure points with values for pressure set at $p/2$ and $p$. The corresponding radial displacements (5.16) are measured at the outer radius where $r_o = 5\,\mathrm{mm}$ and $d_r = 5$. The Jacobian reads

$$\boldsymbol{J}(\boldsymbol{\kappa}) = \begin{bmatrix} \dfrac{\partial u(r_o, p/2, K, G)}{\partial K} & \dfrac{\partial u(r_o, p/2, K, G)}{\partial G} \\ \dfrac{\partial u(r_o, p, K, G)}{\partial K} & \dfrac{\partial u(r_o, p, K, G)}{\partial G} \end{bmatrix} \tag{5.18}$$

$$= \begin{bmatrix} -\dfrac{9pr_o}{4\,(d_r^2-1)\,(G+3K)^2} & -\dfrac{(4G^2+6KG+9K^2)\,pr_o}{4\,(d_r^2-1)\,G^2(G+3K)^2} \\ -\dfrac{9pr_o}{2\,(d_r^2-1)\,(G+3K)^2} & -\dfrac{(4G^2+6KG+9K^2)\,pr_o}{2\,(d_r^2-1)\,G^2(G+3K)^2} \end{bmatrix} \tag{5.19}$$

leading to the Hessian

$$\boldsymbol{H} = \boldsymbol{J}^T\boldsymbol{J} = \begin{bmatrix} \dfrac{405p^2r_o^2}{16\,(d_r^2-1)^2\,(G+3K)^4} & \dfrac{45\,(4G^2+6KG+9K^2)\,p^2r_o^2}{16\,(d_r^2-1)^2\,G^2(G+3K)^4} \\ \text{sym.} & \dfrac{5\,(4G^2+6KG+9K^2)^2\,p^2r_o^2}{16\,(d_r^2-1)^2\,G^4(G+3K)^4} \end{bmatrix}. \tag{5.20}$$

The determinant of the Hessian vanishes $\det \boldsymbol{H} = 0$ and thus no unique local minimum exists. Thus, additional information is required to obtain the material parameters $K$ and $G$ (this is also valid for $E$ and $\nu$). In Fig. 5.9, for re-identification of material parameters $K = 20\,\mathrm{MPa}$, $G = 15\,\mathrm{MPa}$ ($E = 36\,\mathrm{MPa}$ and $\nu = 0.2$), this property is visible in the long valley, where infinite

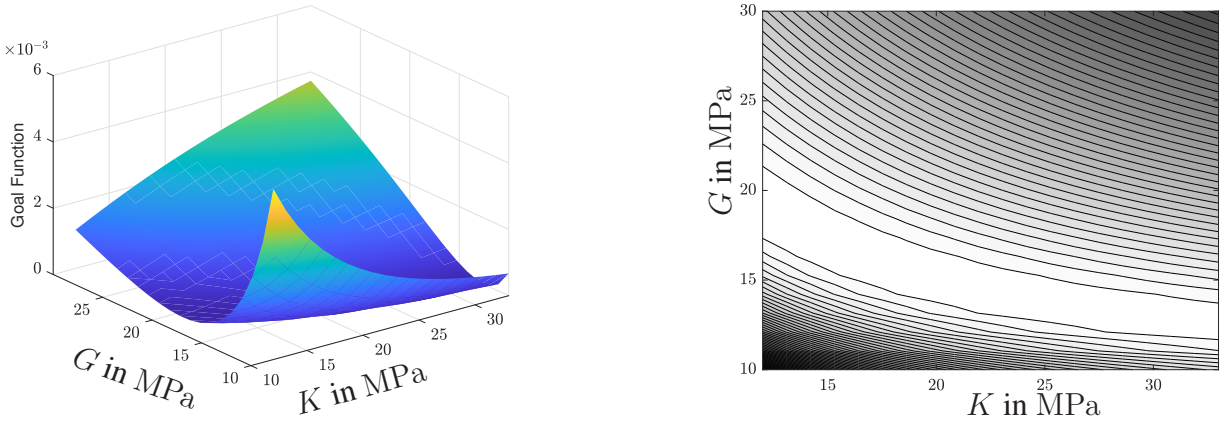


(a) Surface plot $f(K, G)$ (b) Contour plot $f(K, G)$

Figure 5.9.: Sum of squares of residuals of radial displacement (outer surface) of thick-walled tube under internal pressure, i.e. pure radial displacement information

combinations of material parameters are valid. Another possibility is, for example, an additional (separate) uniaxial tensile (or compression) test, which has to be combined with the thick-walled tube tests, or to look for a combined axially stretched and internally pressurized tube.

#### 5.1.4.2. Radial and Axial Information

In the following, in addition to the radial displacement (5.16), the axial stresses (5.17) are also provided. The Jacobian at the internal pressure points $p/2$ and $p$ are determined,

$$\boldsymbol{J}(\boldsymbol{\kappa}) = \begin{bmatrix} \dfrac{\partial u(r_o, p/2, K, G)}{\partial K} & \dfrac{\partial u(r_o, p/2, K, G)}{\partial G} \\ \dfrac{\partial u(r_o, p, K, G)}{\partial K} & \dfrac{\partial u(r_o, p, K, G)}{\partial G} \\ \dfrac{\partial \sigma_z(p/2, K, G)}{\partial K} & \dfrac{\partial \sigma_z(p/2, K, G)}{\partial G} \\ \dfrac{\partial \sigma_z(p, K, G)}{\partial K} & \dfrac{\partial \sigma_z(p, K, G)}{\partial G} \end{bmatrix} \tag{5.21}$$

$$= \begin{bmatrix} -\dfrac{9pr_o}{4\,(d_r^2-1)\,(G+3K)^2} & -\dfrac{(4G^2+6KG+9K^2)\,pr_o}{4\,(d_r^2-1)\,G^2(G+3K)^2} \\ -\dfrac{9pr_o}{2\,(d_r^2-1)\,(G+3K)^2} & -\dfrac{(4G^2+6KG+9K^2)\,pr_o}{2\,(d_r^2-1)\,G^2(G+3K)^2} \\ \dfrac{9Gp}{2\,(d_r^2-1)\,(G+3K)^2} & -\dfrac{9Kp}{2\,(d_r^2-1)\,(G+3K)^2} \\ \dfrac{9Gp}{(d_r^2-1)\,(G+3K)^2} & -\dfrac{9Kp}{(d_r^2-1)\,(G+3K)^2} \end{bmatrix}. \tag{5.22}$$

The Hessian reads

$$\boldsymbol{H} = \begin{bmatrix} \frac{405 r_o^2 p^2}{16(d_r^2-1)^2(G+3K)^4} + \frac{405 G^2 p^2}{4(d_r^2-1)^2(G+3K)^4} & \frac{45\left(4G^2+6KG+9K^2\right)p^2 r_o^2}{16(d_r^2-1)^2 G^2(G+3K)^4} - \frac{405 GKp^2}{4(d_r^2-1)^2(G+3K)^4} \\ \text{sym.} & \frac{5\left(4G^2+6KG+9K^2\right)^2 r_o^2 p^2}{16(d_r^2-1)^2 G^4(G+3K)^4} + \frac{405 K^2 p^2}{4(d_r^2-1)^2(G+3K)^4} \end{bmatrix} \tag{5.23}$$

where the determinant

$$\det \boldsymbol{H} = \frac{2025 p^4 r_o^2 (4G+3K)^2}{64\left(d_r^2-1\right)^4 G^2 (G+3K)^6}. \tag{5.24}$$

This clearly indicates that a unique local minimum exists which can be determined by the optimizer, see the goal function distribution in Fig. 5.10.

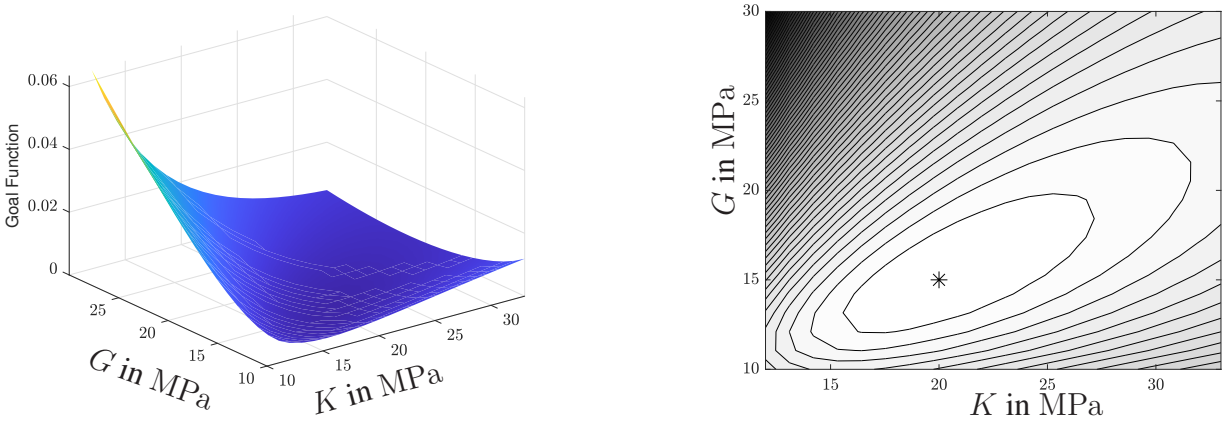


(a) Surface plot $f(K, G)$ (b) Contour plot $f(K, G)$

Figure 5.10.: Sum of squares of residuals of axial stress and radial displacement (outer surface) of thick-walled tube under internal pressure

#### 5.1.4.3. Thick-walled Tube with Two Layers

There are several applications of thick-walled tubes under internal and external pressure with multiple layers. One primary example is in drilling applications, see (Clifton et al., 1976; Yeh and Kyriakides, 1986; Bourgoyne, 1986; Bai et al., 1997; Shildip et al., 2015) or in biomechanical applications such as arteries, see, for example (Gasser et al., 2006; Sutton et al., 2011; Rachev and Shazly, 2013). Thus, investigations need to be performed for identifiability of the material parameters in each layer. Thus, boundary-value problem is sought to obtain the solution. However, analytical solution for the case of small-strain isotropic linear elasticity with several layers and combined axial strains is provided, see (Hartmann et al., 2018b; Hartmann and Gilbert, 2018), see Fig. 5.8(b) as well.

Two layers with inner radii $r_i = r^{(1)} = 1\,\mathrm{mm}$, $r^{(2)} = 2\,\mathrm{mm}$ and outer radii $r_o = r^{(2)} = 3\,\mathrm{mm}$ are chosen, for which the internal pressure and the axial strains are provided by four (synthetic data) points, $p_i = 1, 2, 3$ and $4\,\mathrm{MPa}$, $\varepsilon_z = 1, 2, 3$ and $4\,\%$, $p_o = 0\,\mathrm{MPa}$. Hartmann et al. (2018b);

Hartmann and Gilbert (2018) provide the resulting displacements at the outer surface and the resulting axial forces. These are used to re-identify the material parameters $K^{(1)} = 3\,\mathrm{MPa}$, $G^{(1)} = 1.5\,\mathrm{MPa}$, $K^{(2)} = 6\,\mathrm{MPa}$, and $G^{(2)} = 3\,\mathrm{MPa}$. The determinant of the Hessian can be computed analytically because the analytical solution is available. The equations are omitted for brevity. The determinant of the Hessian is $\det \boldsymbol{H} = 0$. Therefore, a unique local minimum is unavailable.

Now, the exact data were perturbed and re-identification was performed. As expected, the parameters cannot be uniquely identifiable.

Additionally, the radial displacements $u(r_i)$ at the inner side ("exact" experimental data) were also taken into consideration. Even this extra information, did not solve the problem with $\det \boldsymbol{H} = 0$. Thus, unique identification of the parameters is impossible. For more complex constitutive models like for human arteries with complex geometry, where two layers with 10 material parameters need to be identified, unique identification is extremely challenging, see (Gilbert et al., 2016).

### 5.1.5. 1D Small Strain Linear Viscoelasticity

As a next example, a simple 1D case of small strain linear viscoelasticity is investigated. In

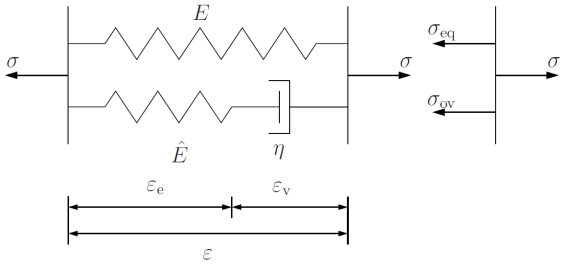


Figure 5.11.: Rheological model of 3-parameter model of viscoelasticity

the case of linear viscoelasticity, a combination of spring and damper elements are used and is modeled using the so-called 3-parameter model, see Fig. 5.11. The total strain $\varepsilon$ can be divided into elastic strain $\varepsilon_e$ and viscous strain $\varepsilon_v$,

$$\varepsilon = \varepsilon_e + \varepsilon_v. \tag{5.25}$$

The total stress can also be subdivided into equilibrium stress $\sigma_{\mathrm{eq}}$ and over stress $\sigma_{\mathrm{ov}}$,

$$\sigma = \sigma_{\mathrm{eq}} + \sigma_{\mathrm{ov}}. \tag{5.26}$$

Each rheological model is assigned a material property by means of constitutive equations,

$$\sigma_{\mathrm{eq}} = E\varepsilon, \quad \sigma_{\mathrm{ov}} = \hat{E}\varepsilon_e, \quad \sigma_{\mathrm{ov}} = \eta\dot{\varepsilon_v}. \tag{5.27}$$

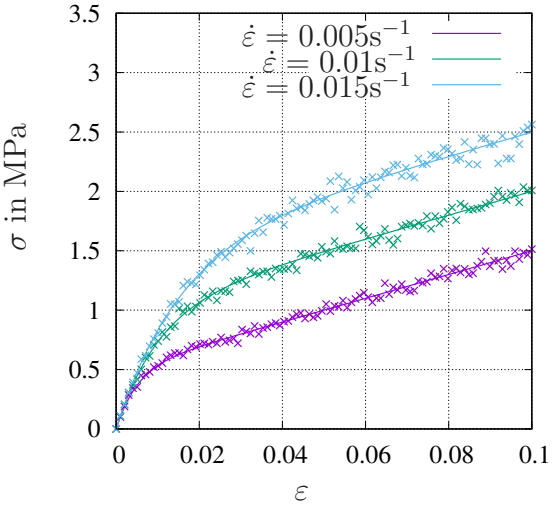


Figure 5.12.: Synthetic data

Combining the above equations (5.26) and (5.27), the stress relation

$$\sigma = \sigma_{\text{eq}} + \sigma_{\text{ov}} = E\varepsilon + \hat{E}\varepsilon_e = E\varepsilon + \hat{E}(\varepsilon - \varepsilon_v) \tag{5.28}$$

results, where an evolution equation is obtained

$$\dot{\varepsilon_v} = \frac{\hat{E}}{\eta}(\varepsilon - \varepsilon_v). \tag{5.29}$$

The stress equation, (5.28), is differentiated with respect to time and the rate of viscous strain (5.29) is substituted to obtain the ODE

$$\dot{\sigma}(t) + \frac{\hat{E}}{\eta}\sigma(t) = (E + \hat{E})\dot{\varepsilon}(t) + \frac{\hat{E}E}{\eta}\varepsilon(t). \tag{5.30}$$

This ODE can be solved, see (Hartmann, 2012), to obtain

$$\sigma(\varepsilon) = \eta\dot{\varepsilon}\left(1 - e^{-\hat{E}/(\eta\dot{\varepsilon})\varepsilon}\right) + E\varepsilon. \tag{5.31}$$

The three parameters $E = 10\text{MPa}$, $\hat{E} = 100\text{MPa}$ and $\eta = 100\text{MPa}\,\text{s}$ are assumed and strain-controlled synthetic data are created using three different strain rates $\dot{\varepsilon} = 0.005, 0.01, 0.015\text{s}^{-1}$ (100 data points per strain rate), see Fig. 5.12. In order to study the different aspects of the identification process, the exact synthetic data is then perturbed. Since, it is a simple 1D problem, the entire process is solved analytically.

Initially, it is assumed that $E$ is known and thereby fixed. The parameters $\hat{E}$ and $\eta$ are re-identified. The sensitivities $\partial\sigma/\partial\hat{E}$ and $\partial\sigma/\partial\eta$ can be derived easily and read,

$$\begin{aligned} \frac{\partial\sigma}{\partial\hat{E}} &= \varepsilon e^{\frac{\hat{E}\varepsilon}{K\eta}} \\ \frac{\partial\sigma}{\partial\eta} &= -\dot{\varepsilon}\left(e^{\frac{\hat{E}\varepsilon}{K\eta}} - 1\right) - \frac{\hat{E}\varepsilon e^{\frac{\hat{E}\varepsilon}{K\eta}}}{\eta} \end{aligned} \tag{5.32}$$

Assuming initial guess of $\hat{E} = 1\text{MPa}$ and $\eta = 1\text{MPa}\,\text{s}$, the re-identified parameters are $\hat{E} = 99.49 \pm 1.51\text{MPa}$ and $\eta = 99.68 \pm 0.37\text{MPa}\,\text{s}$. With $\det \boldsymbol{H} \approx 2.05 \times 10^{-5}$, a non-vanishing determinant of the Hessian, identifiability is guaranteed. A correlation coefficient of $C_{12} = -0.437$ is moderate with a very high coefficient of determination of $R^2 \approx 0.99$ showing a very good reliability of identification of these parameters.

The identification of parameters $\hat{E}$ and $\eta$ by fixing $E$ begs the question of whether all the three material parameters can be identified in parallel at the same time. For this, all the parameters are assumed to be unity and parameters are re-identified. The re-identified parameter values read $E = 10.04 \pm 0.12\text{MPa}$, $\hat{E} = 99.72 \pm 1.64\text{MPa}$ and $\eta = 99.4 \pm 0.83\text{MPa}\,\text{s}$. $\det \boldsymbol{H} \approx 3.12 \times 10^{-6}$ represents the local identifiabilty of the parameters. The coefficient of determination of $R^2 \approx 0.99$ is also rather high showing a good fit. The correlation coefficient matrix reads,

$$\boldsymbol{C} = \begin{bmatrix} 1 & 0.36 & -0.91 \\ 0.36 & 1 & -0.5 \\ -0.91 & -0.5 & 1 \end{bmatrix}.$$

Thus all the three material parameters can be identified in parallel with appropriate quality.

## 5.1.6. Basic Problems in Large Strain Analysis

In this section, the investigation is extended to large strains and thus analytical solutions aren't available. Thus, finite element method, explained in Chapter 3 is used to solve inhomogeneous boundary-value problems similarly to Section 5.1.3. Furthermore, constitutive equations for large strain theory is taken into consideration. The basic NLS problem, identified using small-strain experiments, can be transferred to large strain problems as well. However, different experiments are used to identify the parameters in the following examples. One common experiment is the indentation experiment using a hard indenter that presses on a weaker material to obtain the material parameters. This is investigated in the following section for single and double layered specimens.

### 5.1.6.1. Indentation Tests

The method of pressing a hard "indenter" onto a weaker material is chosen normally to determine the hardness of the material. It can also be used to characterize the material behavior, see (Huber and Tsakmakis, 1999a,b; Lee et al., 2005; Gibmeier et al., 2005; Rauchs et al., 2010; Chen and Diebels, 2014). The identifiability of the material parameters is of particular interest. Since the problem is large strains following the application of the indenter, a large-strain, compressible, isotropic Neo-Hookean model is chosen (For the basic in continuum mechanics, see Chapter 2). It is better to have the same decomposition in the elasticity relation (volumetric strains $\varepsilon_v = \operatorname{tr} \mathbf{E}$ and deviatoric strains $\mathbf{E}^D$). The deformation gradient is decomposed into volume-preserving and volume-changing parts as shown in Eq.(2.19). This implies the strain-energy function

$$\psi(J, \mathrm{I}_{\overline{\mathbf{C}}}, \mathrm{II}_{\overline{\mathbf{C}}}) = U(J) + w(\mathrm{I}_{\overline{\mathbf{C}}}, \mathrm{II}_{\overline{\mathbf{C}}}) \tag{5.33}$$

with $J = \det \mathbf{F}$, and the invariants $\mathrm{I}_{\overline{\mathbf{C}}} = \operatorname{tr} \overline{\mathbf{C}}$ and $\mathrm{II}_{\overline{\mathbf{C}}} = 1/2(\mathrm{I}^2_{\overline{\mathbf{C}}} - \operatorname{tr} \overline{\mathbf{C}}^2)$ of the unimodular right Cauchy-Green tensor $\overline{\mathbf{C}} = (\det \mathbf{C})^{-1/3}\mathbf{C}$. For convenience, the commercial finite element program Abaqus ® is chosen where

$$U(J) = K/2(J-1)^2 \quad \text{and} \quad w(\mathrm{I}_{\overline{\mathbf{C}}}) = \frac{G}{2}(\mathrm{I}_{\overline{\mathbf{C}}} - 3). \tag{5.34}$$

The resulting Cauchy-stress state reads

$$\mathbf{T} = K(J-1)\mathbf{I} + \frac{G}{J}\overline{\mathbf{B}}^D \tag{5.35}$$

where the unimodular left Cauchy-Green tensor $\overline{\mathbf{B}} = (\det \mathbf{B})^{-1/3}\mathbf{B}$, $\mathbf{B} = \mathbf{F}\mathbf{F}^{\mathrm{T}}$. In the case of small strains, the linearized constitutive model (5.35) leads to Eq.(5.1).

### 5.1.6.2. One-layer Application

The goal is to identify the bulk modulus $K$ and shear modulus $G$ from a displacement-controlled process from Eq.(5.35). $u_{\mathrm{I}} = 0.35\,\mathrm{mm}$ is the indentation depth, see the sketch in Fig. 5.13(a) for the geometrical dimensions. For simplicity, the specimen is assumed to be axisymmetric, and the

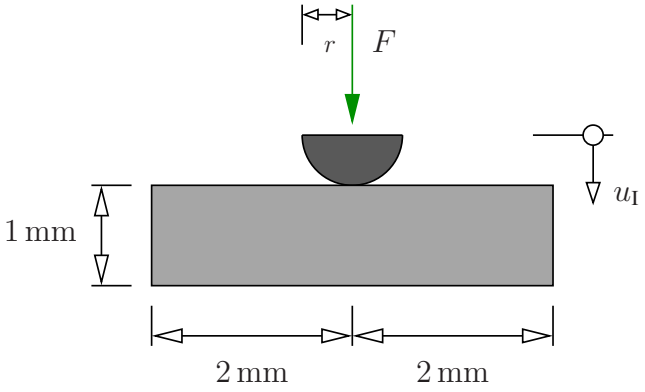


(a) Geometry

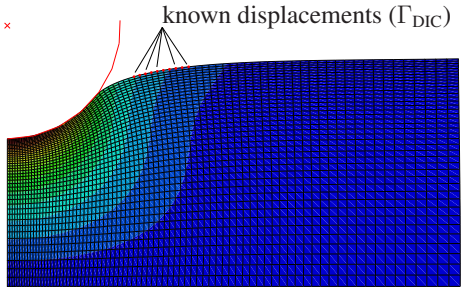


(b) Mesh and result of finite element solution

Figure 5.13.: Geometry and simulation result of indentation test (indenter radius $r = 0.5\,\mathrm{mm}$, indentation depth $u_{\mathrm{I}} = 0.35\,\mathrm{mm}$), see (Hartmann and Gilbert, 2018)

indenter is given as a rigid spherical indenter with the radius $r = 0.5\,\mathrm{mm}$. The element type used is CAX4R (4-noded bilinear quadrilateral elements) with reduced integration and a total number of 3321 nodes as shown in the Fig. 5.13(b). Surface-to-surface contact is chosen in connection with a node-to-surface contact discretization method. A tangential frictional coefficient of $0.4$ is assumed for the contact problem.

**Re-identification using exact force data** If the indenter is indented onto a single layer material with $K = 3\,\mathrm{MPa}$ and $G = 1.5\,\mathrm{MPa}$, a number of data points are generated at certain time-steps by the automatic load control of Abaqus. The force-indentation depth information $F/u_\mathrm{I}$ obtained from the Abaqus simulation is given as the experimental data to re-identify the material parameters. The determinant of the Hessian is calculated numerically following the Eq.(4.33) resulting in $\det \boldsymbol{H} \approx 1.56$. This implies a unique solution and as expected, the parameters were re-identified with four digits accuracy with a perfect fit of $R^2 = 1$. Therefore, indentation test seems to be a reliable experiment for identifying $K$ and $G$.

**Re-identification using perturbed force data** Now, the force data is perturbed with a standard deviation of $3\%$, see Fig. 5.14(a), and the material parameters are re-identified. For

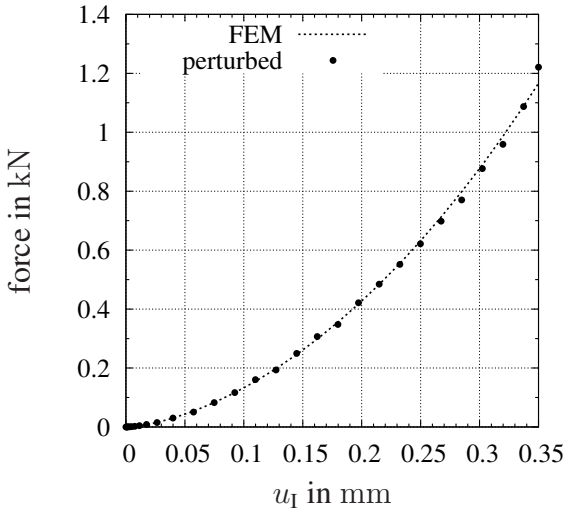


(a) Force/displacement behavior and perturbed data, see (Hartmann and Gilbert, 2018)

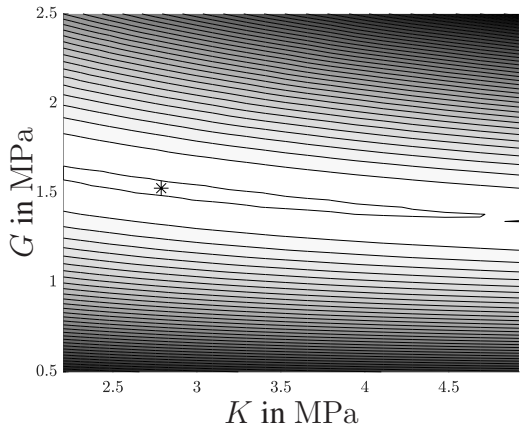


(b) Goal function behavior for indentation test with "measured perturbed" force

Figure 5.14.: Perturbed force for indentation test and contour plot of $f(K, G)$

an initial guess of $K^{(0)} = 7.5\,\mathrm{MPa}$ and $G^{(0)} = 0.9\,\mathrm{MPa}$, the result of identification is $K = 2.12 \pm 0.21\mathrm{MPa}$ and $G = 1.63 \pm 0.04\mathrm{MPa}$ (instead of the expected parameters $K = 3\,\mathrm{MPa}$ and $G = 1.5\,\mathrm{MPa}$). It was also found out that the material parameters are highly correlated with a correlation coefficient of $C_{12} = 0.995$. If the goal function $f(K, G)$ distribution plot is created, see Fig. 5.14(b), by varying the material parameters $K$ and $G$ it can be seen that the minimum is located in a very narrow, elongated valley. Since the valley is almost parallel to the $K$-axis, the confidence interval is also larger for $K$ than for $G$. Thus it can be concluded that the estimation of $K$ is more uncertain.

**Perturbed data and surface deformation** Along with the reaction force $F$, it is assumed that full-field data is also available in a small region $\Gamma_\mathrm{DIC}$ close to the indenter, see Fig. 5.13(b), to measure the radial and axial displacement. This implies that in addition to the force/indentation

depth curve, more information is available for re-identification. The displacement on $\Gamma_{\text{DIC}}$ as well as the reaction forces $F$ are perturbed with a standard deviation of $3\%$ and used to identify the material parameters (29 load steps). Here, the Jacobian is computed numerically using Eq.(4.33) as in the previous example. The resulting Hessian and its determinant of the re-identification are

$$\boldsymbol{H} = \begin{bmatrix} 49.81 & -12.24 \\ -12.24 & 3.21 \end{bmatrix}, \quad \text{and} \quad \det \boldsymbol{H} = 9.856 \tag{5.36}$$

indicating that identifiability is guaranteed at this point. Even though the identification is unique, the correlation between the material parameters is again extremely high,

$$\boldsymbol{C} = \begin{bmatrix} 1 & 0.9687 \\ 0.9687 & 1 \end{bmatrix}. \tag{5.37}$$

Thus, the incorporation of another information, as shown in this example, improves the confidence interval of the material parameters, $K = 2.79 \pm 1.8 \times 10^{-2}$ MPa and $G = 1.52 \pm 4.5 \times 10^{-3}$ MPa with $s^2 = 1 \times 10^{-5}$. However, the correlation between the parameters are not improved.

#### 5.1.6.3. Two-layer Application

Based on the results obtained from the single-layer example in Section 5.1.6.2, obtaining the parameters for two-layered material can be thought to be identifiable. In this example, soft materials, like arteries, it is assumed that the surface deformations are large enough to be detectable by a DIC-system. Fig. 5.15(a) shows the three-dimensional discretization, which yields much

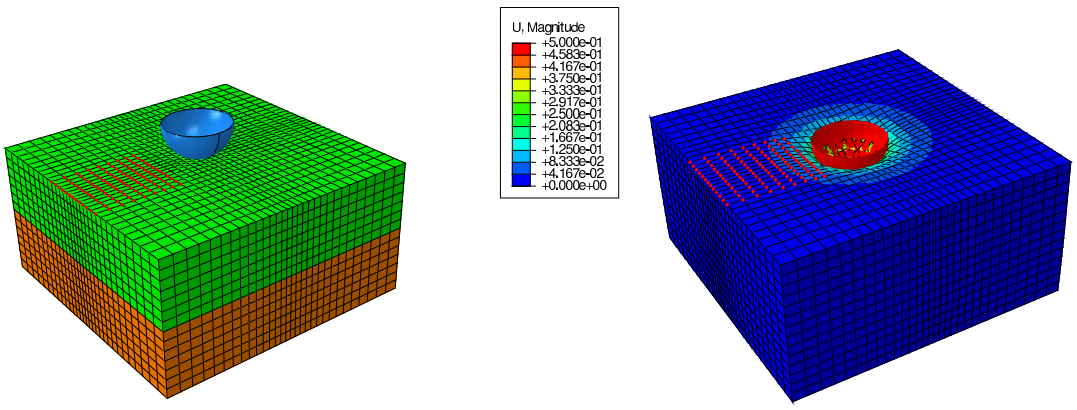


(a) Layer distribution and mesh

(b) Maximum displacement distribution

Figure 5.15.: Geometry, mesh and displacement of three-dimensional two-layered plate under indentation, see (Hartmann and Gilbert, 2018)

more information than the axisymmetric consideration of Section 5.1.6.1. Here, the block is

$4\,\mathrm{mm} \times 4\,\mathrm{mm}$ with a height of $2 \times 1\,\mathrm{mm}$. A typical displacement is shown in Fig. 5.15(b). The element type used is C3D8 (8-noded brick elements). Two tests are carried out: first, the displacement-controlled indentation is performed on layer 1 and thereafter on layer 2 ($u_\mathrm{I} = 0.5\,\mathrm{mm}$). Furthermore, a larger amount of indentation than in Section 5.1.6.1 is chosen to initiate larger deformations at the surface. Again, the force data and surface displacements are generated, perturbed and afterwards provided for re-identification. Naturally, since there are force and surface displacement data, the residuum needs to be weighted. Here, the material parameters $K^{(1)} = 3\,\mathrm{MPa}$, $G^{(1)} = 1.5\,\mathrm{MPa}$, $K^{(2)} = 6\,\mathrm{MPa}$ and $G^{(2)} = 3\,\mathrm{MPa}$ are used to generate the experimental data. The result of identification is $K^{(1)}_\mathrm{res} = 2.91 \pm 0.05$ MPa, $G^{(1)}_\mathrm{res} = 1.52 \pm 0.0076$ MPa, $K^{(2)}_\mathrm{res} = 5.98 \pm 0.1$ MPa, and $G^{(2)}_\mathrm{res} = 3.04 \pm 0.0097$ MPa. Additionally, a very good fit $R^2 = 0.999$ was obtained with a non-vanishing determinant of the Hessian, $\det \boldsymbol{H} = 0.803$ and a correlation matrix, for a variance of $s^2 = 0.0001$

$$\boldsymbol{C} = \begin{bmatrix} 1 & 0.64 & -0.23 & -0.21 \\ & 1 & -0.05 & -0.59 \\ & & 1 & 0.25 \\ & & & 1 \end{bmatrix}.$$

The correlation is moderate, showing that this test seems to produce reliable elastic material parameters of a Neo-Hookean-type model. However, for more complex material models (plasticity, viscoplasticity, anisotropy etc.) this statement may not be valid since the number of material parameters is higher and additional investigations are required. This test can be combined with other tests, like uniaxial tension, biaxial etc., for such complicated models.

#### 5.1.6.4. Bending

As a final example to investigate identifiability, the possibility to use bending tests is explored. For this purpose, a two layered specimen is modeled in Abaqus. Here, each layer is $20\,\mathrm{mm} \times 100\,\mathrm{mm}$ with a thickness of $2.5\,\mathrm{mm}$. The element type used is C3D20 (20-noded quadratic brick elements). A Neo-Hooke model according to Eq.(5.35) is assumed for each layer with the material parameters $K^{(t)} = 400\,\mathrm{MPa}$, $G^{(t)} = 200\,\mathrm{MPa}$, $K^{(b)} = 200\,\mathrm{MPa}$ and $G^{(b)} = 100\,\mathrm{MPa}$, where $t$ represents top layer while $b$ represents bottom layer. It as also assumed that DIC information is available, see the area marked red in Fig. 5.16(a). Synthetic data are created using the material parameters. The experiment data vector is compiled of force data from the indentor as well as the maximum principal strain distribution, see Fig. 5.16(b). In order to determine the quality measures, the data are perturbed and the residuum vector is weighted appropriately. The re-identification is carried out. It was found out that the material parameters can be uniquely identified. The result of identification is $K^{(1)}_\mathrm{res} = 401.23 \pm 1$ MPa, $G^{(1)}_\mathrm{res} = 199.45 \pm 2$ MPa, $K^{(2)}_\mathrm{res} = 200.78 \pm 1$ MPa, and $G^{(2)}_\mathrm{res} = 99.67 \pm 2$ MPa. Additionally, a very good fit $R^2 = 0.997$ was obtained with a non-vanishing $\xi_p = 0.224$ and a correlation matrix, for a variance of

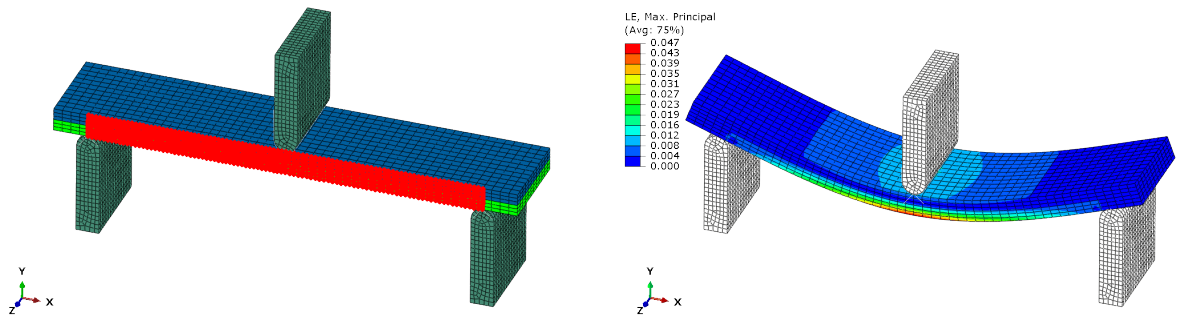


(a) Layer distribution and mesh (b) Maximum principal strain distribution

Figure 5.16.: Geometry, mesh and maximum principal strain of three-dimensional two-layered plate under bending

$s^2 = 0.00001$

$$\boldsymbol{C} = \begin{bmatrix} 1 & 0.52 & -0.11 & -0.34 \\ & 1 & -0.17 & -0.68 \\ & & 1 & 0.48 \\ & & & 1 \end{bmatrix}.$$

The correlation is once again moderate showing that bending tests also produce reliable elastic material parameters for a Neo-Hookean-type model.

From all these investigations done with regards to identifiability, it must be concluded that before performing experiments to identify material parameters, it is essential to re-identify the material parameters using synthetic data to ensure the identifiability of the material parameters.

## 5.1.7. Comparison between IND and END

Once the investigation on identifiability is completed, it is essential to investigate the computational cost between IND and END. In the following cases, at first, an example of a case for a material model without any internal variables are investigated. The computational cost between END and IND are compared. Following that, a small strain non-linear viscoelastic case is investigated. These examples will provide a better understanding of the advantages and disadvantages of IND and END.

### 5.1.7.1. Biaxial Tension

In this example, a quarter of the specimen according to (Hartmann et al., 2018a), see Fig. 5.17(a) is modeled and using the boundary conditions shown in Fig. 5.17(b). A simple neo-Hooke model described in the Section 5.1.6.1 is assumed with the parameters $K = 1600\,\mathrm{MPa}$ and $G = 275\,\mathrm{MPa}$. It is also assumed that DIC is available, see the red area marked in Fig. 5.17(a). A total number of 40 load steps are assumed to be available. The model is meshed using quadratic elements with a total number of 8200 elements. The synthetic data created can be

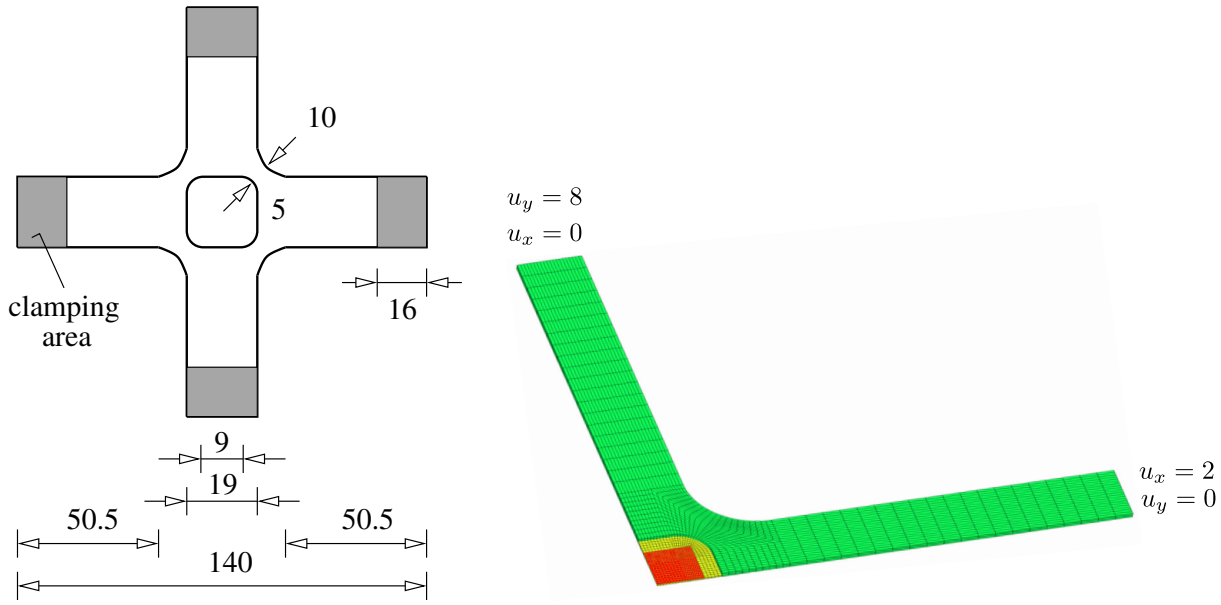


(a) Geometry of the specimen, see (Hartmann et al., 2018a)

(b) Mesh of the specimen

Figure 5.17.: Geometry and Mesh of a biaxial specimen (measures in $\mathrm{mm}$)

seen in Fig. 5.18. Since both reaction forces and displacements are used to re-identify the parameters, it is essential to weigh the residuals. In order to compare between END and IND, it is essential to provide certain quantities as described in Section 4.4.3.1, see Eq.(4.46). Acegen is used to develop FORTRAN code which is fed to the FEM program TASAFEM to determine the sensitivities. Now that the problem is setup, the re-identification process is carried out using both IND and END. The number of FEM calls in the case of END is 24 whereas in the case of IND is 8. The total number of time taken to complete the identification process in the case of END is approximately 1700 seconds whereas the time taken to complete in the case of IND is approximately 800 seconds. This implies that more than $50\%$ of the time can be spared when using IND instead of END.

#### 5.1.7.2. 3D Small Strain Non-Linear Viscoelasticity

In this example, a small strain non-linear viscoelastic model for a 3D case is investigated using a dog-bone specimen. Similar to the 1D case, the total strain $\mathbf{E}$ can be divided into elastic strain $\mathbf{E}_e$ and viscous strain $\mathbf{E}_v$.

$$\mathbf{E} = \mathbf{E}_e + \mathbf{E}_v. \tag{5.38}$$

The stress can be divided into the equilibrium part $\mathbf{T}_{\text{eq}}$ and the overstress part $\mathbf{T}_{\text{ov}}$,

$$\mathbf{T} = \mathbf{T}_{\text{eq}} + \mathbf{T}_{\text{ov}} \tag{5.39}$$

where

$$\mathbf{T}_{\text{eq}} = K(\text{tr}\mathbf{E})\mathbf{I} + 2G\mathbf{E}^D \tag{5.40}$$

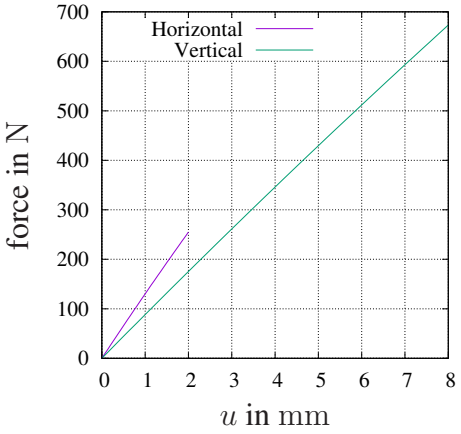


Figure 5.18.: Synthetic experimental data

is the equilibrium stress part and

$$\mathbf{T}_{\text{ov}} = \mathbf{T}^D_{\text{ov}} = 2\hat{G}(\mathbf{E} - \mathbf{E}^D_v) \tag{5.41}$$

is the overstress part. Combining the equations 5.40 and 5.41,

$$\mathbf{T} = K(\text{tr}\mathbf{E})\mathbf{I} + 2G\mathbf{E}^D + 2\hat{G}(\mathbf{E} - \mathbf{E}^D_v) \tag{5.42}$$

with

$$\dot{\mathbf{E}}_v = \frac{2\hat{G}}{\eta}(\mathbf{E} - \mathbf{E}^D_v) \tag{5.43}$$

and

$$\eta = \eta_0 e^{-s_0||\mathbf{T}^D_{\text{ov}}||}. \tag{5.44}$$

The model is implemented in TASAFEM. A dog-bone type specimen is assumed and meshed (1200 elements), see Fig. 5.19(a). It is assumed that DIC information is available, see the red area in the Fig. 5.19(a). Once it is modeled, for the material parameters $K = 1667\text{MPa}$, $G = 8.75\text{MPa}$, $\hat{G} = 150\text{MPa}$, $\eta_0 = 13\text{MPa}\,\text{s}$ and $s_0 = 1.1\text{MPa}^{-1}$ synthetic data is created, see Fig. 5.19(b). The parameters $K$ and $G$ are fixed and the other parameters are re-identified. The $\xi_p = 0.0016$ indicating local unique identifiability of the problem. Since there are forces and displacements in the experimental vector, the residuum is appropriately weighted. The re-identification process is carried out with the help of time-adaptive scheme (experimental data is interpolated to simulated data because the sensitivities cannot be interpolated) and the results are analyzed. It was found out that for END, the FEM code was called 36 times meanwhile for IND, the FEM code was called only 9 times. The total time consumed for END is approximately 2500 seconds whereas the total time consumed for IND is approximately 1600 seconds. This shows that the IND is computationally more efficient than END.

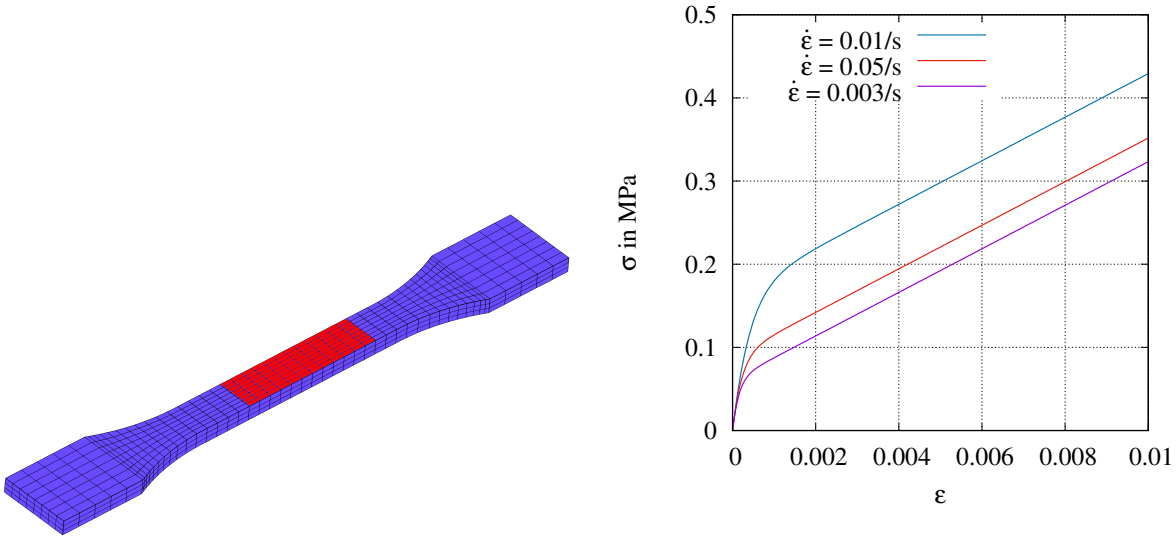


(a) 3D mesh

(b) Synthetic data used in re-identification

Figure 5.19.: 3D small strain viscoelastic example

## 5.2. Real Example

As an example to understand the concepts of material parameter identification and to compare IND and END for complicated models, biaxial experiments are performed on rubber specimen. This example will address all the different concepts introduced in this research work, see also (Hartmann and Gilbert, 2021).

### 5.2.1. Experimental Data

Experiments were carried out on a biaxial testing machine, see (Hartmann et al., 2018a) for more detailed analysis regarding the biaxial tests. Carbon black-filled natural rubber, cured at $140\,^{\circ}\mathrm{C}$ for $36\,\mathrm{min}$ according to (Bellec, 2018), was chosen. Bellec (2018) performed repeatability tests on the specimens and determined that the results are reproducible. Thus, it was not essential to repeat the experiments. Mullins effects are also ignored in this example. The problems regarding the usage of equibiaxial tests have been previously discussed in Section 5.1.3. Thus, only non-equibiaxial tests have been carried out. In Fig. 5.20(a), the testing device is shown. In Figs. 5.20(b) and 5.20(c) typical strain distributions in horizontal and vertical directions as determined by a digital image correlation (DIC) system is shown. The 3D-DIC system ARAMIS developed by the company GOM, Brunswick, Germany is being used to obtain the full-field data, see (GOM, 2009).

The rigid body motions due to the testing machines affect the identification process adversely and thus needs to be removed completely. If displacements are used from the DIC systems,

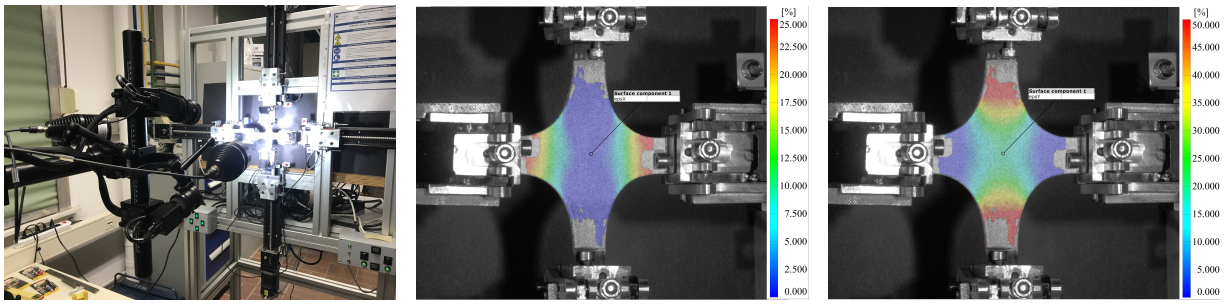


(a) Biaxial testing machine (b) Horizontal strain field (c) Vertical strain field

Figure 5.20.: Experimental setup and typical strain distributions in horizontal and vertical directions, see (Hartmann and Gilbert, 2021)

the rigid body motions cannot be accounted for in the calculations. The elimination of rigid body motion from the experimental data is a challenging process. Especially, in the case of biaxial tests, the rigid body motions cannot be accounted for by the testing machine or the full-field data. The easiest method to circumvent this drawback is to use a strain measure instead of displacement. Thus, maximum principal strains are determined using the displacement data obtained from the system. The determination of principal strains (stretches) is based on the concept proposed in (Hartmann and Rodriguez, 2018). It is advantageous to use this method since the coordinates of the points in the Euclidean space can be obtained from the DIC-systems. In the following experiments, the clamp displacements are prescribed and the resulting forces are measured at the two clamps in horizontal and vertical directions as can be seen in the Fig. 5.20(a). The shape of the specimen was based on studies shown in (Hartmann et al., 2018a; Seibert et al., 2014) and are shown in Fig.5.21. Two plates are machined out according to Fig.5.21. The rubber sheet of dimension $118 \times 118\mathrm{mm}$ are then placed between the plates and then the shape of the specimen is cut out from the sheet. The bulge is for a better fixation in the clamps and helps from the specimen not slipping during loading.

Rubber specimens are usually modeled using hyperelasticity or an overstress-type viscoelasticity. In this research work, a model of overstress-type viscoelasticity is assumed to represent the behavior of the rubber specimen*. Thus, different loading paths are required to identify the material parameters in the equilibrium stress and overstress state. For the identification of material parameters, four monotonous rate-dependent paths along with a multi-step relaxation tests are carried out. In order to identify the material parameters of the equilibrium stress state, the termination points of the multi-step relaxation process is taken into consideration, see for discussion (Haupt and Sedlan, 2001). Monotonous rate-dependent loading paths, see Fig. 5.22(a), and a multi-step relaxation path, see Fig. 5.22(b), are prescribed. In order to ensure better identifiability of the material parameters, in one direction (vertical), a displacement four times larger than in the other direction (horizontal) is prescribed, see discussion in (Hartmann et al., 2018a). The displacement rates of the clamps are set at $\dot{u}(t) = 0.004, 0.01, 0.1, 1\mathrm{mm\,s^{-1}}$ in the hori-

*See Chapter 1 for a detailed literature review on the different types of constitutive models used for rubber

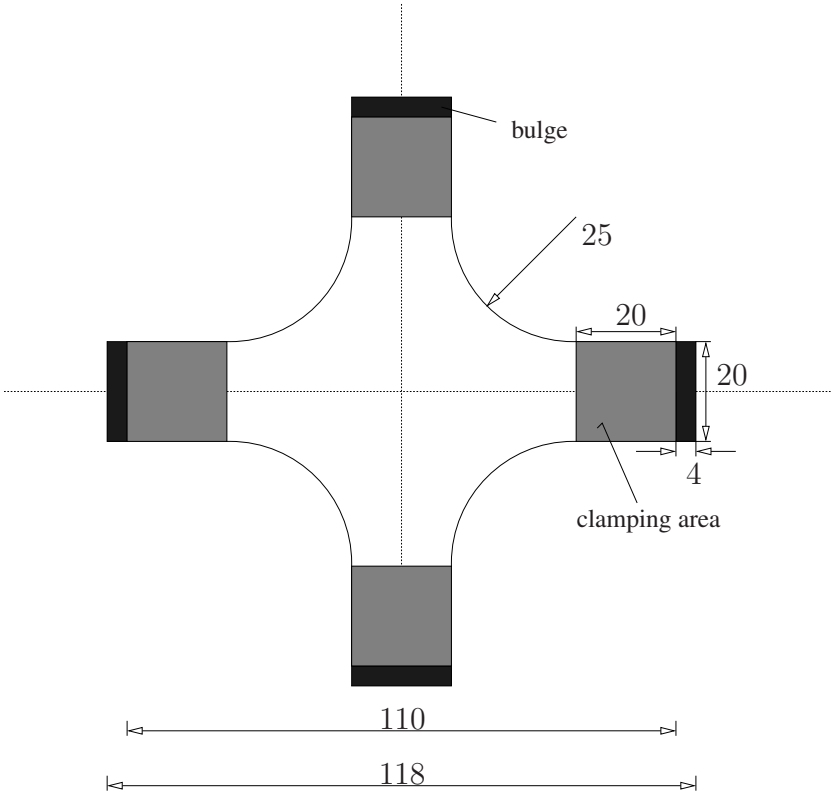


Figure 5.21.: Geometry of the cruciform-like specimen with a thickness of $6\,\mathrm{mm}$ (all dimensions in $\mathrm{mm}$, see (Hartmann and Gilbert, 2021))

zontal direction. Rates slower than $0.004\,\mathrm{mm\,s^{-1}}$ and higher than $1\,\mathrm{mm\,s^{-1}}$ were not possible owing to the technical limitation of the testing machine. For the multi-step relaxation tests, for loading, the displacement rate was set at $0.01\mathrm{mm\,s^{-1}}$ with a subsequent holding time of $6\,\mathrm{h}$. The force-displacement (displacements of the clamps) results are shown in Fig. 5.27 together with the calibrated model.

## 5.2.2. Material Model

Based on the basics introduced in the Chapter 2, the constitutive relation assumed for the rubber specimen is discussed in this section. Following the balance of linear momentum (quasi-static case) along with the stress-strain relation and the evolution equations for the internal variables,

$$\begin{aligned} \widetilde{\mathbf{T}}(\vec{X},t) &= \widetilde{\mathbf{h}}(\mathbf{C}(\vec{X},t),\mathbf{q}(\vec{X},t)) \\ \dot{\mathbf{q}}(\vec{X},t) &= \widetilde{\mathbf{r}}(\mathbf{C}(\vec{X},t),\mathbf{q}(\vec{X},t)) \end{aligned} \tag{5.45}$$

the stress measures are introduced. As previously mentioned, in this research work, the rubber specimens are characterized by a model of finite strain viscoelasticity, see (Lion, 1997; Haupt and Sedlan, 2001; Reese and Govindjee, 1998; Hartmann, 2002), with certain modifications to suit

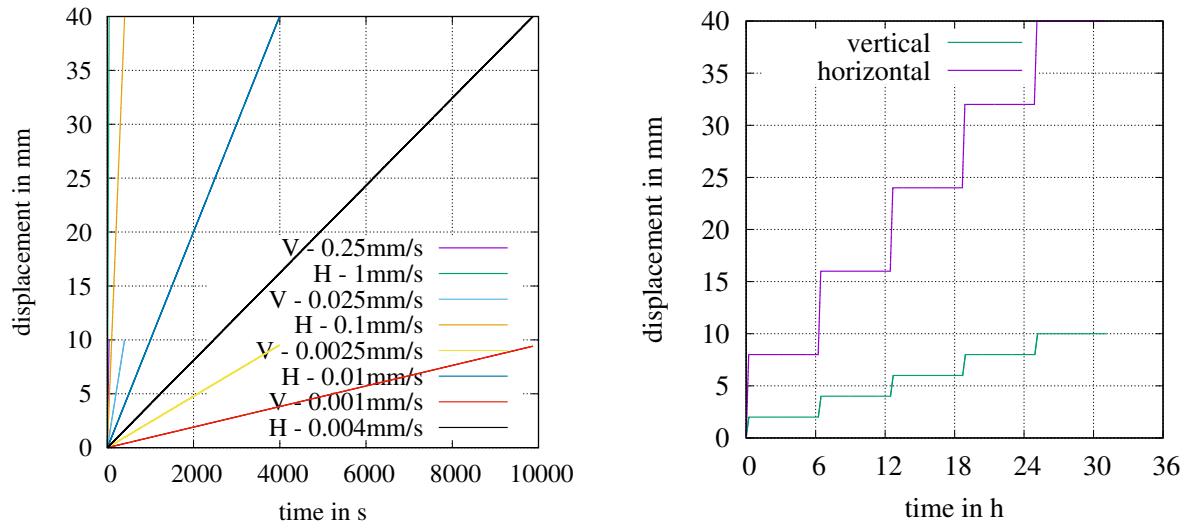


(a) Displacement loading paths with different rates

(b) Multi-step loading paths

Figure 5.22.: Displacement loading paths in the biaxial tensile testing machine, see (Hartmann and Gilbert, 2021)

the particular case. Eqs.$(5.45)_{1,2}$ depend on internal variables $\mathbf{q} \in \mathbb{R}^{n_q}$, which might be scalar- or tensor-valued. For this model, the vector of internal variables $\mathbf{q}$ is assumed to be components of the (symmetric) viscous right Cauchy-Green tensor $\mathbf{q} \leftarrow \mathbf{C}_v$ with $n_q = 6$. The starting vector for the internal variables is given by $\mathbf{q}_0 = \{1, 1, 1, 0, 0, 0\}$. $\mathbf{C}_v = \mathbf{F}_v^T \mathbf{F}_v$ is derived from the multiplicative decomposition of the deformation gradient into an elastic and a viscous part, $\mathbf{F} = \mathbf{F}_e \mathbf{F}_v$. The second Piola-Kirchhoff tensor decomposes into three parts

$$\tilde{\mathbf{T}} = J\rho_R U'(J)\mathbf{C}^{-1} + \tilde{\mathbf{T}}_{eq}^{iso} + \tilde{\mathbf{T}}_{ov}, \quad \text{with} \quad U'(J) = \frac{K}{10}(J^4 - J^{-6}). \tag{5.46}$$

The first part depends on the volumetric deformation, the second part is the isochoric representation (equilibrium stress state) and the last term defines the overstress part. The specific strain energy function according to neo-Hooke model, $U(J) = K/2(J-1)^2$ exhibits non-physical behavior under tension, see discussion in (Ehlers and Eipper, 1998; Hartmann and Neff, 2003). Thus, the strain energy function $U(J) = K/50(J^5 + J^{-5} - 2)$ is chosen. The equilibrium stress part which depends on the isochoric deformation reads

$$\tilde{\mathbf{T}}_{eq}^{iso} = \varphi_1 \mathbf{I} + \varphi_2 \overline{\mathbf{C}} + \varphi_3 \overline{\mathbf{C}}^{-1} \tag{5.47}$$

where

$$\varphi_1 = \frac{2\rho_R}{(\det \overline{\mathbf{C}})^{1/3}}(w_1 + w_2 \mathrm{I}_{\overline{\mathbf{C}}}), \quad \varphi_2 = -\frac{2\rho_R}{(\det \overline{\mathbf{C}})^{1/3}} w_2, \quad \varphi_3 = -\frac{2\rho_R}{3(\det \overline{\mathbf{C}})^{1/3}}(w_1 \mathrm{I}_{\overline{\mathbf{C}}} + 2w_2 \mathrm{II}_{\overline{\mathbf{C}}}) \tag{5.48}$$

and

$$w_1 = \frac{\partial w_{\text{eq}}}{\partial \mathrm{I}_{\overline{\mathbf{C}}}} = c_{10}, \quad w_2 = \frac{\partial w_{\text{eq}}}{\partial \mathrm{II}_{\overline{\mathbf{C}}}} = c_{01}\frac{3}{2}\mathrm{II}_{\overline{\mathbf{C}}}^{1/2} \tag{5.49}$$

for

$$w_{\text{eq}}(\mathrm{I}_{\overline{\mathbf{C}}}, \mathrm{II}_{\overline{\mathbf{C}}}) = c_{10}(\mathrm{I}_{\overline{\mathbf{C}}} - 3) + c_{01}(\mathrm{II}_{\overline{\mathbf{C}}}^{3/2} - 3\sqrt{3}). \tag{5.50}$$

This is suppositionally an extension of the Mooney-Rivlin model to polyconvexity, see discussions regarding polyconvexity in (Hartmann and Neff, 2003; Balzani et al., 2006). $\overline{\mathbf{C}} = \overline{\mathbf{F}}^T\overline{\mathbf{F}}$ represents the unimodular right Cauchy-Green tensor depending on $\overline{\mathbf{F}} = (\det \mathbf{F})^{-1/3}\mathbf{F}$ with $\det \overline{\mathbf{F}} = 1$.

The overstress part, see (Hartmann, 2002, 2003), is given by

$$\tilde{\mathbf{T}}_{\text{ov}} = 2\rho_{\text{R}}\mu_0 \frac{(\det \mathbf{C}_{\text{v}})^{1/3}}{(\det \mathbf{C})^{1/3}} \left(\mathbf{C}_{\text{v}}^{-1} - \frac{1}{3}(\mathbf{C}\cdot\mathbf{C}_{\text{v}}^{-1})\mathbf{C}^{-1}\right) \tag{5.51}$$

depending on the evolving viscous right Cauchy-Green tensor

$$\dot{\mathbf{C}}_{\text{v}} = \frac{4\rho_{\text{R}}\mu_0}{\eta} \frac{(\det \mathbf{C}_{\text{v}})^{1/3}}{(\det \mathbf{C})^{1/3}} \left(\mathbf{C} - \frac{1}{3}(\mathbf{C}\cdot\mathbf{C}_{\text{v}}^{-1})\mathbf{C}_{\text{v}}\right). \tag{5.52}$$

The rate dependence is characterized by a process-dependent viscosity

$$\eta = \eta_0 e^{\left(-s_0\sqrt{\mathbf{C}\mathbf{T}_{\text{ov}}\cdot\mathbf{T}_{\text{ov}}\mathbf{C}}\right)}. \tag{5.53}$$

In certain cases, the same function can also be expressed in dependence of the Green-strain tensor $\mathbf{E} = (\mathbf{C} - \mathbf{I})/2$. However, this does not affect the principal equations. For consistent tangents of the material model, the reader is referred to Hartmann (2002). The material model used in this example is summarized in Tab.5.1.

In this model, six material parameters are defined, which are determined step-wise. The step-wise identification enables the optimizer to find the local minimum for elastic and viscous part. If all the parameters are identified at the same time, then the parameters cannot be identified. At first, the equilibrium parameters, $\boldsymbol{\kappa}_{\text{eq}}^T = \{K, c_{10}, c_{01}\}$ characterizing the equilibrium stress state is identified using the relaxation termination points. This is followed by the identification of the parameters, $\boldsymbol{\kappa}_{\text{ov}}^T = \{\mu_0, \eta_0, s_0\}$ characterizing the overstress behavior, are identified using the monotonous rate-dependent loading along with the multi-step relaxation data.The common procedure to connect the density $\rho_{\text{R}}$ with the material parameters $K \leftarrow K\rho_{\text{R}}$, $c_{10} \leftarrow c_{10}\rho_{\text{R}}$, $c_{01} \leftarrow c_{01}\rho_{\text{R}}$, and $\mu_0 \leftarrow \mu_0\rho_{\text{R}}$ is also applied here. Obviously, Eq.(5.46) represents the concrete formulation of Eq.$(5.45)_2$, and Eq.(5.52) the evolution equation $(5.45)_3$.

## 5.2.3. Determination of Strain using DIC

The specimen is firstly spray-painted with white paint and then points were made by application of black paint (the area under consideration is shown in orange in Fig. 5.21). These points are then tracked in real time by the DIC-system. Since these are biaxial testing specimens, triple

Table 5.1.: Material model expressed in reference configuration

(1) $2^{\text{nd}}$ **Piola-Kirchhoff stress tensor**

$$\tilde{\mathbf{T}} = J\rho_{\text{R}}U'(J)\mathbf{C}^{-1} + \tilde{\mathbf{T}}^{\text{iso}}_{\text{eq}} + \tilde{\mathbf{T}}_{\text{ov}} \tag{5.54}$$

$$U'(J) = \frac{K}{10}(J^4 - J^{-6}) \tag{5.55}$$

(2) **Equilibrium stress**

$$\tilde{\mathbf{T}}^{\text{iso}}_{\text{eq}} = \varphi_1\mathbf{I} + \varphi_2\overline{\mathbf{C}} + \varphi_3\overline{\mathbf{C}}^{-1} \tag{5.56}$$

$$\varphi_1 = \frac{2\rho_{\text{R}}}{(\det\overline{\mathbf{C}})^{1/3}}(w_1 + w_2\mathrm{I}_{\overline{\mathbf{C}}}) \tag{5.57}$$

$$\varphi_2 = -\frac{2\rho_{\text{R}}}{(\det\overline{\mathbf{C}})^{1/3}}w_2 \tag{5.58}$$

$$\varphi_3 = -\frac{2\rho_{\text{R}}}{3(\det\overline{\mathbf{C}})^{1/3}}(w_1\mathrm{I}_{\overline{\mathbf{C}}} + 2w_2\mathrm{II}_{\overline{\mathbf{C}}}) \tag{5.59}$$

$$w_1 = \frac{\partial w_{\text{eq}}}{\partial \mathrm{I}_{\overline{\mathbf{C}}}} = c_{10} \tag{5.60}$$

$$w_2 = \frac{\partial w_{\text{eq}}}{\partial \mathrm{II}_{\overline{\mathbf{C}}}} = c_{01}\frac{3}{2}\mathrm{II}^{1/2}_{\overline{\mathbf{C}}} \tag{5.61}$$

(3) **Overstress**

$$\tilde{\mathbf{T}}_{\text{ov}} = 2\rho_{\text{R}}\mu_0\frac{(\det\mathbf{C}_{\text{v}})^{1/3}}{(\det\mathbf{C})^{1/3}}\left(\mathbf{C}_{\text{v}}^{-1} - \frac{1}{3}(\mathbf{C}\cdot\mathbf{C}_{\text{v}}^{-1})\mathbf{C}^{-1}\right) \tag{5.62}$$

$$\dot{\mathbf{C}}_{\text{v}} = \frac{4\rho_{\text{R}}\mu_0}{\eta}\frac{(\det\mathbf{C}_{\text{v}})^{1/3}}{(\det\mathbf{C})^{1/3}}\left(\mathbf{C} - \frac{1}{3}(\mathbf{C}\cdot\mathbf{C}_{\text{v}}^{-1})\mathbf{C}_{\text{v}}\right) \tag{5.63}$$

$$\eta = \eta_0 e^{\left(-s_0\sqrt{\mathbf{C}\mathbf{T}_{\text{ov}}\cdot\mathbf{T}_{\text{ov}}\mathbf{C}}\right)} \tag{5.64}$$

symmetry can be utilised by spatially discretizing only one-eighth of the specimen. It is meshed using 20-noded mixed hexahedral elements (Q2P1-elements of Simo and Taylor (1991a), see, for details (Hartmann, 2002) as well. Fig. 5.23 represents the mesh and the boundary conditions applied. In order to identify the material parameters, it is essential to compare the experiment and the simulation. To compare them, FEM nodes are projected on to the DIC data points. It is not possible to obtain the data of the entire finite element mesh from the DIC. Thus a region of interest is predetermined and will be analyzed for all the time steps. From a commercial DIC-system, it is possible to obtain the spatial coordinates of the points on the specimen as well as the surface displacements. As explained previously, in biaxial tests, the rigid body motions cannot

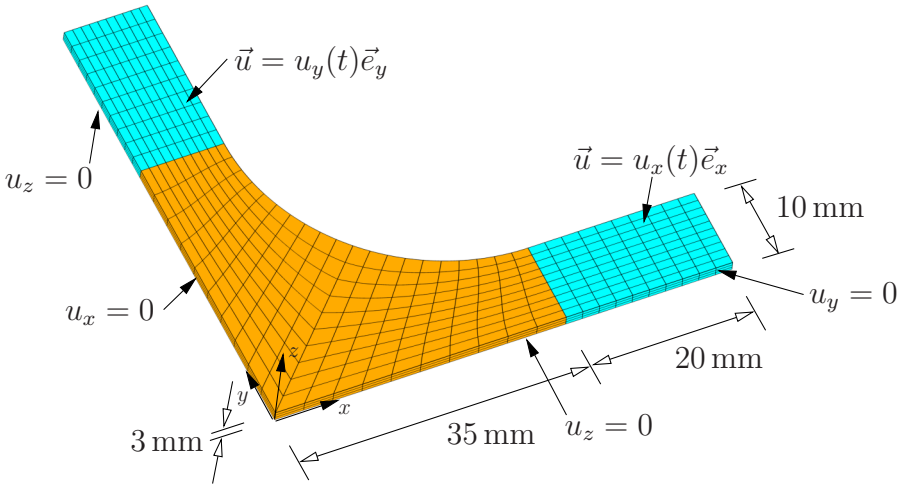


Figure 5.23.: Mesh using 20-noded Q2P1-elements and the boundary conditions applied ($n_{\mathrm{u}} = 8472$), see (Hartmann and Gilbert, 2021)

be accounted for and as such evaluation of strain is essential. The DIC data points are obtained at different time steps. Only data points that are available at all time steps need to be taken into consideration. Following the interpolation concept proposed by Hartmann and Rodriguez (2018), the strain data for both the DIC-data as well as finite element nodal displacement data are calculated based on triangulation, see (Hsu et al., 1994; Orteu, 2009). After this step is completed, based on the triangulation tool proposed by (Shewchuk, 1996, 2002), both the DIC-data points as well as the finite element nodal points are triangulated by Delaunay triangulation method. The triangles with the smallest angle less than $20^\circ$ are eliminated. The triangulated surface regions of both the DIC-data points as well as the finite element nodal points are shown in Fig. 5.24. Classical interpolation technique is used to project the FEM to DIC to obtain the strains of the experiment at the FEM nodes, see (Hartmann and Rodriguez, 2018) as well as Appendix A.2. The ability to compute displacement and strain at any available DIC-region as well as the finite element model provide a great amount of flexibility in the identification process.

### 5.2.4. Mixed Elements

Before going into the details about the identification of material parameters, it is essential to explain why mixed elements were used instead of displacement elements. Simple displacement elements are too stiff for almost incompressible materials, mixed formulation needs to be used in the case of hyperelasticity for rubber-like materials based on the three-field formulation by Simo (1985); Simo and Taylor (1991b). The variation formulation is modified to extend two additional scalar unknowns, $\Theta$ and $\lambda$. These scalar unknowns are volumetric strain, $\Theta$ and the lagrangian multiplicator, $\lambda$. By applying the method of vertical lines, the resulting DAE system can be solved by the procedures detailed in Sec. 3.4. For volumetric strains and lagrangian multiplicator, element-wise continuous shape functions lead to *Q1P0* and *Q2P1* elements, see

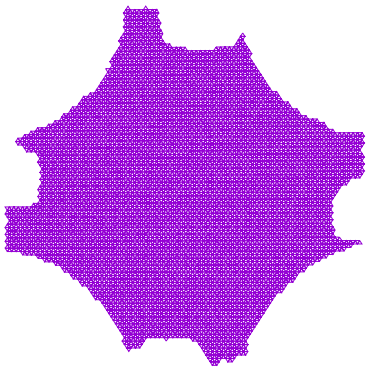

(a) Triangulation of the entire DIC-data

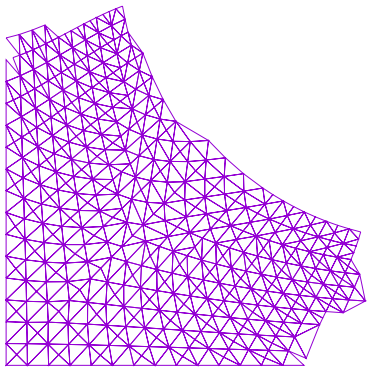

(b) Triangulation of the FEM-data (only the region which is compared to the DIC-data is shown)

Figure 5.24.: Triangulation of surface data for strain determination, see (Hartmann and Gilbert, 2021)

for more details (Wriggers, 2008; Hartmann, 2003).

## 5.2.5. Setting up of the Identification Problem

Different aspects of the identification problem have already been extensively addressed in Chapter 4. Therefore, here only certain aspects of the quantities are explained. Initially the the notations regarding the experimental data are discussed here. When using full-field measurement along with forces, for each experiment $E$, $E = 1, \ldots, n_{\text{exp}}$, a data vector $\boldsymbol{d}^{(E)} \in \mathbb{R}^{n_{\text{exp}}^{(E)}}$ is obtained. This data vector contains information about totally $n_{\text{N}}^{(E)}$ (temporal) load-steps. In each time step $n_{\text{d}}^{(E)}$ number of entries exists. These entries are the full-field data (spatially distributed displacements or as in this case, stretches) and forces in horizontal and vertical directions of the biaxial testing machine, $n_{\text{exp}}^{(E)} = n_{\text{N}}^{(E)} n_{\text{d}}^{(E)}$.The experimental evaluation times are $t_m$, $m = 1, \ldots, n_{\text{N}}^{(E)}$. These data vectors are assembled into the vector $\boldsymbol{d}^{(E)T} = \{\boldsymbol{d}_0^{(E)T}, \boldsymbol{d}_1^{(E)T}, \ldots, \boldsymbol{d}_{n_{\text{N}}^{(E)}}^{(E)T}\}$, where $\boldsymbol{d}_m^{(E)} \in \mathbb{R}^{n_{\text{d}}^{(E)}}$ contains the information of one experiment. For all tests under consideration, this leads to the entire data vector $\boldsymbol{d}^T = \{\boldsymbol{d}^{(1)T}, \boldsymbol{d}^{(2)T}, \ldots, \boldsymbol{d}^{(n_{\text{exp}})T}\}$, $\boldsymbol{d} \in \mathbb{R}^{n_{\text{D}}}$, with $n_{\text{D}} = \sum_{E=1}^{n_{\text{exp}}} n_{\text{exp}}^{(E)}$.

The determination of the strain/stretch data at each time step $t_n^{(E)}$, $n = 1, \ldots, N^{(E)}$ has been discussed in Sec.5.2.3. In this example, stretch values are used. The common letter for stretch is $\lambda$. However, $\lambda$ is already used in the Lagrange-multiplier $\boldsymbol{\lambda}$ method. Thus $\tau$ is used to represent the stretch henceforth. The simulation component

$$s_k(\boldsymbol{\kappa}) = \tau_k(\tilde{\boldsymbol{u}}_n(\boldsymbol{\kappa})) \tag{5.65}$$

is indirectly dependent on the parameter set $\boldsymbol{\kappa}$. $k = 1, 2$ where the indices $1, 2$ indicate the horizontal and the vertical directions respectively. In the case of a principal strain measure (alternate

measure to stretches), this reads $\varepsilon_k(\tau_k(\tilde{\boldsymbol{u}}_n(\boldsymbol{\kappa})))$. Finally, an integral quantity, like force, measured from the force-gauges placed at the clamps in horizontal and vertical axes is also taken into consideration for the identification process. The finite element model provides stretches ($\tau_n(\boldsymbol{u}_n^{(E)})$ and $\tau_n(\overline{\boldsymbol{u}}_n^{(E)})$), and reaction forces $\boldsymbol{\lambda}_n^{(E)}$ at each time steps. In order to compare the experiment and the simulation, the temporal points for both the cases should coincide. Thus it is essential that the reaction forces and the stretches are interpolated to the time steps. Since, the sensitivities are determined using IND, see Section 4.4.3, it is better to linearly interpolate the experimental data to the simulated data. This is done because sensitivities cannot be interpolated. Thus the size of the data vectors $\boldsymbol{d}$ is adjusted to the data from the finite element computations.

Since, the entire vector $\boldsymbol{d}$ of all experimental data embodies different physical properties like forces, displacements, strains etc., it is essential to weight the residuum vector. Additionally, the number of entries in the forces data is very much lesser when compared to the number of entries in the strain data points. Thus, weights to balance the number should also be in the weights introduced, see Eq.(4.9)

$$\tilde{\boldsymbol{r}}(\boldsymbol{\kappa}) = \boldsymbol{W}\boldsymbol{r}(\boldsymbol{\kappa}) = \boldsymbol{W}\{\boldsymbol{s}(\boldsymbol{\kappa}) - \boldsymbol{d}\}. \tag{5.66}$$

This is based on the concepts proposed in (Hartmann, 2001a). The entire weighting matrix reads

$$\boldsymbol{W} = \begin{bmatrix} \boldsymbol{W}^{(1)} & & \\ & \ddots & \\ & & \boldsymbol{W}^{(n_{\text{exp}})} \end{bmatrix} \quad \text{with} \quad \boldsymbol{W}^{(E)} = \begin{bmatrix} \boldsymbol{W}_0^{(E)} & & \\ & \ddots & \\ & & \boldsymbol{W}_{n_{\text{N}}^{(E)}}^{(E)} \end{bmatrix}. \tag{5.67}$$

Within the weighting matrix

$$\boldsymbol{W}_n^{(E)} = \begin{bmatrix} w_F^{(E)} & & \\ & w_F^{(E)} & \\ & & w_\varepsilon^{(E)}\boldsymbol{I} \end{bmatrix}, \tag{5.68}$$

where the same weight

$$w_F^{(E)} = \frac{1}{\left( \max\limits_{n=1,\ldots,n_{\text{N}}^{(E)}} \left| F_n^{(E)} \right| \right) n_{\text{N}}^{(E)}} \tag{5.69}$$

is used for the force data in vertical and horizontal direction of the biaxial tensile tests. The weighting factors of the principal strain data are defined by

$$w_\varepsilon^{(E)} = \frac{1}{\left( \left\| \boldsymbol{\varepsilon}_n^{(E)} \right\|_{\max\limits_{n=1,\ldots,n_{\text{N}}^{(E)}}} \right) n_{\text{d}}^{(E)}}. \tag{5.70}$$

## 5.2.6. Determination of Sensitivities

To demonstrate the determination of sensitivities, an incidence matrix $\tilde{\boldsymbol{M}}^{(E)}$ is introduced to extract the required nodal displacements. $F_{\text{FEM1}n}^{(E)} = -\overline{\boldsymbol{M}}_1^{(E)T}\boldsymbol{\lambda}_n$ and $F_{\text{FEM2}n}^{(E)} = -\overline{\boldsymbol{M}}_2^{(E)T}\boldsymbol{\lambda}_n$ represent

the horizontal and vertical forces from the two clamps. $\overline{\boldsymbol{M}}_k^{(E)} \in \mathbb{R}^{n_{\mathrm{p}^{(k)}}}$, $k = 1, 2$ is chosen to extract the nodal reaction forces required to determine the scalar values. The indices $1, 2$ indicate the horizontal and the vertical directions respectively. Here, the sensitivity matrix

$$\boldsymbol{D}(\boldsymbol{\kappa}) = \frac{\mathrm{d}\tilde{\boldsymbol{r}}(\boldsymbol{\kappa})}{\mathrm{d}\boldsymbol{\kappa}} = \boldsymbol{W}\frac{\mathrm{d}\boldsymbol{s}(\boldsymbol{\kappa})}{\mathrm{d}\boldsymbol{\kappa}}, \tag{5.71}$$

$\boldsymbol{D} \in \mathbb{R}^{n_{\mathrm{D}} \times n_{\kappa}}$ is calculated based on internal numerical differentiation and external numerical differentiation methods detailed in Section 4.4. These sensitivities with respect to the parameter vector $\boldsymbol{\kappa}$ are,

$$\frac{\mathrm{d}F_{\mathrm{FEM}n}^{(E)}(\boldsymbol{\kappa})}{\mathrm{d}\boldsymbol{\kappa}} = -\overline{\boldsymbol{M}}^{(E)T}\frac{\mathrm{d}\boldsymbol{\lambda}_n^{(E)}(\boldsymbol{\kappa})}{\mathrm{d}\boldsymbol{\kappa}}, \quad \frac{\mathrm{d}\tilde{\boldsymbol{u}}_n^{(E)}(\boldsymbol{\kappa})}{\mathrm{d}\boldsymbol{\kappa}} = \tilde{\boldsymbol{M}}^{(E)}\frac{\mathrm{d}\boldsymbol{u}_n^{(E)}(\boldsymbol{\kappa})}{\mathrm{d}\boldsymbol{\kappa}}. \tag{5.72}$$

The derivatives of the principal strains (or stretches) with respect to the parameters $\boldsymbol{\kappa}$ are obtained using the chain-rule,

$$\frac{\mathrm{d}\varepsilon_k}{\mathrm{d}\boldsymbol{\kappa}} = \frac{\mathrm{d}\varepsilon_{kn}}{\mathrm{d}\tau_{kn}}\left\{\frac{\mathrm{d}\tau_{kn}}{\mathrm{d}\tilde{\boldsymbol{u}}_n}\right\}^T\left[\frac{\mathrm{d}\tilde{\boldsymbol{u}}_n}{\mathrm{d}\boldsymbol{\kappa}}\right], \tag{5.73}$$

see Eq.(5.72)$_2$, see Appendix A.3.

## 5.2.7. Preliminary Investigation

Based on the investigations in Chapter 4 and (Hartmann and Gilbert, 2018), it was found out that in order to check whether material parameters can be determined uniquely using the experiments, a re-identification using synthetic data needs to be carried out at first. Thus, such a procedure was carried out for this example also. The geometry of the biaxial tensile specimens are shown in Fig. 5.21. With a $\xi_p \approx 0.145$, it was concluded that the parameters are locally identifiable for the equilibrium part. Similar re-identification procedure was carried out for overstress part using synthetic data yielding $\xi_p \approx 0.0257$ indicating local identifiability. Once the re-identification using synthetic data is completed, the identification of the material parameters for the rubber specimen can be determined.

## 5.2.8. Identification of Material Parameters

In order to identify the material parameter $\boldsymbol{\kappa}_{\mathrm{eq}}$ and $\boldsymbol{\kappa}_{\mathrm{ov}}$, a step-wise identification procedure is followed. At first, the termination points of relaxation resulting from the loading process in Fig. 5.22(b) are chosen to determine $\boldsymbol{\kappa}_{\mathrm{eq}}^T = \{K, c_{10}, c_{01}\}$. Secondly, the four monotonous rate-dependent tests, see Fig. 5.22(a), along with the multi-step relaxation loading path shown in Fig. 5.22(b) are taken into consideration to identify $\boldsymbol{\kappa}_{\mathrm{ov}}$.

## 5.2.9. Identification of Equilibrium Stress Part

Based on the investigations by Hartmann et al. (2018a) and Section 5.1.3, it was found out that, in order to accurately identify the material parameters using biaxial experiments, the displacement applied in one direction requires to be much bigger than the displacement applied in the

perpendicular direction. Following this finding, a displacement of four times the horizontal displacement was applied in the vertical direction, see Fig. 5.22(b). The preliminary investigation performed in Section 5.2.7 found out that the problem is uniquely identifiable. The material parameters of the equilibrium stress part $\boldsymbol{\kappa}^T = \{K, c_{10}, c_{01}\}$ are identified using data from the termination points of relaxation in multi-step relaxation tests. The experimental vector is a big vector containing maximum as well as minimum principal surface strain of each node under consideration and the forces at each termination point of relaxation. Since the equilibrium parts contain no internal variables, a NLS-problem applied to systems of non-linear equations, see Eq.(3.46) needs to be solved depending on whether the sensitivities are calculated using IND, Eqs.(4.46)-(4.55) or END as discussed in Section 4.4.2. The experiment vector for identification is compiled of force data points and strain data points. The total number of force data points are 12, meanwhile, the total number of strain data points are 5472. Thus, appropriate weighting according to Eq.(5.67) is necessary. Here, both the surface strains and the force-displacement curves provided by the termination points of relaxation are compared. The parameter vector is $\boldsymbol{\kappa}_{\text{eq}}$, see model (5.46) for $\tilde{\mathbf{T}}_{\text{ov}} = \mathbf{0}$.

The identified material parameters are compiled in Tab. 5.2. The results plotted in the Fig. 5.25(a)

Table 5.2.: Identified material parameters of the equilibrium stress part

| Equilibrium stress part $\boldsymbol{\kappa}_{\text{eq}}$ | | |
|---|---|---|
| $K$ $\text{N}\,\text{mm}^{-2}$ | $c_{10}$ $\text{N}\,\text{mm}^{-2}$ | $c_{01}$ $\text{N}\,\text{mm}^{-2}$ |
| $5706.81 \pm 222$ | $0.012 \pm 0.007$ | $0.33 \pm 0.004$ |

have an $R^2$-value of $0.994$. The computational strain distribution at the final point is compared with the experimental strain distribution. Here, both the maximum and minimum principal strains are considered. Fig. 5.25(b) shows the relative error of the principal maximum strains

$$e = \frac{|\varepsilon_{\text{max,exp}} - \varepsilon_{\text{max,sim}}|}{|\varepsilon_{\text{max,exp}}|} \times 100. \tag{5.74}$$

Here, the relative error is around 20% in the center region of the specimen. From the confidence interval of the material parameters, it is clear that only $c_{10}$ is sensitive. This is attributed to the lower loading in the middle region that is used for identification compared to the less data available in the heavily loaded sample arms. It is a well-known fact that the first and second invariant $\text{I}_{\overline{\mathbf{C}}}$ and $\text{II}_{\overline{\mathbf{C}}}$ are strongly coupled in pure tensile tests, see Fig. 5.26. In the biaxial tensile test this is less pronounced, but is visible in the correlation matrix (always calculated with the help $\det \boldsymbol{H}$ and not $\xi_p$):

$$\boldsymbol{C} = \begin{bmatrix} 1.0 & 0.107 & -0.623 \\ & 1.0 & -0.841 \\ & & 1.0 \end{bmatrix}. \tag{5.75}$$

There is a strong correlation between the parameters $c_{10}$ and $c_{01}$, see Eq.(4.21). This is due to fact that the invariants $\text{I}_{\overline{\mathbf{C}}}$ and $\text{II}_{\overline{\mathbf{C}}}$ are in the small strain range dependent on each other. Here,

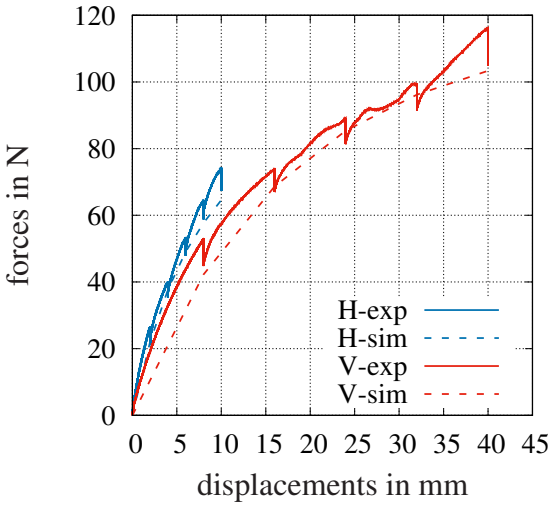


(a) Calibration of equilibrium stress part at termination points of relaxation

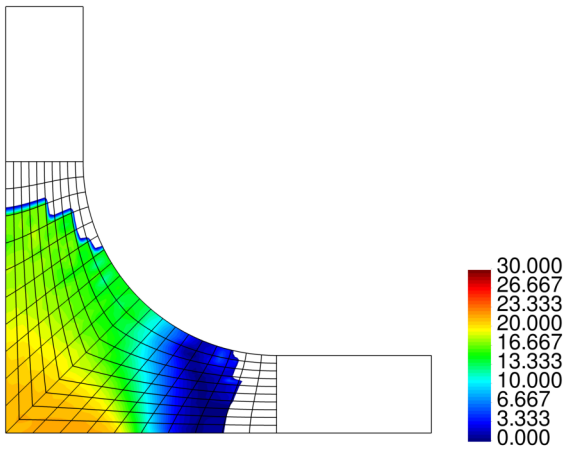


(b) Relative error $e$ of final principal strain, see definition (5.74)

Figure 5.25.: Force-displacement identification result and relative error in principal strains, see (Hartmann and Gilbert, 2021)

the variance (square of the standard deviation) is $s^2 = 0.053$ is small. With a $\xi_p \approx 0.0014$, it was concluded that the parameters are locally identifiable for the equilibrium part.

The computations are done using the in-house finite element program TASAFEM on a four-core computer with an Intel(R) Core(TM) i7-4770 processor (8MB Cache, 3.4GHz) and 16GB memory. Furthermore, the linear solver PARDISO, (Schenk and Gärtner, 2006), addressing 8 threads were applied. The computations required 25 iterations for a starting vector $\boldsymbol{\kappa}_{\text{eq}}^{(0)} = \{100, 0.264, 0.5\}$. In the case of END, it took 104 function calls to identify the material parameters and took around $6200\text{s}$. In the case of IND, the entire identification process finished in $1800\text{s}$. It takes END a factor of 3.4 times the time in comparison IND to complete the identification process. This proves the computational efficiency of IND.

## 5.2.10. Identification of Overstress Part

For the overstress part, in the whole structure $n_{\text{u}} = 8472$ unknown nodal displacements and $n_{\text{Q}} = 194400$ unknown internal variables exist. The material parameters $\boldsymbol{\kappa}_{\text{eq}}$, see Tab. 5.2, identified in the previous step are fixed and the parameters $\boldsymbol{\kappa}_{\text{ov}}^T = \{\mu_0, \eta_0, s_0\}$ on the basis of the four monotonous displacement rates in the loading paths of Fig. 5.22(a) and the multi-step relaxation path of Fig. 5.22(b) have to be determined. Similar to the identification of the equilibrium stress part, the horizontal and vertical measured force data, and the maximum as well as minimum strain data are used to identify the material parameters. However, compared to the previous case, in the determination of parameters of overstress part, the number of data points are significantly higher. The total number of force data points are 652063, meanwhile, the total number of strain data points are 1656048. Thus, appropriate weighting according to Eq.(5.67) is necessary.

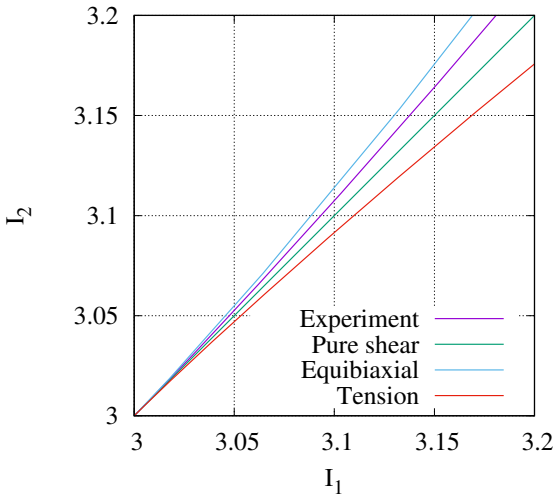


Figure 5.26.: Comparison of invariants

The time-adaptive time integrator is the second-order scheme of Ellsiepen, see (Ellsiepen, 1999; Diebels et al., 1999) and Appendix A.1, which is based on the second-order method of (Alexander, 1977). The result of identification of the force-displacement curves is shown in Fig. 5.27 (the strain data is not shown here). The coefficient of determination $R^2 = 0.9903$ shows a good fit, see Fig. 5.27. The parameters are assembled in Tab. 5.3. The parameters result from the starting

Table 5.3.: Identified material parameters of the overstress part

| Overstress part $\boldsymbol{\kappa}_{\mathrm{ov}}$ | | |
|---|---|---|
| $\mu_0$ $\mathrm{N\,mm^{-2}}$ | $\eta_0$ $\mathrm{s\,mm^2\,N^{-1}}$ | $s_0$ $(\mathrm{N\,mm^{-2}})^{-1}$ |
| $0.26 \pm 0.02$ | $14113.39 \pm 4405$ | $0.00053 \pm 0.006$ |

values of the iterative scheme $\boldsymbol{\kappa}_{\mathrm{ov}}^{(0)} = \{0.2, 180, 0.001\}$. With a $\xi_p \approx 0.0003$, it was concluded that the parameters are locally identifiable for the overstress part. The parameter $s_0$ required for incorporating rate dependence has not a good quality since the confidence interval is larger than value itself. This could be accounted to the noise in the experimental data itself. This is indicated also by the correlation matrix

$$\boldsymbol{C} = \begin{bmatrix} 1 & -0.075 & 0.015 \\ & 1 & 0.934 \\ & & 1 \end{bmatrix}, \tag{5.76}$$

where the viscosity $\eta_0$ and $s_0$ are strongly correlated. The variance $s^2 = 0.0573$ is, however, small.

In the case of END, the entire identification process took around $47000\mathrm{s}$ while in the case of IND, the entire identification process finished in $13250\mathrm{s}$. The comparison of the computations

with analytical derivatives (IND) with numerical differentiation (END) yields again a factor of 3.5 showing again the advantage of using IND over END.

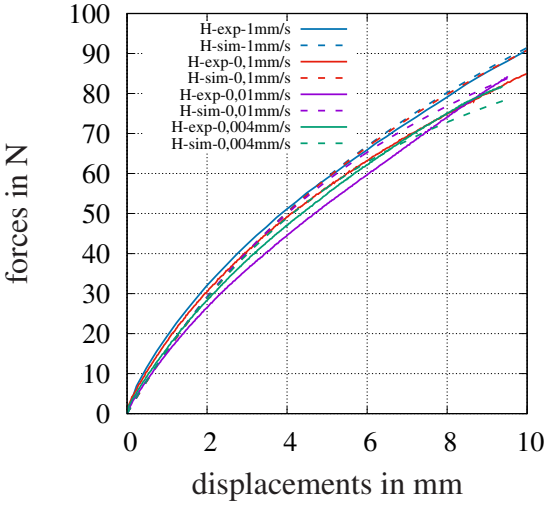


(a) Horizontal rate-dependent calibration results

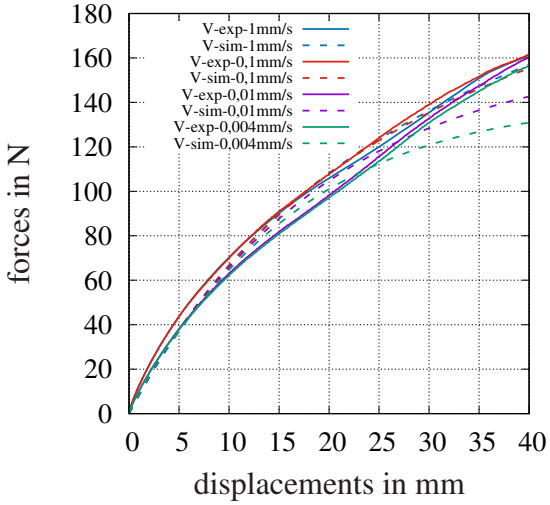


(b) Vertical rate-dependent calibration results

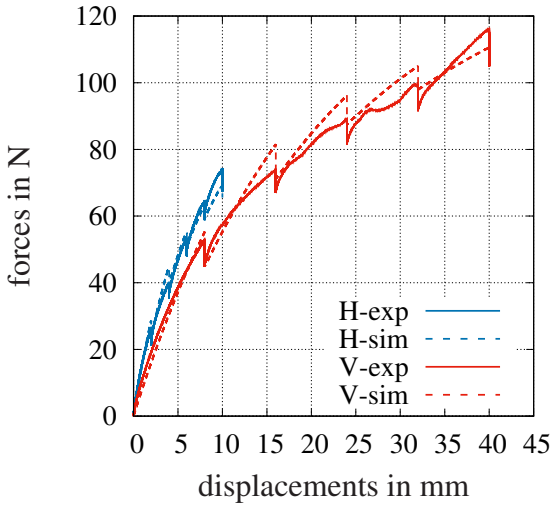


(c) Calibration of overstress-type model at multi-step relaxation path

Figure 5.27.: Force-displacement results of identification of rate dependence and relaxation, see (Hartmann and Gilbert, 2021)

# 6. Conclusion

The aim of the thesis is to present an overview about the different aspects of material parameter identification. The different concepts regarding identification of material parameters have been presented with particular focus on the identifiability and determination of sensitivities. All these concepts have been explained with different examples and a real example of an overstress-type finite strain viscoelasticity applied on biaxial tests performed on rubber specimen.

The thesis introduces the basic ideas of Continuum Mechanics as well as how the partial differential equation can be solved using the finite element method. Starting from the derivation of the weak form of balance of linear momentum, the method of vertical lines is detailed. This is followed by spatial discretization. The spatial discretization results in a system of differential-algebraic systems which is then discretized in temporal domain using the very simple and popular Backward-Euler schemes or the slightly more complicated yet flexible and better high-order time integrators like diagonally-implicit Runge-Kutta schemes. The time discretization yields a system of non-linear equations which can be solved using the classic Newton-Raphson scheme for material models without internal variables like hyperelasticity and using Multi-Level Newton algorithm for material models with internal variables like viscoelasticity, viscoplasticity or rate-dependent plasticity. For most of the finite element simulations, a FORTRAN based in-house code TASAFEM was used.

If the identified material parameters of a constitutive model are not locally unique, the predicted response of the components in real world may not be accurate. The non-linear least square algorithm which forms the basis of material parameter identification is an ill-posed problem which may lead to multiple solutions. On the basis of this question, the concept of local identifiability is discussed. Another important question arises about the quality of these identified material parameters. Due to the existence of multiple solutions of the problem, certain quality measures are required to better understand the parameters like correlation coefficient, coefficient of determination and confidence intervals. These aspects of material parameter identification are also addressed.

The concept of local identifiability is researched on the basis of several simple examples in linear isotropic elasticity like uniaxial tension (single and multi-layered), biaxial tests, thick-walled tube under internal pressure (single and multi-layered). Some examples (indentation and bending tests) for large strain analysis were also performed. The experimental data were synthesized by assuming material parameter values for bulk modulus $K$ and shear modulus $G$ (consequently modulus of elasticity $E$ and Poisson's number $\nu$). Since exact synthetic data leads to vanishing variance, perturbed synthetic data were also used. The examples show that for the proper identification of material parameters, experiments addressing the material parameters have to be provided. This was observed by the "valley" in the goal function, where there is no local solution, and infinite number of possible $K$ and $G$ combinations exists. In the case of

uniaxial tests, where both axial and lateral information were provided for the identification it was found out that there exists a local minimum. The quality of measures were also studied and found out that when the parameters were identified using both axial and lateral information, the material parameters were of a very good confidence.

On the basis of small strain linear isotropic elastic studies, the investigations were extended to large strain case as well. Indentation and bending tests were investigated. It was found out that using DIC information along with forces leads to satisfactory identification of parameters. *From all these investigations, it can be concluded that before identifying material parameters, it is essential to verify that the experiments performed are enough to identify the material parameters. Thus a re-identification is always suggested before material parameters are identified.*

Another important aspect of material parameter identification is the determination of sensitivities. Mostly, researchers use a direct finite difference scheme to obtain these sensitivities. However, it is a time consuming process in the case of models with a large number of internal variables and material parameters. On the basis of research by Schittkowski (2002), Hartmann (2017) compared three approaches namely, *simultaneous simulation equations*, *internal*, and *external numerical differentiation* for models with internal variables. These methods to determine the sensitivities of displacements and strains are explained in context of a constitutive model with internal variables. The determination of sensitivities of force are also explained.

Finally, a real world example of biaxial tests on carbon-black filled rubber specimens were performed to analyse all the concepts introduced in this thesis. Since, the biaxial tests result in inhomogeneous strain state in the middle of the specimen, finite element method needs to be used to identify the material parameters. An overstress-type finite strain viscoelastic model was used to characterize the behavior of the rubber specimen. However, before performing the actual experiments, a re-identification process was carried out to study the local identifiability. It was found out that using force values (horizontal and vertical) alone from biaxial tests were not enough to determine the material parameters. Thus, full-field data using DIC has also to be used in addition to the force data. For this purpose, strain values calculated at the nodes by the projection of FEM to DIC, were also used to re-identify the material parameters. This produced satisfactory results. The analytical derivatives to determine the sensitivities for IND are provided to the FE code as a FORTRAN routine that is developed with the help of *Acegen* (Mathematica addin). Thus, on the basis of the re-identification, the material parameters were identified stepwise. At first, the equilibrium parameters were identified followed by the overstress parameters. The results were good and the parameters were found to be locally unique. The time taken to complete the identification process while using END and IND were compared. It was concluded that the time taken for END is almost 3.5 times the time taken to complete the same identification process using IND thereby justifying the use of IND for material parameter identification. All the examples considered in this thesis, show that IND out performs END. *Thus, it is advised to use IND instead of END whenever possible.*

# A. Appendix

## A.1. Parameters of the Applied DIRK-methods

Tab. A.1 shows the factors of the DIRK-methods to give an overview of the High-order time integration schemes.

Table A.1.: Butcher-Tableaus of the different DIRK methods used

(a) Backward Euler ($s = 1, p = 1$)

$$\begin{array}{c|c} 1 & 1 \\ \hline & 1 \end{array}$$

(b) Alexander/Ellsiepen ($s = 2, p = 2, \hat{p} = 1$)

$$\begin{array}{c|cc} \alpha & \alpha & \\ 1 & 1-\alpha & \alpha \\ \hline & 1-\alpha & \alpha \\ & 1-\hat{\alpha} & \hat{\alpha} \end{array} \qquad \alpha = 1 - \tfrac{1}{2}\sqrt{2}, \qquad \hat{\alpha} = 2 - \tfrac{5}{4}\sqrt{2}$$

## A.2. Interpolation Technique

Following the application of the triangulation of the coordinates given by the DIC-system, the interpolation technique is applied. At first, only the in-plane coordinates are required. A function value $f^*$ (displacement or some strain measure component) is required at a given point $(x^*, y^*)$ in a triangular region given by $(x_1, y_1)$, $(x_2, y_2)$, and $(x_3, y_3)$, see Fig. A.1. Initially, it is required to find out whether the given point lies inside the triangle. Based on the vectorial property of the surface description

$$\vec{x}(\chi, \psi) = \vec{x}_1 + \chi(\vec{x}_2 - \vec{x}_1) + \psi(\vec{x}_3 - \vec{x}_1), \tag{A.1}$$

or in its component representation

$$\begin{Bmatrix} x^* \\ y^* \\ f^* \end{Bmatrix} = \begin{Bmatrix} x_1 \\ y_1 \\ f_1 \end{Bmatrix} + \chi \begin{Bmatrix} x_2 - x_1 \\ y_2 - y_1 \\ f_2 - f_1 \end{Bmatrix} + \psi \begin{Bmatrix} x_3 - x_1 \\ y_3 - y_1 \\ f_3 - f_1 \end{Bmatrix}, \tag{A.2}$$

the first two equations are obtained

$$\begin{bmatrix} x_2 - x_1 & x_3 - x_1 \\ y_2 - y_1 & y_3 - y_1 \end{bmatrix} \begin{Bmatrix} \chi \\ \psi \end{Bmatrix} = \begin{Bmatrix} x^* - x_1 \\ y^* - y_1 \end{Bmatrix}, \tag{A.3}$$

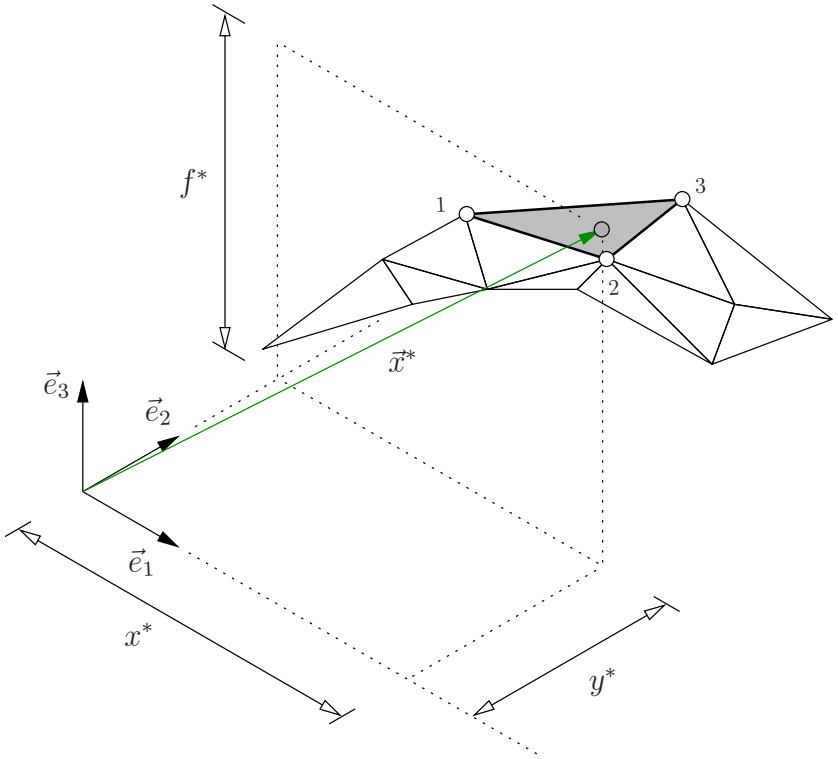


Figure A.1.: Interpolation of a point in a triangle, see (Hartmann et al., 2021)

with the values

$$\left\{ \begin{array}{c} \chi \\ \psi \end{array} \right\} = \frac{1}{(x_2 - x_1)(y_3 - y_1) - (x_3 - x_1)(y_2 - y_1)} \begin{bmatrix} y_3 - y_1 & x_1 - x_3 \\ y_1 - y_2 & x_2 - x_1 \end{bmatrix} \left\{ \begin{array}{c} x^* - x_1 \\ y^* - y_1 \end{array} \right\}. \tag{A.4}$$

If the conditions $0 \leq \chi \leq 1$, $0 \leq \psi \leq 1$, and $\chi + \psi \leq 1$ are fulfilled, the point lies inside the triangle. If the point is not within the triangle, the neighboring triangles are searched.

Using Eq.(A.2)$_3$, the value of $f^*$ is determined by

$$f^* = f_1 + \chi(f_2 - f_1) + \psi(f_3 - f_1) \tag{A.5}$$

for any given $\chi$ and $\psi$. Thus, for a given point $(x^*, y^*)$, the value $f^*$ can be calculated in the triangle.

## A.3. Sensitivities of the Surface Stretches

The common letter for stretch is $\lambda$. However, $\lambda$ is already used in the Lagrange-multiplier $\boldsymbol{\lambda}$ method. Thus $\tau$ is used to represent the stretch henceforth, see Section 5.2.5. The derivatives of the stretches $\tau_k$ with respect to the nodal displacements $\tilde{\boldsymbol{u}}_n$ are required. Hartmann and Rodriguez

(2018) explained the formulas to calculate the in-plane surface stretches by the displacements of the points. The square of stretches $\mu_k = \tau_k^2$ are determined by

$$\mu_{1,2} = \frac{\mathrm{I}_{\hat{\mathbf{C}}}}{2} \pm \sqrt{\frac{\mathrm{I}_{\hat{\mathbf{C}}}^2}{4} - \mathrm{II}_{\hat{\mathbf{C}}}^2}. \tag{A.6}$$

with the invariants of the right Cauchy-Green tensor

$$\mathrm{I}_{\hat{\mathbf{C}}} = \hat{C}^1{}_1 + \hat{C}^2{}_2, \qquad \mathrm{II}_{\hat{\mathbf{C}}} = \hat{C}^1{}_1\hat{C}^2{}_2 - \hat{C}^1{}_2\hat{C}^2{}_1. \tag{A.7}$$

Here,

$$\hat{C}^\alpha{}_\beta(\boldsymbol{\kappa}) = A^{\alpha\beta}\hat{C}_{\alpha\beta}(\boldsymbol{\kappa}), \quad \alpha = 1,2, \quad \beta = 1,2 \tag{A.8}$$

are the mixed-variant components. $[A^{\alpha\beta}] = [A_{\alpha\beta}]^{-1}$ can be computed by the metric of the tangent vectors, $\vec{A}_\alpha$, $\alpha = 1,2$, in the reference configuration $A_{\alpha\beta} = \vec{A}_\alpha \cdot \vec{A}_\beta$. If the surface is described by ansatz functions (similar to the shape functions in finite elements), then

$$\vec{A}_\alpha = \frac{\partial \vec{X}}{\partial \Theta^\alpha} = \left( \sum_{k=1}^{n_{\text{en}}} N_{k,\alpha}\, X_{kj} \right) \vec{e}_j. \tag{A.9}$$

Here, $X_{kj}$ are the coordinates in the reference configuration and $N_k(\Theta^1, \Theta^2)$ represents a surface description. $n_{\text{en}}$ represents the number of "element nodes". For convective coordinates, $\hat{C}_{\alpha\beta} = a_{\alpha\beta}$ with the metric coefficients $a_{\alpha\beta} = \vec{a}_\alpha \cdot \vec{a}_\beta$, which are based on the surface tangent vectors in the current configuration. Similar to the previous case, they can also be approximated by using ansatz functions,

$$\vec{a}_\alpha(\boldsymbol{\kappa}) = \frac{\partial \vec{x}}{\partial \Theta^\alpha} = \left( \sum_{k=1}^{n_{\text{en}}} N_{k,\alpha}\, x_{kj}(\boldsymbol{\kappa}, t) \right) \vec{e}_j, \tag{A.10}$$

where $x_{kj}(\boldsymbol{\kappa}, t) = X_{kj} + u_{kj}(\boldsymbol{\kappa}, t)$. In this regard, the derivatives $\partial\mu_k/\partial\tilde{\boldsymbol{u}}_n$ are calculated. This is done using Acegen to generate the analytical derivatives, (Korelc, 1997, 2002, 2009). The Acegen plugin used with Mathematica provides FORTRAN routines (or other languages) that can be used with the in-house FEM code TASAFEM to determine the sensitivities.

# B. List of Symbols

## Acronyms

| Symbol | Description | Page |
|---|---|---|
| CABG | Coronary Artery Bypass Graft | 1 |
| DAE | Differential Algebraic System | 4 |
| DFG | German Research Foundation | 1 |
| DIC | Digital Image Correlation | 5 |
| DIRK | Diagonally Implicit Runge-Kutta | 21 |
| DOF | Degree of Freedom | 26 |
| END | External Numerical Differentiation | 41 |
| ENIAC | Electronic Numerical Integrator and Computer | 1 |
| FEM | Finite Element Method | 1 |
| GIF | German-Israeli Foundation for Scientific Research and Development | 1 |
| IBVP | Initial Boundary Value Problem | 7 |
| IND | Internal Numerical Differentiation | 41 |
| LHS | Left Hand Side | 48 |
| MLNA | Multi-level Newton Algorithm | 5 |
| MOL | Method of Vertical Lines | 23 |
| NLS | Non-linear Least Square | 8 |
| RHS | Right Hand Side | 21 |
| SSE | Simultaneous Sensitivity Equations | 41 |

## 2nd order tensors

| Symbol | Description | Page |
|---|---|---|
| $\mathbf{A}$ | Almansi strain tensor | 14 |
| $\overline{\mathbf{B}}$ | Unimodular left Cauchy-Green tensor | 68 |
| $\mathbf{B}$ | Left Cauchy-Green tensor | 12 |
| $\mathbf{C}$ | Right Cauchy-Green tensor | 12 |
| $\overline{\mathbf{C}}$ | Unimodular right Cauchy-Green tensor | 68 |
| $\mathbf{C}_v$ | Viscous right Cauchy-Green tensor | 78 |

| Symbol | Description | Page |
|---|---|---|
| $\mathbf{D}$ | Strain rate tensor | 18 |
| $\mathbf{E}$ | Green strain tensor | 13 |
| $\delta\mathbf{E}$ | Virtual Green strain tensor | 23 |
| $\mathbf{F}$ | Deformation gradient | 11 |
| $\mathbf{F}_{\mathrm{e}}$ | Elastic part of deformation gradient | 78 |
| $\overline{\mathbf{F}}$ | Isochoric part of the $\mathbf{F}$ | 13 |
| $\hat{\mathbf{F}}$ | Volumetric part of the $\mathbf{F}$ | 13 |
| $\mathbf{F}_{\mathrm{v}}$ | Viscous part of deformation gradient | 78 |
| $\mathbf{H}$ | Displacement gradient tensor | 14 |
| $\mathbf{I}$ | Identity Tensor | 13 |
| $\mathbf{L}$ | Spatial velocity gradient | 18 |
| $\mathbf{Q}$ | Orthogonal tensor | 13 |
| $\mathbf{R}$ | Rotation tensor of polar composition of $\mathbf{F}$ | 12 |
| $\mathbf{S}$ | Weighted Cauchy stress tensor | 27 |
| $\mathbf{T}$ | Cauchy stress tensor | 14 |
| $\mathbf{T}_{\mathrm{R}}$ | First Piola-Kirchhoff stress tensor | 14 |
| $\widetilde{\mathbf{T}}$ | Second Piola-Kirchhoff stress tensor | 15 |
| $\tilde{\mathbf{T}}_{\mathrm{eq}}^{\mathrm{iso}}$ | Equilibrium part of $\widetilde{\mathbf{T}}$ | 78 |
| $\tilde{\mathbf{T}}_{\mathrm{ov}}$ | Overstress part of $\widetilde{\mathbf{T}}$ | 79 |
| $\mathbf{U}$ | Right stretch tensor | 12 |
| $\mathbf{V}$ | Left stretch tensor | 12 |

## Scalars

| Symbol | Description | Page |
|---|---|---|
| $a_{ij}$ | Weighting coefficients in Runge-Kutta scheme | 31 |
| $b_i$ | Weighting coefficients in Runge-Kutta scheme | 32 |
| $c_i$ | Weighting coefficients in Runge-Kutta scheme | 31 |
| $E$ | Young's modulus | 51 |
| $G$ | Shear modulus | 51 |
| $\mathrm{I}_{\overline{\mathbf{C}}}$ | First invariant of $\overline{\mathbf{C}}$ | 67 |
| $\mathrm{II}_{\overline{\mathbf{C}}}$ | Second invariant of $\overline{\mathbf{C}}$ | 67 |
| $K$ | Bulk modulus | 51 |
| $n_e$ | Number of elements | 24 |
| $n_{en}$ | Number of nodes per element | 27 |
| $n_{\mathrm{u}}^e$ | Number of displacement element degrees of freedom | 26 |
| $n_{\mathrm{GP}}$ | Number of Gauss points in each element | 28 |
| $n_n$ | Number of nodes | 24 |
| $n_{\mathrm{Q}}$ | Number of internal variables of complete structure | 28 |

| Symbol | Description | Page |
|---|---|---|
| $n_q$ | Number of internal variables at a Gauss point | 28 |
| $\nu$ | Poisson's ratio | 51 |
| $n_{\mathrm{a}}$ | Number of displacement degrees of freedom of the entire mesh | 26 |
| $n_{\mathrm{d}}$ | Number of experimental data points | 36 |
| $n_{\mathrm{exp}}$ | Number of experimental data points | 82 |
| $n_\kappa$ | Number of material parameters | 36 |
| $n_{\mathrm{N}}^{(E)}$ | Number of load-steps | 82 |
| $n_{\mathrm{p}}$ | Number of prescribed displacement degrees of freedom of the entire mesh | 26 |
| $n_{\mathrm{u}}$ | Number of unknown displacement degrees of freedom of the entire mesh | 26 |
| $\psi$ | Strain energy function | 67 |
| $\rho_{\mathrm{R}}$ | Density in the reference configuration | 15 |
| $\rho$ | Density in the current configuration | 15 |
| $R^2$ | Coefficient of determination | 40 |
| $t$ | Time | 10 |

# Vectors

| Symbol | Description | Page |
|---|---|---|
| $\mathrm{d}\vec{A}$ | Material surface element in the reference configuration | 11 |
| $\mathrm{d}\vec{a}$ | Material surface element in the current configuration | 11 |
| $\vec{E}_{\mathrm{A}}$ | Cartesian base vectors in the reference configuration | 11 |
| $\vec{e}_i$ | Cartesian base vectors in the current configuration | 11 |
| $\vec{\chi}_{\mathrm{R}}$ | Motion of material body | 10 |
| $\vec{k}$ | Body force density in the current configuration | 16 |
| $\vec{n}$ | Normal vector | 14 |
| $\vec{t}$ | Cauchy stress vector | 14 |
| $\vec{u}$ | Velocity vector | 10 |
| $\delta\vec{u}$ | Virtual displacement | 23 |

# Matrices

| Symbol | Description | Page |
|---|---|---|
| $\mathbf{B}_{\mathrm{u}}^{e}$ | $\in \mathbb{R}^{6\times 3n_{\mathrm{u}}^{e}}$, Strain displacement matrix on element level with respect to the current configuration | 27 |
| $\widetilde{\mathbf{B}}_{\mathrm{ua}}^{e}$ | $\in \mathbb{R}^{6\times 3}$, Strain displacement matrix on element level for node $a$ | 28 |

| Symbol | Description | Page |
|---|---|---|
| $\widetilde{\mathbf{B}}_{\mathrm{u}}$ | $\in \mathbb{R}^{6\times 3n_{\mathrm{u}}^{e}}$, Strain displacement matrix on element level with respect to the reference configuration | 27 |
| $\boldsymbol{C}$ | Correlation matrix | 39 |
| $\boldsymbol{d}$ | $\in \mathbb{R}^{n_{\mathrm{d}}}$ Experimental data vector | 35 |
| $\boldsymbol{D}$ | Sensitivity matrix | 37 |
| $\boldsymbol{G}$ | Global level in MLNA | 33 |
| $\boldsymbol{g}_{\mathrm{u}}$ | Discretized principle of virtual displacements | 27 |
| $\boldsymbol{H}$ | Hessian matrix | 38 |
| $\mathbf{J}^{e}$ | Jacobian matrix of transformation from parametric $\boldsymbol{\xi}$-space into the reference configuration | 25 |
| $\mathbf{j}^{e}$ | Jacobian matrix of transformation from parametric $\boldsymbol{\xi}$-space into the current configuration | 25 |
| $\boldsymbol{J}$ | $\in \mathbb{R}^{n_{\mathrm{d}}\times n_{\kappa}}$ Jacobian with respect to material parameters $\boldsymbol{\kappa}$ | 37 |
| $\boldsymbol{\kappa}$ | $\in \mathbb{R}^{n_{\kappa}}$ Vector of material paramters | 35 |
| $\boldsymbol{L}$ | Local level in MLNA | 33 |
| $\boldsymbol{\lambda}$ | $\in \mathbb{R}^{n_{\mathrm{p}}}$Lagrange multiplier vector | 30 |
| $\mathbf{N}_{\mathrm{u}}^{e}$ | $\in \mathbb{R}^{3\times n_{\mathrm{u}}^{e}}$, Matrix of shape functions related to the displacements | 26 |
| $\boldsymbol{q}$ | $\in \mathbb{R}^{n_{\mathrm{Q}}}$, Internal variables of the whole structure | 26 |
| $\mathbf{q}$ | $\in \mathbb{R}^{n_{\mathrm{q}}}$, Internal variables at a Gauss point | 21 |
| $\tilde{\mathbf{r}}$ | Evolution equation functions | 28 |
| $\mathbf{r}$ | Residuum vector | 35 |
| $\tilde{\mathbf{r}}$ | Weighted residuum vector | 37 |
| $\boldsymbol{s}$ | $\in \mathbb{R}^{n_{\mathrm{d}}}$ Simulated data vector | 35 |
| $\boldsymbol{S}_{ni}^{\lambda}$ | Starting vector for $\boldsymbol{\lambda}$ in DIRK method | 31 |
| $\boldsymbol{S}_{ni}^{\mathrm{q}}$ | Starting vector for internal variables in DIRK method | 31 |
| $\boldsymbol{S}_{ni}^{\mathrm{u}}$ | Starting vector for displacements in DIRK method | 31 |
| $\boldsymbol{u}$ | $\in \mathbb{R}^{n_{\mathrm{uu}}}$, Vector of unknown nodal displacements | 26 |
| $\boldsymbol{u}_{\mathrm{a}}$ | $\in \mathbb{R}^{n_{\mathrm{ua}}}$, Displacement degree of freedom of the entire mesh | 26 |
| $\overline{\boldsymbol{u}}$ | $\in \mathbb{R}^{n_{\mathrm{up}}}$, Vector of prescribed nodal displacements | 26 |
| $\boldsymbol{W}$ | Diagonal weighting matrix | 37 |
| $\boldsymbol{\xi}$ | Local coordinates | 25 |
| $\boldsymbol{M}$ | $\in \mathbb{R}^{(n_{\mathrm{u}}+n_{\mathrm{p}})\times n_{\mathrm{p}}}$, Incidence matrix to differentiate between known and unknown displacement degree of freedom | 30 |
| $\overline{\boldsymbol{Z}}_{\mathrm{u}}^{e}$ | $\in \mathbb{R}^{n_{\mathrm{u}}^{e}\times n_{\mathrm{up}}}$, Incidence matrix for the prescribed displacement degree of freedom | 26 |

| Symbol | Description | Page |
|---|---|---|
| $\boldsymbol{Z}_{\mathrm{u}}^{e}$ | $\in \mathbb{R}^{n_{\mathrm{u}}^{e} \times n_{\mathrm{uu}}}$, Incidence matrix for the unknown displacement degree of freedom | 26 |

## Miscellaneous

| Symbol | Description | Page |
|---|---|---|
| $\chi$ | Arbitrary configuration of material body | 10 |
| $\mathcal{B}$ | Material body | 9 |
| $\chi_t$ | Current configuration of material body | 10 |
| $\mathbb{E}$ | Three dimensional Euclidean space of physical observation | 9 |
| $\mathcal{K}$ | Set of configurations | 10 |
| $\mathcal{P}$ | Material point or particle | 9 |
| $\mathbb{R}$ | Set of real numbers | 10 |
| $\mathcal{R}$ | Reference configuration of material body | 10 |
| $\mathrm{d}V$ | Material volume element in the reference configuration | 11 |
| $\mathrm{d}v$ | Material volume element in the current configuration | 11 |
| $\mathrm{d}\vec{X}$ | Material line element in the reference configuration | 11 |
| $\mathrm{d}\vec{x}$ | Material line element in the current configuration | 11 |

# Bibliography


Alexander, R. (1977). Diagonally implicit Runge-Kutta methods for stiff O.D.E.'s. *SIAM Journal on Numerical Analysis*, 14:1006–1021.

Amin, A. F. M. S., Alam, M. S., and Okui, Y. (2002). An improved hyperelasticity relation in modeling viscoelasticity response of natural and high damping rubbers in compression: experiments, parameter identification and numerical verification. *Mechanics of Materials*, 34:75–95.

Andresen, K., Dannemeyer, S., Friebe, H., Mahnken, R., Ritter, R., and Stein, E. (1996). Parameteridentifikation für ein plastisches Stoffgesetz mit FE-Methoden und Rasterverfahren. *Bauingenieur*, 71:21–31.

Anscombe, F. J. (1973). Graphs in statistical analysis. *The American Statistician*, 27:17–21.

Arruda, E. M. and Boyce, M. C. (1993). A three-dimensional constitutive model for the large stretch behavior of rubber elastic materials. *Journal of the Mechanics and Physics of Solids*, 41:389–412.

Ascher, U. M. and Petzold, L. R. (1998). *Computer methods for ordinary differential equations and differential-algebraic equations*. SIAM Society for Industrial and Applied Mathematics, Philadelphia.

Babuska, I., Szabo, B. A., and Katz, I. N. (1981). The p-version of the finite element method. *SIAM journal on numerical analysis*, 18(3):515–545.

Bai, Y., Igland, T. R., and Moan, T. (1997). Tube collapse under combined external pressure, tension and bending. *Marine Structures*, 10(5):389–410.

Balzani, D., Neff, P., Schröder, J., and Holzapfel, G. A. (2006). A polyconvex framework for soft biological tissues. adjustment to experimental data. *International Journal of Solids and Structures*, 43:6052–6070.

Bathe, K. J. (1986). *Finite Elemente Methode Übersetzung v. Zimmermann, P.* Springer, Berlin, 1st edition.

Bathe, K. J. (2002). *Finite - Elemente - Methoden*. Springer, Berlin, 1st edition.

Bazaraa, M. S., Sherali, H. D., and Shetty, C. M. (1993). *Nonlinear Programming*. John Wiley & Sons, New York.

Beck, J. V. and Arnold, K. J. (1977). *Parameter estimation in engineering and science*. John Wiley & Sons, New York.

Bellec, E. (2018). "RE-LAUNCHING" A self-made biaxial machine. Comparison to other biaxial tests and FE simulation for different elastomers. Technical report, DIK Deutsches Institut für Kautschuktechnologie e.V., Hannover, Germany.

Benedix, U., Görke, U.-J., Kreißig, R., and Kretzschmar, S. (1998). Local and global analysis of inhomogeneous displacement fields for the identification of material parameters. In Hoa, S. V., De Wilde, W. P., and Blain, W. R., editors, *Computer Methods in Composite Materials VI (CADCOMP 98)*, pages 159–168.

Bergström, J. S. and Boyce, M. C. (1998). Constitutive modeling of the large strain time-dependent behavior of elastomers. *Journal of the Mechanics and Physics of Solids*, 46:931–954.

Bettendorf, A. (2019). *Optimum experimental design for parameter estimation with 2D partial differential equation models*. PhD thesis.

Beveridge, G. S. G. and Schechter, R. S. (1970). *Optimization: theory and practice*. McGraw-Hill Book Company, New York, 1st edition.

Bier, W., Dariel, M. P., Frage, N., Hartmann, S., and Michailov, O. (2007). Die compaction of copper powder designed for material parameter identification. *International Journal of Mechanical Science*, 49:766–777.

Bier, W. and Hartmann, S. (2006). A finite strain constitutive model for metal powder compaction using a unique and convex single surface yield function. *European Journal of Mechanics, Series A/Solids*, 25:1009–1030.

Björck, A. (1996). *Numerical methods for least squares problems*. SIAM (Society for Industrial and Applied Mathematics), Philadelphia.

Bock, H. G. (1981). Numerical treatment of inverse problems in chemical reaction kinetics. In Ebert, K. H., Deuflhard, P., and Jäger, W., editors, *Modelling of Chemical Reaction Systems*, pages 102–125, Berlin, Heidelberg. Springer Berlin Heidelberg.

Bock, H. G. (1983). Recent advances in parameter identification techniques for ODEs. In Gear, C. W., Vu, T., Deuflhard, P., and Hairer, E., editors, *Numerical Treatment of Inverse Problems in Differential and Integral Equations*, number 2 in Progress in Scientific Computing, pages 95–121, Basel. Birkhäuser.

Bourgoyne, A. (1986). *Applied Drilling Engineering*. SPE textbook series. Society of Petroleum Engineers.

Brenan, K. E., Campbell, S. L., and Petzhold, L. R. (1996). *Numerical Solution of Initial-Value Problems in Differential-Algebraic Equations*. Classics in Applied Mathematics 14. SIAM Society for Industrial and Applied Mathematics, Philadelphia.

Carnavas, P. C. and Page, N. W. (1998). Elastic properties of compacted metal powders. *Journal of Materials Science*, 33:4647–4655.

Chen, Z. and Diebels, S. (2014). Nanoindentation of soft polymers: Modeling, experiments and parameter identification. *Technische Mechanik*, 34:166–189.

Clifton, R. J., Simonson, E. R., Jones, A. H., and Green, S. J. (1976). Determination of the critical-stress-intensity factor kic from internally pressurized thick-walled vessels. *Experimental Mechanics*, 16(6):233–238.

Clough, R. W. (1960). The finite element method in plane stress analysis. In *Proceedings of 2nd ASCE Conference on Electronic Computation, Pittsburgh Pa., Sept. 8 and 9, 1960*.

Consigny, P. M., Tulenko, T. N., and Nicosia, R. F. (1986). Immediate and long-term effects of angioplasty-balloon dilation on normal rabbit iliac artery. *Arteriosclerosis, Thrombosis, and Vascular Biology*, 6(3):265–276.

Cooreman, S., Lecompte, D., Sol, H., Vantomme, J., and Debruyne, D. (2007). Elasto-plastic material parameter identification by inverse methods: Calculation of the sensitivity matrix. *International Journal of Solids and Structures*, 44:4329–4341.

Courant, R. (1943). Variational methods for the solution of problems of equilibrium and vibrations. *Bulletin of the American Mathematical Society*, 49(1):1–24.

Cox, R. H. (1982). Comparison of mechanical and chemical properties of extra- and intralobar canine pulmonary arterie. *American Journal of Physiology - Heart and Circulatory Physiology*, 242:H245–H253.

Cox, R. H. (1983). Comparison of arterial wall mechanics using ring and cylindrical segments. *American Journal of Physiology - Heart and Circulatory Physiology*, 244:H298–H303.

Demkowicz, L., Oden, J. T., Rachowicz, W., and Hardy, O. (1989). Toward a universal hp adaptive finite element strategy, part 1. constrained approximation and data structure. *Computer Methods in Applied Mechanics and Engineering*, 77(1-2):79–112.

Dennis, J. E. and Schnabel, R. B. (1996). *Numerical methods for unconstrained optimization and nonlinear equations*, volume 16 of *Classics in Applied Mathematics*. SIAM Society for Industrial and Applied Mathematics, Philadelphia.

Dhatt, G. and Touzot, G. (1985). *The finite element method displayed*. Wiley and Sons, Chichester.

Diebels, S., Ellsiepen, P., and Ehlers, W. (1999). Error-controlled Runge-Kutta time integration of a viscoplastic hybrid two-phases model. *Technische Mechanik*, 19:19–27.

Draper, N. R. and Smith, H. (1998). *Applied Regression Analysis*. John Wiley & Sons, Inc.

Eckert Jr., J. P. and Mauchly, J. W. (1964). Electronic numerical integrator and computer.

Ehlers, W. and Eipper, G. (1998). The simple tension problem at large volumetric strains computed from finite hyperelastic material laws. *Acta Mechanica*, 130:17–27.

Ellsiepen, P. (1999). *Zeit- und ortsadaptive Verfahren angewandt auf Mehrphasenprobleme poröser Medien*. Doctoral thesis, Institute of Mechanics II, University of Stuttgart. Report No. II-3.

Ellsiepen, P. and Hartmann, S. (2001). Remarks on the interpretation of current non-linear finite element analyses as differential-algebraic equations. *International Journal for Numerical Methods in Engineering*, 51:679–707.

Flory, P. J. (1961). Thermodynamic relations for high elastic materials. *Transaction of the Faraday Society*, 57:829–838.

Fritzen, P. (1997). *Numerische Behandlung nichtlinearer Probleme der Elastizitäts- und Plastizitätstheorie*. Doctoral thesis, Department of Mathematics, University of Darmstadt.

Gasser, T. C., Ogden, R. W., and Holzapfel, G. A. (2006). Hyperelastic modelling of arterial layers with distributed collagen fibre orientations. *Journal of the Royal Society, Interface*, 3(6):15–35.

Gibmeier, J., Hartmann, S., and Scholtes, B. (2005). Effect of applied and residual stresses on the analysis of mechanical properties by means of instrumented indentation techniques. *Materials Science Forum*, 490-491:454–459.

Gilbert, R. R., Grafenhorst, M., Hartmann, S., and Yosibash, Z. (2019). Simulating the temporal change of the active response of arteries by finite elements with high-order time-integrators. *Computational Mechanics*, 64(6):1669–1684.

Gilbert, R. R., Hartmann, S., Kudela, L., Rank, E., Sahar, G., Yosibash, Z., and Yossef, O. (2016). Parameter identification of the passive response in arteries. Technical Report Series Fac3-16-01, Faculty of Mathematics/Computer Science and Mechanical Engineering, Clausthal University of Technology (Germany).

GOM (2009). *ARAMIS User Manual RevA—Software*.

Govindjee, S. and Reese, S. (1997). A presentation and comparison of two large deformation viscoelasticity models. *ASME Journal of Engineering Materials and Technology*, 199:251–255.

Grafenhorst, M. (2018). *Zeitadaptive Finite-Elemente-Berechnungen thermomechanisch gekoppelter Problemstellungen sowie Mortarkontakt*. Phd-thesis, report no. 1/2018, Institute of Applied Mechanics, Clausthal University of Technology, Clausthal-Zellerfeld.

Grédiac, M. and Hild, F., editors (2013). *Full-field measurments and identification in solid mechanics*. John Wiley & Sons., Hoboken, NJ, USA.

Guo, B. and Babuška, I. (1986). The hp version of the finite element method. *Computational Mechanics*, 1(1):21–41.

Hairer, E., Norsett, S. P., and Wanner, G. (1993). *Solving Ordinary Differential Equations I*. Springer, Berlin, 2nd revised edition.

Hairer, E. and Wanner, G. (1996). *Solving Ordinary Differential Equations II*. Springer, Berlin, 2nd revised edition.

Hanabusa, Y., Takizawa, H., and Kuwabara, T. (2013). Numerical verification of a biaxial tensile test method using a cruciform specimen. *Journal of Materials Processing Technology*, 213(6):961 – 970.

Hannon, A. and Tiernan, P. (2008). A review of planar biaxial tensile test systems for sheet metal. *Journal of Materials Processing Technology*, 198(1–3):1 – 13.

Hartmann, S. (1998). Zur Berechnung inelastischer Festkörper mit der Methode der finiten Elemente. In Hartmann, S., Haupt, P., and Ulbricht, V., editors, *Modellierung und Identifikation*, pages 119–130, Kassel. Gesamthochschul-Bibliothek.

Hartmann, S. (2001a). Numerical studies on the identification of the material parameters of Rivlin's hyperelasticity using tension-torsion tests. *Acta Mechanica*, 148:129–155.

Hartmann, S. (2001b). Parameter estimation of hyperelasticity relations of generalized polynomial-type with constraint conditions. *International Journal of Solids and Structures*, 38(44-45):7999–8018.

Hartmann, S. (2002). Computation in finite strain viscoelasticity: finite elements based on the interpretation as differential-algebraic equations. *Computer Methods in Applied Mechanics and Engineering*, 191(13-14):1439–1470.

Hartmann, S. (2003). *Finite-Elemente Berechnung inelastischer Kontinua. Interpretation als Algebro-Differentialgleichungssysteme*. Habilitation, University of Kassel, Institute of Mechanics. Report No. 1/2003.

Hartmann, S. (2005). A remark on the application of the Newton-Raphson method in non-linear finite element analysis. *Computational Mechanics*, 36(2):100–116.

Hartmann, S. (2006). TASA-FEM: Ein Finite-Elemente-Programm für raum- und zeitadaptive gekoppelte Strukturberechnungen. Technical Report 1/2006, Institute of Mechanics, University of Kassel, Kassel, Germany.

Hartmann, S. (2012). *Introduction to Theory of Materials*. Clausthal-Zellerfeld, Germany.

Hartmann, S. (2017). A remark on material parameter identification using finite elements based on constitutive models of evolutionary-type. *Computer Assisted Methods in Engineering and Science*, 24:113 – 126.

Hartmann, S. and Bier, W. (2008). High-order time integration applied to metal powder plasticity. *International Journal of Plasticity*, 24(1):17–54.

Hartmann, S., Gibmeier, J., and Scholtes, B. (2006). Experiments and material parameter identification using finite elements. Uniaxial tests and validation using instrumented indentation tests. *Experimental Mechanics*, 46(1):5–18.

Hartmann, S. and Gilbert, R. R. (2018). Identifiability of material parameters in solid mechanics. *Archive of Applied Mechanics*, 88(1-2):3–26.

Hartmann, S. and Gilbert, R. R. (2021). Material parameter identification using finite elements with time-adaptive higher-order time integration and experimental full-field strain information. *Computational Mechanics*, 68:633–650.

Hartmann, S., Gilbert, R. R., Kheiri Marghzar, A., Leistner, C., and Dileep, P. K. (2021). Material parameter identification of unidirectional fiber-reinforced composites. *Archive of Applied Mechanics*, 91:687–712.

Hartmann, S., Gilbert, R. R., and Sguazzo, C. (2018a). Basic studies in biaxial tensile tests. *GAMM-Mitteilungen*, 41:e201800004.

Hartmann, S. and Hamkar, A.-W. (2010). Rosenbrock-type methods applied to finite element computations within finite strain viscoelasticity. *Computer Methods in Applied Mechanics and Engineering*, 199(23-24):1455–1470.

Hartmann, S., Kheiri Marghzar, A., Gilbert, R. R., Pangboonyanon, W., and Meiners, D. (2020). Experiment, modeling and simulation of bypassing holes in composites. *Composite Structures*, 234:111666.

Hartmann, S., Mohan, J., Müller-Lohse, L., Hagemann, B., and Ganzer, L. (2018b). An analytical solution of multi-layered thick-walled tubes in thermo-elasticity with application to gas-wells. *International Journal of Pressure Vessels and Piping*, 161:10–16.

Hartmann, S. and Neff, P. (2003). Polyconvexity of generalized polynomial-type hyperelastic strain energy functions for near-incompressibility. *International Journal of Solids and Structures*, 40(11):2767–2791.

Hartmann, S., Quint, K. J., and Hamkar, A.-W. (2008). Displacement control in time-adaptive non-linear finite-element analysis. *ZAMM Journal of Applied Mathematics and Mechanics*, 88(5):342–364.

Hartmann, S. and Rodriguez, S. (2018). Verification examples for strain and strain-rate determination of digital image correlation systems. In Altenbach, H., Jablonski, F., Müller, W., Naumenko, K., and Schneider, P., editors, *Advances in Mechanics of Materials and Structural Analysis. Advanced Structured Materials*, number 80 in Advanced Structured Materials, pages 135 – 174. Springer International Publishing, Cham.

Hartmann, S., Tschöpe, T., Schreiber, L., and Haupt, P. (2003). Large deformations of a carbon black-filled rubber. Experiment, optical measurement and parameter identification using finite elements. *European Journal of Mechanics, Series A/Solids*, 22:309–324.

Haupt, P. (2002). *Continuum Mechanics and Theory of Materials*. Springer, Berlin, second edition edition.

Haupt, P. and Lion, A. (1995). Experimental identification and mathematical modelling of viscoplastic material behavior. *Journal of Continuum Mechanics and Thermodynamics*, 7:73–96.

Haupt, P. and Sedlan, K. (2001). Viscoplasticity of elastomeric materials. experimental facts and constitutive modelling. *Archive of Applied Mechanics*, 71:89–109.

Heimes, T. (2005). *Finite Thermoinelastizität*. Number 709 in Fortschrittsberichte, Reihe 5, Grund- und Werkstoffe/Kunststoffe. VDI-Verlag, Düsseldorf.

Holzapfel, G. A. (1996). On large strain viscoelasticity: Continuum formulation and finite element applications to elastomeric structures. *International Journal for Numerical Methods in Engineering*, 39:3903–3926.

Holzapfel, G. A. (2000). *Nonlinear Solid Mechanics*. Wiley & Sons, Chichester.

Holzapfel, G. A. and Simo, J. C. (1996). A new viscoelastic constitutive model for continuous media at finite thermomechanical changes. *International Journal of Solids and Structures*, 33:3019–3034.

Hrennikoff, A. (1941). Solution of Problems of Elasticity by the Framework Method. *Journal of Applied Mechanics*, 8(4):0–0.

Hsu, F. P. K., Schwab, C., Rigamonti, D., and Humphrey, J. D. (1994). Identification of response functions from axisymmetric membrane inflation tests: implications for biomechanics. *International Journal of Solids and Structures*, 31:3375–3386.

Huber, N. and Tsakmakis, C. (1999a). Determination of constitutive properties from sperical indentation data using neural networks, Part II: plasticity with nonlinear and kinematic hardening. *Journal of the Mechanics and Physics of Solids*, 47:1589–1607.

Huber, N. and Tsakmakis, C. (1999b). Determination of constitutive properties from spherical indentation data using neural networks, Part II: the case of pure kinematic hardening in plasticity laws. *Journal of the Mechanics and Physics of Solids*, 47:1569–1588.

Huber, N. and Tsakmakis, C. (2000). Finite deformation viscoelasticity laws. *Mechanics of Materials*, 32:1–18.

Hughes, T. J. R. (1987). *The finite element method*. Prentice-Hall, Engelwood Cliffs, New Jersey, 1st edition.

Kadlowec, J., Wineman, A., and Hulbert, G. (2003). Elastomer bushing response: experiments and finite element modeling. *Acta Mechanica*, 163:25–38.

Kiefer, B., Haldar, K., and Menzel, A. (2015). Modeling, simulation and parameter identification for rate-dependent magnetoactive polymer response. *PAMM*, 15:395–396.

Kleuter, B., Menzel, A., and Steinmann, P. (2007). Generalized parameter identification for finite viscoelasticity. *Computer Methods in Applied Mechanics and Engineering*, 196:3315–3334.

Korelc, J. (1997). Automatic generation of finite-element code by simultaneous optimization of expressions. *Theoretical Computer Science*, 187:231–248.

Korelc, J. (2002). Multi-language and multi-environment generation of nonlinear finite element codes. *Engineering with Computers*, 18:312–327.

Korelc, J. (2009). Automation of primal and sensitivity analysis of transient coupled problems. *Computational Mechanics*, 44(5):631–649.

Krämer, S. (2016). *Einfluss von Unsicherheiten in Materialparametern auf Finite-Elemente Simulationen*. Phd-thesis, report no. 5/2016, Institute of Applied Mechanics, Clausthal University of Technology, Clausthal-Zellerfeld.

Krämer, S., Rothe, S., and Hartmann, S. (2015). Homogeneous stress-strain states computed by 3D-stress algorithms of FE-codes: application to material parameter identification. *Engineering with Computers*, 31:141–159.

Kreißig, R. (1998). Auswertung inhomogener Verschiebungsfelder zur Identifikation der Parameter elastisch-plastischer Deformationsgesetze. *Forschung im Ingenieurwesen*, 64:99–109.

Kreissig, R., Benedix, U., and Goerke, U.-J. (2001). Statistical aspects of the identification of material parameters for elasto-plastic models. *Archive of Applied Mechanics*, 71:123–134.

Lamkanfi, E., Paepegem, W. V., and Degrieck, J. (2015). Shape optimization of a cruciform geometry for biaxial testing of polymers. *Polymer Testing*, 41:7 – 16.

Lawson, C. L. and Hanson, R. J. (1995). *Solving least squares problems*. Siam Society for Industrial and Applied Mathematics, Philadelphia.

Lee, H., Lee, J. H., and Pharr, G. M. (2005). A numerical approach to spherical indentation techniques for material property evaluation. *Journal of the Mechanics and Physics of Solids*, 53:2037–2069.

Lefebvre, D., Chebl, C., Thibodeau, L., and Khazzari, E. (1983). A high-strain biaxial-testing rig for thin-walled tubes under axial load and pressure. *Experimental Mechanics*, 23:384–392.

Lehmann, T. (1984). *Elemente der Mechanik II, Elastostatik*. Vieweg, Braunschweig, 2nd edition.

Lion, A. (1996). A constitutive model for black filled rubber. experimental investigations and mathematical representations. *Journal of Continuum Mechanics and Thermodynamics*, 8:153–169.

Lion, A. (1997). On the large deformation behaviour of reinforced rubber at different temperatures. *Journal of the Mechanics and Physics of Solids*, 45:1805–1834.

Liu, C. H., Hofstetter, G., and Mang, H. A. (1994). 3D finite element analysis of rubber-like materials at finite strains. *Engineering Computations*, 11:111–128.

Lubliner, J. (1985). A model of rubber viscoelasticity. *Mechanics Research Communications*, 12:93–99.

Mahnken, R. (2018). Identification of material parameters for constitutive equations. In Stein, E., De Borst, R., and Hughes, T. J. R., editors, *Encyclopedia of Computational Mechanics*, pages 1165–1185. John Wiley & Sons, 2 edition.

Mahnken, R. and Stein, E. (1996). A unified approach for parameter identification of inelastic material models in the frame of the finite element method. *Computer Methods in Applied Mechanics and Engineering*, 136:225–258.

Mahnken, R. and Stein, E. (1997). Parameter identification for finite deformation elasto-plasticity in principal directions. *Computer Methods in Applied Mechanics and Engineering*, 147:17–39.

Malvern, L. E. (1969). *Introduction to the Mechanics of a Continuous Medium*. Prentice-Hall, New Jersey.

Marsden, J. E. and Hughes, T. J. R. (1994). *Mathematical Foundations of Elasticity*. Dover Publications, New York.

McCormick, N. and Lord, J. (2010). Digital image correlation. *Materials Today*, 13(12):52–54.

Metropolis, N. (1987). The beginning. *Los Alamos Science*, 15:125–130.

Metropolis, N. and Ulam, S. (1949). The monte carlo method. *Journal of the American Statistical Association*, 44(247):335–341.

Miehe, C. and Keck, J. (2000). Superimposed finite elastic-viscoelastic-plastoelastic stress response with damage in filled rubbery polymers. experiments, modelling and algorithmic implementation. *Journal of the Mechanics and Physics of Solids*, 48:323–365.

Mooney, M. (1940). A theory of large elastic deformation. *Journal of Applied Physics*, 11:582–595.

Moré, J. J. and Sorensen, D. C. (1983). Computing a trust region step. *SIAM Journal on Scientific and Statistical Computing*, 4(3):553–572.

Newton, I., Motte, A., and Machin, J. (1729). *The Mathematical Principles of Natural Philosophy*. Number Bd. 1 in The Mathematical Principles of Natural Philosophy. B. Motte.

Nocedal, J. and Wright, S. J. (1999). *Numerical Optimization*. Springer, New York.

Ogden, R. W. (1976). Volume changes associated with the deformation of rubberlike solids. *Journal of the Mechanics and Physics of Solids*, 24:323–338.

Ogden, R. W. (1997). *Non-Linear Elastic Deformations*. Dover Publications, New York.

Ognedal, A. S., Clausen, A. H., Polanco-Loria, M., Benallal, A., Raka, B., and Hopperstad, O. S. (2012). Experimental and numerical study on the behaviour of PVC and HDPE in biaxial tension. *Mechanics of Materials*, 54:18 – 31.

Orteu, J.-J. (2009). 3-D computer vision in experimental mechanics. *Optics and Lasers in Engineering*, 47:282–291.

Peano, A. (1976). Hierarchies of conforming finite elements for plane elasticity and plate bending. *Computers and Mathematics with Applications*, 2:211–224.

Powell, M. (1994). A direct search optimization method that models the objective and constraint functions by linear interpolations. In Gomez, S. and Hennart, J. P., editors, *Advances in Optimization and Numerical Analysis*, pages 51–67, Dordrecht. Kluwer Academic.

Powell, M. J. D. (1998). Direct search algorithms for optimization calculations. *Acta Numerica*, 7:287–336. (see internet address: http://plato.la.asu.edu/topics/problems/nlores.html).

Quint, K. J. (2012). *Thermomechanically coupled processes for functionally graded materials: experiments, modelling, and finite element analysis using high-order DIRK-methods*. Phd-thesis, report no. 2/2012, Institute of Applied Mechanics, Clausthal University of Technology, Clausthal-Zellerfeld.

Rabbat, N. B. G., Sangiovanni-Vincentelli, A. L., and Hsieh, H. Y. (1979). A multilevel Newton algorithm with macromodeling and latency for the analysis of large-scale nonlinear circuits in the time domain. *IEEE Transactions on Circuits and Systems*, 26:733–740.

Rachev, A. and Shazly, T. (2013). A preliminary analysis of the data from an in vitro inflation-extension test can validate the assumption of arterial tissue elasticity. *ASME. Journal of Biomechanical Engineering*, 135(8):084502–084502.

Rauchs, G., Bardon, J., and Georges, D. (2010). Identification of the material parameters of a viscous hyperelastic constitutive law from spherical indentation tests of rubber and validation by tensile tests. *Mechanics of Materials*, 42:961–973.

Reese, S. and Govindjee, S. (1998). A theory of finite viscoelasticity and numerical aspects. *International Journal of Solids and Structures*, 35:3455–3482.

Rentrop, P., Strehmel, K., and Weiner, R. (1995). Ein Überblick über Einschrittverfahren zur numerischen Integration in der technischen Simulation. Reports on Numerical Mathematics 95-12, Department of Mathematics and Computer Science, Institute of Numerical Mathematics, Universität Halle-Wittenberg.

Rivlin, R. S. (1948). Large elastic deformation of isotropic materials. iii. some simple problems in cylindrical polar co-ordinates. *Philosophical Transaction of the Royal Society of London, Series A*, 240:509–525.

Rivlin, R. S. and Saunders, D. W. (1951). Large elastic deformation of isotropic materials. vii. experiments on the deformation of rubber. *Philosophical Transaction of the Royal Society of London, Series A*, 243:251–288.

Rose, L. and Menzel, A. (2019). Influence of thermal boundary conditions on the parameter identification in thermodynamics. *PAMM*, 19:e201900170.

Rose, L. and Menzel, A. (2020). Optimisation based material parameter identification using full field displacement and temperature measurements. *Mechanics of Materials*, 145:103292.

Rothe, S. (2014). *Electro-thermo-mechanical modeling of field assisted sintering technology: experiments, constitutive modeling and finite element analysis*. Phd-thesis, report no. 1/2015, Institute of Applied Mechanics, Clausthal University of Technology, Clausthal-Zellerfeld.

Scheday, G. (2003). *Theorie und Numerik der Parameteridentifikation von Materialmodellen der finiten Elastizität und Inelastizität auf der Grundlage optischer Feldmessmethoden*. Phd-thesis, Report No. I-11 (2003), University of Stuttgart (Germany), Institute of Mechanics.

Schenk, O. and Gärtner, K. (2006). On fast factorization pivoting methods for sparse symmetric indefinite systems. *ETNA. Electronic Transactions on Numerical Analysis [electronic only]*, 23:158–179.

Schiesser, W. (1991). *The Numerical Method of Lines: Integration of Partial Differential Equations*. Academic Press.

Schittkowski, K. (2002). *Numerical data fitting in dynamical systems*. Kluwer Academic Publ., Dordrecht.

Schmaltz, S. and Willner, K. (2013). Material parameter identification utilizing optical full-field strain measurement and digital image correlation. *Journal of the Japanese Society for Experimental Mechanics*, 13:s120–s125.

Schmaltz, S. and Willner, K. (2014). Comparison of different biaxial tests for the identification of sheet steel material parameters. *Strain*, published online.

Schulte, R., Ostwald, R., and Menzel, A. (2020). Gradient-enhanced modelling of damage for rate-dependent material behaviour—a parameter identification framework. *Materials*, 13:3156.

Schwab, C., Schwab, C., and Schwab, C. (1998). *p-and hp-finite element methods: Theory and applications in solid and fluid mechanics*. Oxford University Press.

Schwarz, H. and Köckler, N. (2013). *Numerische Mathematik*. Lehrbuch Mathematik. Vieweg+Teubner Verlag.

Seibert, H., Scheffer, T., and Diebels, S. (2014). Biaxial testing of elastomers - experimental setup, measurement and experimental optimisation of specimen's shape. *Technische Mechanik; 34; 2; 72-89; ISSN 2199-9244*.

Sewerin, F. (2020). On the local identifiability of constituent stress-strain laws for hyperelastic composite materials. *Computational Mechanics*, 65:853–876.

Sguazzo, C. and Hartmann, S. (2018). Tensile and shear experiments using polypropylene/polyethylene foils at different temperatures. *Technische Mechanik. Scientific Journal for Fundamentals and Applications of Engineering Mechanics*, 38(2):166–190.

Shewchuk, J. R. (1996). Triangle: Engineering a 2D Quality Mesh Generator and Delaunay Triangulator. In Lin, M. C. and Manocha, D., editors, *Applied Computational Geometry: Towards Geometric Engineering*, volume 1148 of *Lecture Notes in Computer Science*, pages 203–222. Springer-Verlag. From the First ACM Workshop on Applied Computational Geometry.

Shewchuk, J. R. (2002). Delaunay refinement algorithms for triangular mesh generation. *Computational Geometry: Theory and Applications*, 22(1-3):21–74.

Shildip, D. U., Bhope, D. V., and Khamankar, S. D. (2015). Stress analysis of multilayer pressure vessel. *Journal of Applied Mechanical Engineering*, 4(2):1–6.

Sidoroff, F. (1974). Un modele viscoelastique non lineaire avec configuration intermediaire. *Journal de Mećanique*, 13:679–713.

Simo, J. C. (1985). On the computational significance of the intermediate configuration and hyperelastic stress relations in finite deformation elastoplasticity. *Mechanics of Materials*, 4:439–451.

Simo, J. C. (1987). On a fully three-dimensional finite-strain viscoelastic damage model: Formulation and computational aspects. *Computer Methods in Applied Mechanics and Engineering*, 60:153–173.

Simo, J. C. and Hughes, T. J. R. (1998). *Computational Inelasticity*. Springer, New York, 1st edition.

Simo, J. C. and Taylor, R. L. (1991a). Quasi-incompressible finite elasticity in principal stretches. Continuum basis and numerical algorithms. *Computer Methods in Applied Mechanics and Engineering*, 85:273–310.

Simo, J. C. and Taylor, R. L. (1991b). Quasi-incompressible finite elasticity in principal stretches. continuum basis and numerical algorithms. *Computer Methods in Applied Mechanics and Engineering*, 85:273–310.

Sutton, M., Badel, P., Avril, S., and Lessner, S. (2011). Mechanical identification of hyperelastic anisotropic properties of mouse carotid arteries. In Proulx, T., editor, *Mechanics of Biological Systems and Materials, Proceedings of the 2011 Annual Conference on Experimental and Applied Mechanics*, volume 2, pages 11–17, New York. Springer.

Sutton, M. A., Orteu, J.-J., and Schreier, H.-W. (2009). *Image correlation for shape, motion and deformation measurements*. Springer, New York.

Sutton, M. A., Wolters, W., Peters, W., Ranson, W., and McNeill, S. (1983). Determination of displacements using an improved digital correlation method. *Image and vision computing*, 1(3):133–139.

Szabo, B. and Babuska, I. (1991). *Finite Element Analysis*. Wiley, New York.

Szabo, B. and Mehta, A. (1978). p-convergent finite element approximations in fracture mechanics. *International Journal for Numerical Methods in Engineering*, 12(3):551–560.

Szabó, B. A. (1979). Some recent developments in finite element analysis. *Computers & Mathematics with Applications*, 5(2):99–115.

Tikhonov, A. N., Goncharsky, A. V., Stepanov, V. V., and Yagola, A. G. (1995). *Numerical methods for the solution of ill-posed problems*. Kluwer Academic Publishers, Dordrecht.

Timoschenko, S. P. and Goodier, J. N. (1985). *Theory of Elasticity*. McGraw-Hill Book Company, Singapore, 3rd edition.

Truesdell, C. and Noll, W. (2004). *The Non-Linear Field Theories of Mechanics*. Springer, Berlin, third edition edition.

Ulam, S., Bednarek, A., and Ulam, F. (1990). *Analogies Between Analogies: The Mathematical Reports of S.M. Ulam and His Los Alamos Collaborators*. Los Alamos series in basic and applied sciences. University of California Press.

Šimůnek, J. and Hopmans, J. W. (2002). 1.7 parameter optimization and nonlinear fitting. *Methods of Soil Analysis: Part 4 Physical Methods*, 5:139–157.

Wittekindt, J. (1991). *Die numerische Lösung von Anfangs-Randwertproblemen zur Beschreibung inelastischen Werkstoffverhaltens*. Doctoral thesis, Department of Mathematics, University of Darmstadt.

Wriggers, P. (2008). *Nonlinear Finite Element Methods*. Springer Berlin Heidelberg.

Yeh, M. and Kyriakides, S. (1986). On the collapse of inelastic thick-walled tubes under external pressure. *ASME. Journal of Energy Resources and Technology*, 108(1):35–47.

Zienkiewicz, O. C. (1984). *Methode der finiten Elemente*. Carl Hanser, München, 2nd edition.

Zienkiewicz, O. C. and Taylor, R. L. (2000a). *The Finite Element Method*, volume 2. Butterworth & Heinemann, Oxford, 5th edition.

Zienkiewicz, O. C. and Taylor, R. L. (2000b). *The Finite Element Method*, volume 1. Butterworth & Heinemann, Oxford, 5th edition.

# List of Publications

S. Hartmann, R. R. Gilbert: *Material parameter identification using finite elements with time-adaptive higher-order time integration and experimental full-field strain information*, Computational Mechanics 68:633-650, 2021

S. Hartmann, R. R. Gilbert, A.K. Marghzar, C. Leistner, and P. K. Dileep: *Material parameter identification of unidirectional fiber-reinforced composites*, Archive of Applied Mechanics 91, 687–712, 2021

S. Hartmann, A.K. Marghzar, R. R. Gilbert, W. Pangboonyanon, D. Meiners: *Experiment, modeling and simulation of bypassing holes in composites*, Composite Structures 234:111666, 2020, 1-16

M. Harhash, R. R. Gilbert, S. Hartmann, H. Palkowski: *Experimental characterization, analytical and numerical investigations of metal/polymer/metal sandwich composites – Part 2: free bending*, Composite Structures 232:111421, 2020, 1-15

Gilbert, R.R., Grafenhorst, M., Hartmann, S., Yosibash, Z.: *Simulating the temporal change of the active response of arteries by finite elements with high-order time-integrators*, Computational Mechanics 64(6), 1669-1684, 2019

M. Harhash, R. R. Gilbert, S. Hartmann, H. Palkowski: *Experimental characterization, analytical and numerical investigations of metal/polymer/metal sandwich composites – Part 1: Deep drawing*, Composite Structures 202, 1308 - 1321, 2018

Hartmann, S., Gilbert, R. R., Sguazzo, C.: *Basic studies in biaxial tensile tests*, GAMM-Mitteilungen 41(1): e201800004, 2018

Hartmann, S., Gilbert, R. R.: *Identifiability of material parameters in solid mechanics*, Archive of Applied Mechanics 88 (1), 3 - 26, 2018

Hartmann, S., Gilbert, R. R.: *From Experiment to Material Parameter Identification*, PAMM Proceedings in Applied Mathematics and Mechanics 18, 2018, e201800440, pp. 1-4

Gilbert, R. R., Hartmann, S., Kudela, L., Rank, E., Yossef, O., Yosibash, Z.: *Numerical modeling of active response of arteries*, PAMM Proceedings in Applied Mathematics and Mechanics 17, 189 – 190, 2017

Gilbert, R. R., Hartmann, S., Kudela, L., Rank, E., Yosibash, Z., Yossef, O.: *Problems in parameter identification of the passive response in human arteries*, PAMM Proceedings in Applied Mathematics and Mechanics 16, 83-84, 2016

Gilbert, R. R., Hartmann, S., Kudela, L., Rank, E., Sahar, G., Yosibash, Z., Yossef, O.: *Parameter identification of the passive response in arteries*, Technical Report Series Fac3-16-01, Faculty of Mathematics/Computer Science and Mechanical Engineering, Clausthal University of Technology, 2016